



January 2013

Theoretical Studies Of Oxides Relevant To The Combustion Of Fossil Fuels

Jason Hicks

Follow this and additional works at: <https://commons.und.edu/theses>

Recommended Citation

Hicks, Jason, "Theoretical Studies Of Oxides Relevant To The Combustion Of Fossil Fuels" (2013). *Theses and Dissertations*. 1544.
<https://commons.und.edu/theses/1544>

This Thesis is brought to you for free and open access by the Theses, Dissertations, and Senior Projects at UND Scholarly Commons. It has been accepted for inclusion in Theses and Dissertations by an authorized administrator of UND Scholarly Commons. For more information, please contact zeinebyousif@library.und.edu.

THEORETICAL STUDIES OF OXIDES RELEVANT TO THE COMBUSTION OF
FOSSIL FUELS

by

Jason Michael Hicks

Bachelor of Science, Chemistry, University of North Dakota, 2010
Associate of Arts, Northland Community and Technical College, 2008

A Thesis

Submitted to the Graduate Faculty

of the

University of North Dakota

in partial fulfillment of the requirements

for the degree of

Master of Science

Grand Forks, North Dakota

December

2013

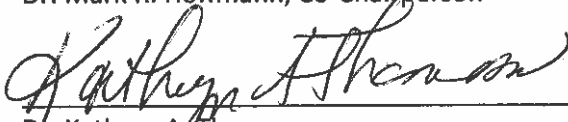
This thesis, submitted by Jason Hicks in partial fulfillment of the requirements for the Degree of Master of Science from the University of North Dakota, has been read by the Faculty Advisory Committee under whom the work has been done and is hereby approved.



Dr. Jerome Delhommelle, Co-Chairperson

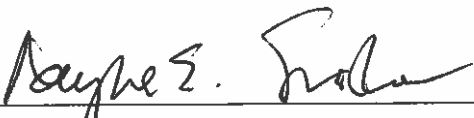


Dr. Mark R. Hoffmann, Co-Chairperson



Dr. Kathryn A. Thomasson

This thesis is being submitted by the appointed advisory committee as having met all of the requirements of the School of Graduate Studies at the University of North Dakota and is hereby approved.



Dr. Wayne Swisher
Dean, School of Graduate Studies



Date

PERMISSION

Title Theoretical Studies of Oxides Relevant to the Combustion of Fossil Fuels

Department Chemistry

Degree Master of Science

In presenting this thesis in partial fulfillment of the requirements for a graduate degree from the University of North Dakota, I agree that the library of this University shall make it freely available for inspection. I further agree that permission for extensive copying for scholarly purposes may be granted by the professor who supervised my thesis work or, in their absence, by the chairperson of the department or the dean of the School of Graduate Studies. It is understood that any copying or publication or other use of this dissertation or part thereof for financial gain shall not be allowed without my written permission. It is also understood that due recognition shall be given to me and to the University of North Dakota in any scholarly use which may be made of any material in my thesis.

Name: Jason Hicks

Date: 11/26/2013

TABLE OF CONTENTS

LIST OF FIGURES	vii
LIST OF TABLES	xiv
ACKNOWLEDGMENTS	xvi
ABSTRACT	xviii
1 GENERAL INTRODUCTION AND STRUCTURE OF THE THESIS	1
2 MODELING THE ENCAPSULATION OF CO₂ INTO IRMOFS USING EX- PANDED WANG-LANDAU SIMULATIONS	4
2.1 BACKGROUND	5
2.1.1 Motivations	5
2.1.2 Porous Materials	10
2.1.3 State of the Art in Molecular Simulation	17
2.2 WANG-LANDAU SAMPLING	22
2.2.1 Quantum Origins	25
2.2.2 Formalism for Classical Systems	34

2.3	EXPANDED WANG-LANDAU SAMPLING	44
2.3.1	Formalism	44
2.3.2	Determination of Thermodynamic Properties	49
2.3.3	Applied to Vapor-Liquid Equilibrium	55
2.4	APPLICATIONS TO CO ₂ ADSORPTION INTO IRMOFS	61
2.4.1	Simulation Details and Models used for CO ₂ and the IRMOFs	62
2.4.2	Solution Thermodynamics Approach	65
2.4.3	Performance of IRMOF-1, 8 and 10 in Supercritical and Subcritical Regimes	71
2.5	CHAPTER CONCLUSION	85
3	THEORETICAL STUDIES OF THE RELATIVE ENERGIES OF DIMERIC ARSENIC AND SELENIUM OXIDES	87
3.1	BACKGROUND	88
3.1.1	Motivations	88
3.1.2	Computational Chemistry	92
3.2	METHODS	94
3.2.1	Hartree-Fock Approximation	95
3.2.2	Second Order Møller-Plesset Perturbation Theory	102
3.2.3	Multi-Configurational Self-Consistent Field Theory	106
3.2.4	Second-Order Generalized Van Vleck Perturbation Theory	109
3.3	RESULTS	116
3.3.1	Computational Details	116

3.3.2	Validation of the Computational Protocol	119
3.3.3	Se ₂ O ₃	121
3.3.4	Se ₂ O ₅	126
3.3.5	As ₂ O ₃	133
3.3.6	As ₂ O ₅	137
3.4	CHAPTER CONCLUSIONS AND FUTURE PROSPECTS	142

REFERENCES **146**

LIST OF FIGURES

2.1	Mean atmospheric CO ₂ concentration in parts per million at Mauna Loa Observatory from 1958-present. It shows the continual and accelerating increase of CO ₂ concentration in atmosphere. Figure taken from reference 1.	5
2.2	Anthropogenic CO ₂ emission in China from 1980-2011. Figure taken from reference 2.	6
2.3	CO ₂ emissions in thousands of metric tons per year by country in 2006. ^{7,8}	8
2.4	Flow chart showing the various methods available for CO ₂ capture by absorption and adsorption. Figure taken from reference 9.	10
2.5	Various types of carbonaceous adsorbents. From top to bottom: single-walled CNT, multi-walled CNT, ordered meso-porous carbon, carbon nanofiber, fly ash, almond shell and anthracite. This figure, which compiles figures taken from references 17–21, is a slightly modified version of figure 1 from reference 22.	11
2.6	The microporous repeating molecular structure of ZSM-5, which is an aluminosilicate zeolite with a chemical formula is Na _n Al _n Si _{96n} O ₁₉₂ · 16H ₂ O (where 0 < n < 27). Figure taken from reference 23.	13

2.7	Construction of a MOF, from the organic and inorganic subunits to the main building unit and then to three-dimensional framework where the spheres represent the pores (i.e., the empty space available). The last image highlights the geometrical symmetry. This figure, which compiles figures taken from references 30 and 31, is taken from reference 29.	14
2.8	Synthesis of IRMOF-1. The yellow sphere represents the pore size. Reproduced from reference 14.	15
2.9	First 16 IRMOFs. The yellow spheres inside the IRMOFs represent the free volume. Figure taken from reference 33.	16
2.10	The percent free volumes in the first 16 IRMOFs. Figure taken from reference 33.	16
2.11	A pictorial representation of a GCMC simulation box. Both the number of particles and the energy are allowed to fluctuate, while the chemical potential, temperature and volume are kept constant. Figure taken from reference 61.	19
2.12	Five isotherms computed by CGMC and compared to experimental results. Figure taken from reference 50.	20
2.13	When regular Boltzmann sampling is used, the sampling gets trapped in either the vapor or liquid phases (ρ_v and ρ_l respectively) since the probability of the system being in between the two states is near zero.	23

2.14	When WL sampling is used, all states of the system can be equally sampled. There is no longer any issue traversing from one phase to another since the probability is the same for all values of the order parameter ρ for the entire range the user specifies.	24
2.15	Schematic of a 5×5 Ising or 2D Potts model. Figure taken from reference 61	26
2.16	The canonical distribution at the transition temperature for various L sizes of the 2D ten Potts model. The histogram of visited states for $L = 100$ is shown in the inset. Figure taken from reference 75	32
2.17	The density of states obtained via WL sampling along with exact results obtained by Beale's method. ¹⁰³ The inset shows the relative error ($\epsilon(\log[\Omega(E)])$). Figure taken from reference 75	33
2.18	Converging estimates of $\ln(Q(N, V, T))$ which draw closer to the true value up to a multiplicative constant as f draws closer to unity. ⁸⁵	38
2.19	Vapor-liquid equilibria for naphthalene (\square), anthracene (\circ) and phenanthrene (\triangle). Estimates for the critical point are plotted in bold. ⁸⁵	39
2.20	Two molecules of CO_2 , the one on the left is a full particle, while the one on the right is a particle of fraction close to $l=50$	45
2.21	The number distribution $p(N)$ of argon at $T = 140.46\text{K}$ for different values of μ : (a) $\mu = -316.62 \text{ kJ/kg}$ (bulk liquid), (b) $\mu = -361.68 \text{ kJ/kg}$ (bulk vapor), and (c) $\mu = -323.27 \text{ kJ/kg}$ (liquid-vapor coexistence). Figures taken from reference 92	50

2.22	The logarithm of the reduced canonical partition function for carbon dioxide plotted against the number of CO ₂ molecules, where $Q^*(N, V, T) = \frac{\Lambda^{3N} Q(N, V, T)}{\left(\frac{8\pi^2 1k_B T}{2h^2}\right)^N}$. Figure taken from reference 92	57
2.23	Vapor-liquid phase diagrams for CO ₂ in the (a) pressure-temperature plane and in the (b) volume-pressure plane. Results from expanded WL are connected by a solid line, where the experimental data are shown with empty squares. ⁹¹ The estimated critical point is given as a filled circle. Figures taken from reference 92	58
2.24	Single-phase bulk properties for carbon dioxide: Variations of (a) density and (b) entropy as a function of pressure for the gas phase. The simulations results obtained are shown with lines, while the experimental data are shown as empty squares. ⁹¹ Figure taken from reference 92.	60
2.25	Ball-stick and space-fill models of IRMOF-1, showing the inorganic and organic subunits.	65
2.26	Six snapshots of CO ₂ adsorption into a single cell of IRMOF-1, for which all the volumes and temperatures are the same.	66
2.27	The natural logarithm of the reduced canonical partition function $Q^*(N, V, T)$ plotted against the number of atoms adsorbed per unit cell at eight different temperatures for: (a) IRMOF-1, (b) IRMOF-8, and (c) IRMOF-10. The reduced canonical partition function is reduced with respect to the partition function of an ideal gas which is composed of rigid, linear molecules. ⁹⁴ . . .	72

2.28	Adsorption isotherms of eight temperatures for: (a) IRMOF-1, (b) IRMOF-8, and (c) IRMOF-10. ⁹⁴ The results from a set of GCMC simulations ⁵⁹ at 225 K for IRMOF-1 is included for comparison (black circles).	74
2.29	Absolute amount (solid line) and excess amount (dashed line) adsorbed per unit cell of IRMOF-8 (in mol/kg) against pressure at: (a) 220 K (subcritical temperature) and (b) 360 K (supercritical temperature). ⁹⁴	76
2.30	ΔG^e (solid line), ΔG^{comp} (dotted line), and ΔG^{imm} (dashed line) against pressure at 220 K (left panel) and at 360 K (right panel). On both panels, results are shown for IRMOF-1 (top), IRMOF-8 (middle), and IRMOF-10 (bottom). ⁹⁴	77
2.31	ΔH^e (solid line), ΔH^{comp} (circles), and ΔH^{imm} (triangles) against pressure at 220 K (left panel) and at 360 K (right panel). On both panels, results are shown for IRMOF-1 (top), IRMOF-8 (middle), and IRMOF-10 (bottom). ⁹⁴	79
2.32	ΔS^e (solid line), ΔS^{comp} (circles), and ΔS^{imm} (triangles) against pressure at 220 K (left panel) and at 360 K (right panel). On both panels, results are shown for IRMOF-1 (top), IRMOF-8 (middle), and IRMOF-10 (bottom). ⁹⁴	80
2.33	Desorption functions as a function of pressure at 220 K (left panel) and at 360 K (right panel). On both panels, results are shown for IRMOF-1 (top), IRMOF-8 (middle), and IRMOF-10 (bottom). G is shown with a solid line, H with a dotted line, and TS with a dashed line. ⁹⁴	82
2.34	The desorption free energy, $ \Omega^e $, plotted against pressure for: (a) IRMOF-1, (b) IRMOF-8, and (c) IRMOF-10. ⁹⁴	84

3.1	The 2009 total world electricity generation by fuel. Within the “Other Renewables” category are solar, wind, combustible renewables, geothermal and waste. Figure taken from reference 139.	89
3.2	Examples of the isomers of As_2O_3 (a), As_2O_5 (b), Se_2O_3 (c) and Se_2O_5 respectively. Oxygen is red, arsenic is purple and selenium is yellow.	94
3.3	The Hamiltonian matrix represented as a box. (a) The \mathbf{H}_{MM} matrix has a small number of electron configurations and neglects dynamic correlation while the full H matrix has a large number of configurations and includes dynamic correlation. (b) By a final diagonalization, dynamic electron correlation is included into \mathbf{H}_{MM}^{eff} by the contributions from \mathbf{H}_{QM} and \mathbf{H}_{MQ} while only the diagonal elements of \mathbf{H}_{QQ} are kept.	112
3.4	Structure of isomer 1 of diselenium trioxide (Se_2O_3). ²¹⁸	121
3.5	Relative GVVPT2/cc-pVTZ energies of diselenium trioxide (Se_2O_3) isomers and transition states (in kcal/mol). ²¹⁸	124
3.6	Relative GVVPT2/cc-pVDZ energies of diselenium trioxide (Se_2O_3) isomers and transition states (in kcal/mol). ²¹⁸	125
3.7	Structure of TS12 of diselenium pentoxide (Se_2O_5). ²¹⁸	127
3.8	Relative GVVPT2/cc-pVDZ energies of diselenium pentoxide (Se_2O_5) isomers and transition states (in kcal/mol). ²¹⁸	131
3.9	Relative GVVPT2/cc-pVTZ energies of diselenium pentoxide (Se_2O_5) isomers and transition states (in kcal/mol). ²¹⁸	132
3.10	Structure of isomer 4 of diarsenic trioxide (As_2O_3). ²¹⁸	134

3.11	Relative GVVPT2/cc-pVTZ energies of diarsenic trioxide (As_2O_3) isomers and transition states (in kcal/mol).(Hicks and co-workers. Not yet submitted for publication)	136
3.12	Structure of isomer 5 of diarsenic pentoxide (As_2O_5). ²²⁰	138
3.13	Relative GVVPT2/cc-pVTZ energies of diarsenic pentoxide (As_2O_5) isomers and transition states (in kcal/mol).(Hicks and co-workers. Not yet submitted for publication)	141

LIST OF TABLES

2.1	Densities of the liquid and vapor phases of naphthalene at coexistence as well as the vapor pressure from HMC WL ⁸⁵ and experimental data. ⁹¹ . . .	40
2.2	Entropies at coexistence for CO ₂ from expanded WL simulations (S_{sim}) compared to experimental data (S_{exp}). ⁹¹	59
3.1	Optimized B3LYP/6-311G* geometrical parameters (Å and degrees) of the diselenium trioxide (Se ₂ O ₃) isomers and transition states. ²¹⁸	122
3.2	Relative energies (kcal/mol) of the diselenium trioxide (Se ₂ O ₃) isomers and transition states. ²¹⁸	123
3.3	Total energies (a.u.) of SeO, SeO ₂ and Se ₂ O ₃ (isomer 1), and predicted reaction energy (kcal/mol) where both GVVPT2 and CR-CC(2,3) used the optimized B3LYP/6-311G* geometries. ²¹⁸	126
3.4	Optimized B3LYP/6-311G* geometrical parameters (Å and degrees) of the diselenium pentoxide (Se ₂ O ₅) isomers. ²¹⁸	127
3.5	Optimized B3LYP/6-311G* geometrical parameters (Å and degrees) of the diselenium pentoxide (Se ₂ O ₅) transition states. ²¹⁸	128

3.6	Relative energies (kcal/mol) of the diselenium pentoxide (Se_2O_5) isomers and transition states. ²¹⁸	130
3.7	Total energies (a.u.) of O_2 , SeO_3 and Se_2O_5 (isomer 4), and predicted reaction energy (kcal/mol) where ΔE_{rxn1} refers to ($\text{SeO}_2 + \text{SeO}_3 \rightarrow \text{Se}_2\text{O}_5$ (4)) and ΔE_{rxn2} refers to (Se_2O_3 (1) + $\text{O}_2 \rightarrow \text{Se}_2\text{O}_5$ (4)). Both GVVPT2 and CR-CC(2,3) used the optimized B3LYP/6-311G* geometries. ²¹⁸	133
3.8	Optimized B3LYP/6-311G* geometrical parameters (\AA and degrees) of the diarsenic trioxide (As_2O_3) isomers and transition states. ²²⁰	134
3.9	Relative energies (kcal/mol) at the B3LYP, CR-CC(2,3) and GVVPT2 levels of theory of the diarsenic trioxide (As_2O_3) isomers and transition states.(Hicks and co-workers. Not yet submitted for publication).	135
3.10	Optimized B3LYP/6-311G* geometrical parameters (\AA and degrees) of the diarsenic pentoxide (As_2O_5) isomers. ²²⁰	138
3.11	Optimized B3LYP/6-311G* geometrical parameters (\AA and degrees) of the diarsenic pentoxide (As_2O_5) transition states. ²²⁰	139
3.12	Relative energies (kcal/mol) at the B3LYP, CR-CC(2,3) and GVVPT2 levels of theory of the diarsenic pentoxide (As_2O_5) isomers and transition states.(Hicks and co-workers. Not yet submitted for publication)	140

ACKNOWLEDGMENTS

Firstly, I would like to thank my co-advisors, Prof. Mark Hoffmann and Prof. Jerome Delhommelle for their continual guidance in my education and research; I would not be where I am now if not for them. Their deep understanding of science and their willingness to help enabled me to gain a much better grasp of our research.

I would like to thank Prof. Hoffmann, in particular, for his countless hours helping me with correcting and polishing up the various drafts of my thesis. I feel that I have really grown as a writer due to his valuable mentorship in this regard. He has also always been so willing to meet with me and answer my barrage of questions, many times even without an appointment.

I would like to thank Prof. Delhommelle, in particular, for always encouraging and guiding me in getting a deeper and broader understanding of the literature background behind my research. He has always encouraged me to attend and present at local and national conferences, which I am greatly thankful for. Through those experiences he has helped me gain valuable power point and poster presentation skills while provided me with valuable networking opportunities.

I would also like to thank Prof. Kathryn Thomasson for her help answering all my questions and agreeing to serve on my Master's committee.

I would like to thank Dr. Desgranges for all of the helpful discussions and educational experiences she has given me as well as her guidance in the various sections of the first part of my thesis. Her excitement for our research would give me motivation that I would not have had otherwise. I would also like to thank all my fellow group members in each

research group for all of their help and support during my masters work, you have all proven to valuable colleagues as well as great friends.

I would like to thank all of my other friends and family who have so instrumental to my life. My mom and dad deserve an indescribable amount of thanks for all of their continual support and prayers.

I would especially like to thank my wonderful wife Erica Hicks for all of her love and encouragement throughout my stay here. She has so lovingly put up with all the late nights I have put in finishing this thesis.

Last, but certainly not least, I would like to thank God for all of his guidance, love, presence and wisdom. He has been there from the beginning pushing me to step outside my comfort zone and giving me the wisdom, strength and motivation I need to make it through. I am deeply grateful for all of He has done and is still doing for me. There were so many times throughout my graduate work, when things were not going well, that He filled me with and indescribable peace through His Holy Spirit or miraculously came through and helped me in ways I did not even think possible. I am so incredibly grateful for this.

ABSTRACT

Anthropogenic pollution has greatly increased since the industrial revolution and continues to increase as more of the world becomes dependent upon fossil fuels for important applications like transportation and power production. In a general case, whenever a fossil fuel is consumed, a primary product of a complete combustion reaction is carbon dioxide. In a more specific case, the collection, processing and combustion of coal for power production are one of the primary ways by which trace elements, such as arsenic and selenium, are released into the environment. All of these pollutants are known to have harmful effects, whether on the environment, human health or power production itself. Because of this there has been an increasing interest in studies related to combating these pollutants.

Concerning CO₂ emissions, recently there has been a significant amount of work related to CO₂ capture. A promising method involves the encapsulation of CO₂ into isorecticular metal-organic frameworks (IRMOFs). The effectiveness of IMROFs greatly depends on the choice of both metal and organic parts. Molecular simulations have been used in the past to aid in the design and characterization of new MOFs, in particular by generating an adsorption isotherm. However, these traditional simulation methods have several drawbacks. The method used in this thesis, namely expanded Wang-Landau, not only overcomes these drawbacks but provides access to all the thermodynamic properties relevant to the adsorption process through a solution thermodynamics approach. This is greatly beneficial, since an excellent way to characterize the performance of various MOFs is by comparing their desorption free energy, i.e., the energy it takes to regenerate a saturated MOF to prepare it for the next adsorption cycle. Expanded WL was used in the study of CO₂ adsorption into

IRMOF-1, 8 and 10 at eight temperatures, spanning both the subcritical and supercritical regimes and the following were obtained: adsorption isotherms, Gibbs free energy, enthalpy, entropy and desorption free energy. It was found that, when the maximum loading was compared to the regeneration costs, IRMOF-10 had the best performance, followed by IRMOF-8 then IRMOF-1.

During the combustion of coal, not only is CO_2 produced, but also the trace elements of arsenic and selenium escape into the environment through this process. Both arsenic and selenium are known to have harmful effects on the environment and human health. Arsenic is also known to poison the catalytic converter used in selective catalytic reduction of NO_x . These trace elements have been found on fly ash or in the hot flue gases released into the atmosphere. In flue gases they most often exist as oxides. There have been many experimental and a few theoretical studies on the monomeric oxides, AsO_x and SeO_x , where $x = 1, 2, \text{ or } 3$. However, little is known concerning the corresponding dimeric oxides, As_2O_x and Se_2O_x , where $x = 3 \text{ or } 5$, though these compounds are expected from their similarities to nitrogen and sulfur chemistry, respectively. From an experimental perspective, they are very challenging to study due to the high temperatures, complex environments and low concentrations needed for a direct study of the form and structures of the dimeric oxides. From a theoretical perspective, they can be challenging to study due to their multireference character and the need for both dynamic and non-dynamic electron correlation due to bonds forming and breaking during isomerization. However, high level multireference *ab initio* methods which account for both dynamic and non-dynamic electron correlation can be used. In the work contained in this thesis, GVVPT2 and CR-CC(2,3) were used to study the relative stabilities of all relevant isomers and transition states of As_2O_x and

Se₂O_x. The structures used were generated through DFT using the B3LYP functional. Not only were plausible stationary points located for all species, it was further confirmed that GVVPT2, though with lower computational cost than CR-CC(2,3), can accurately predict such complex surfaces.

Chapter 1

GENERAL INTRODUCTION AND STRUCTURE OF THE THESIS

The combustion of fossil fuels play an undeniably crucial role in modern day society. Due to the high energy density of these fuels and their current relatively high abundance, they see extensive use in transportation and power production. The use of these fuels, however, can have harmful side effects on the environment (e.g., climate and human health). In effort to mitigate these harmful effects, computational chemistry with its wide variety of methods and applications can be of use. When modeling in the nanoscale, computational statistical thermodynamics, e.g., can be used to screen through and compare various materials for removing pollutants from the fossil fuel combustion exhaust. When working with relatively small molecules, computational quantum chemistry, e.g., can use electronic structure calculations to determine the structures and relative energies of various pollutants which can aid in the design of technologies to break down or remove these pollutants. In this thesis, two projects with two different advisors using two very different methods, but with connection in the application, will be presented. Therefore, this thesis is broken up into two parts and the structure is as follows.

In Chapter 2, the work conducted with Dr. Delhommelle will be presented, in which the encapsulation of CO_2 into IRMOFs was modeled using expanded Wang-Landau (WL) simulations. More specifically, in Section 2.1 the background behind the research will be given, focusing on both the practical applications and the motivation for the use of the expanded WL method. In Section 2.2 a brief introduction on how the WL sampling method originated is given followed by a detailed description of the WL algorithm when applied to the isothermal-isobaric and grand canonical ensemble. In Section 2.3 the formalism for expanded WL is given followed by how the grand canonical partition function can be generated, how the thermodynamic properties are determined and how it was applied

to vapor-liquid equilibrium. In Section 2.4 my work in which expanded WL simulations were used to model CO₂ adsorption into IRMOF-1, 8 and 10 is presented. Specifically, the simulation details are given, the solution thermodynamic approach is explained and the results are presented and discussed. Finally, the conclusions of the work conducted with Dr. Delhomelle are given in Section 2.5.

In Chapter 3, the work conducted with Dr. Hoffmann will be presented, in which the relative energies of dimeric arsenic and selenium oxides were calculated. More specifically, in Section 3.1 the background will be given, focusing on both the motivation behind this research and how computational chemistry can be a powerful tool to solve this type of problem. In Section 3.2, the general computational procedure used to obtain the results presented in this part of this thesis and a brief introduction to the notation as well as the various *ab initio* methods used will be given. In Section 3.3 several relevant details of the calculations, an explanation of the validity of the computational protocol and the results for single point energy calculations of the dimeric selenium and arsenic oxides will be given. Finally, the conclusions of the work conducted with Dr. Hoffmann given in Section 3.4.

Chapter 2

MODELING THE ENCAPSULATION OF CO₂ INTO IRMOFS USING EXPANDED WANG-LANDAU SIMULATIONS

2.1 BACKGROUND

2.1.1 Motivations

Since the beginning of the industrial revolution in ca. 1760, anthropogenic CO₂ emissions, due to the combustion of fossil fuels, have continued to climb at an alarming rate. Over the years since then, the concentrations of CO₂ in the atmosphere has risen from 280 ppm to 390 ppm in 2010.¹ A snapshot of this rise over the last half century is shown in Figure 2.1.

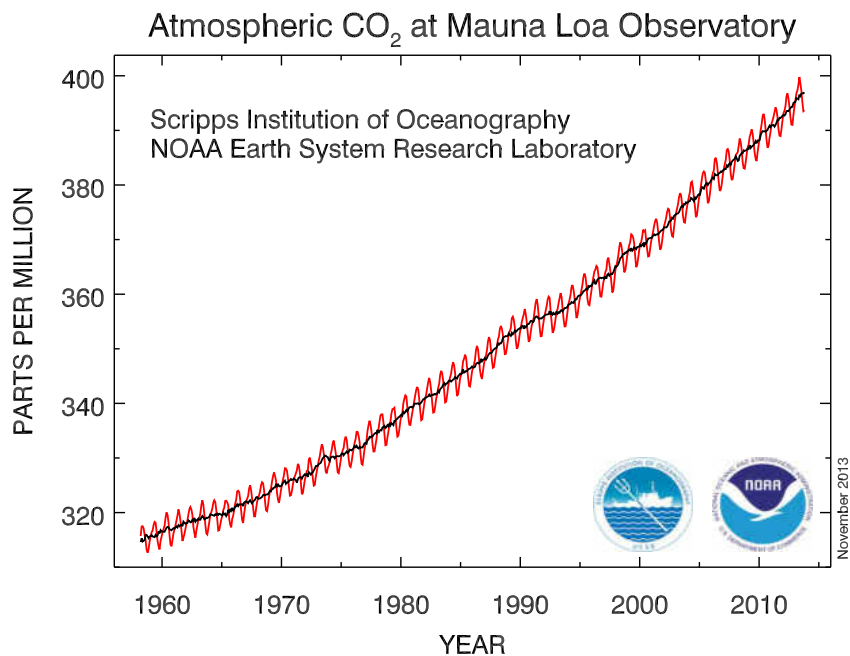


Figure 2.1. Mean atmospheric CO₂ concentration in parts per million at Mauna Loa Observatory from 1958-present. It shows the continual and accelerating increase of CO₂ concentration in atmosphere. Figure taken from reference 1.

Currently over 85% of the world's energy is supplied through the combustion of fossil fuels.¹ As the world's population rapidly increases and as the economies of developing

countries grow, the consumption of such fuels have been and are still vastly increasing anthropogenic CO₂ emission. For example, China's booming economy has increased their CO₂ emission nearly an order of magnitude over the last few decades as shown in Figure 2.2. This alarming trend will only continue around the world unless progressive steps are taken toward reducing the amount of CO₂ that is released into the atmosphere.

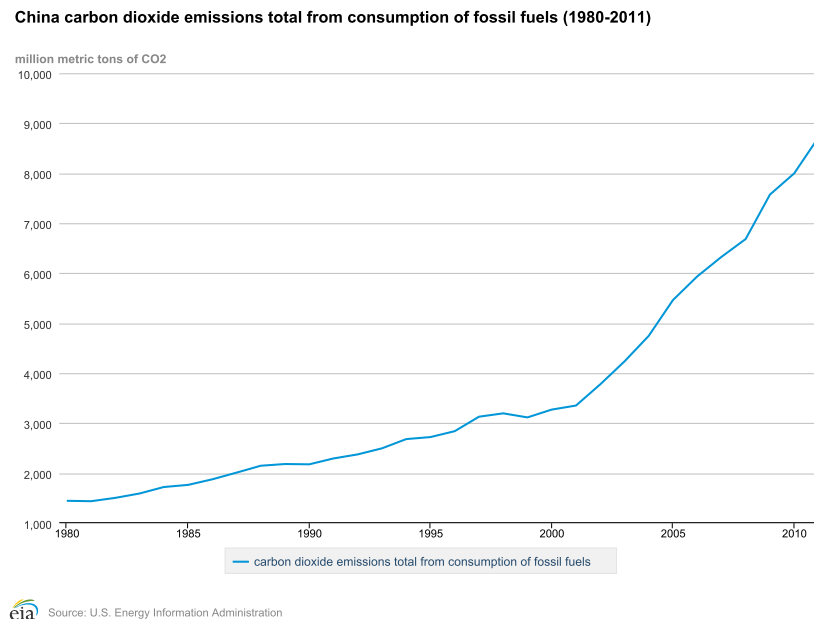


Figure 2.2. Anthropogenic CO₂ emission in China from 1980-2011. Figure taken from reference 2.

A graphical representation of the world's CO₂ emission due to human consumption in 2006 is given in Figure 2.3. As developing countries continue to grow, the many countries which currently have relatively low emissions may greatly increase their output, resulting in a considerably more serious problem. Though anthropogenic CO₂ emissions account for a relatively small amount when compared to many natural carbon fluxes, this increasing rate of CO₂ emission has upset the natural carbon balance of our planet and has had clear influences on the climate in a short amount of time.^{3,4}

Carbon dioxide, along with other greenhouse gases (GHGs), has been shown to trap heat from the sun due to its activity in the infrared region of the electromagnetic spectrum. Thus, the increased level of CO₂ concentration in the atmosphere upsets the balance of ingoing and outgoing energy, resulting in an increase in the average surface temperature of earth. This unnatural climate change produces many other negative consequences on the health of our planet, e.g., rising sea levels, directly affecting human life. There are many highly populated areas that are very close to sea level which are at high risk of flooding with the rising sea levels. The country of Maldives is an island nation southwest of India with the lowest natural highest point in the world, at only 2.4 metres (i.e., 7 ft 10 in).⁵ That country is in real danger of being wiped from existence by these rising sea levels caused by this increase in earths average surface temperature.

Presently, CO₂ contributes to more then 60% of global warming, due to the huge volumes being released into the atmosphere.⁶ Although many details are uncertain on the precise mechanism behind climate change, it is certain that technologies and methods to reduce the CO₂ emissions are desperately needed to preserve the planet's ecosystem while minimizing the present climate change.

As harmful byproducts of this problem have become more apparent, society's awareness of the harmful consequences of GHGs has vastly improved, which, in turn, has increased the effort to control the output of CO₂ emissions. However, it is a difficult task to reduce CO₂ emissions, whether in industry or in transportation. An immediate halt to the use of fossil fuels is currently not possible since much of modern society is highly dependent upon these fuels. In the United States, over 82.3% of the anthropogenic CO₂ emissions were due to the combustion of carbon-based fossil fuels in 2004.^{10,11}

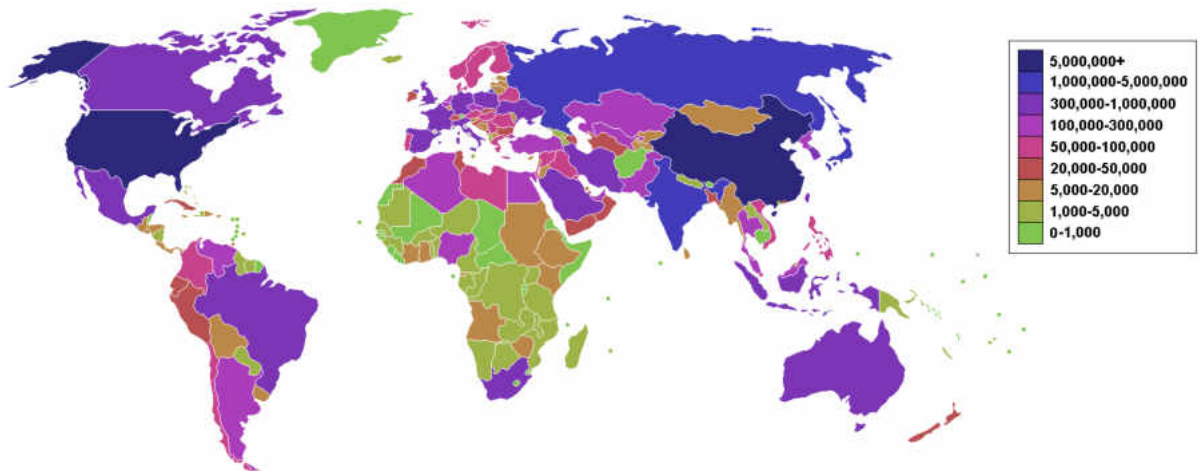


Figure 2.3. CO₂ emissions in thousands of metric tons per year by country in 2006.^{7,8}

Though the implementation of clean alternatives to fossil fuels, such as hydrogen or solar energy, would dramatically reduce society's CO₂ emissions, full implementation of these technologies to the point of relinquishing our dependence on fossil fuels is still far off. This is due to both the high energy density and abundance of fossil fuels as well as the technological and engineering problems which must be overcome in order to fully implement alternative fuels into everyday society. Meanwhile, carbon dioxide capture and storage (CCS) is the best option.

There has been a vast global effort to develop new technologies, methods and processes to effectively implement CCS from post-combustion effluents, e.g., flue gases.^{12,13} There are three steps of CCS: (i) separations of CO₂ from some gaseous exhaust mixture, (ii) transportation of the CO₂ to a storage site, (iii) and its permanent storage. While the latter two steps are fairly well developed, effectively and efficiently separating and capturing CO₂ is still a challenging task. This is especially true in the sequestration of carbon dioxide from exhaust streams of fossil fuel combustion in flue gases. This is because in smoke stacks,

the partial pressure of CO₂ is relatively low and the temperatures are high.

There are several methods that are being developed to selectively capture CO₂. These methods are categorized as chemical absorption, physical adsorption and chemical adsorption; of these, physical adsorption is proving to be one of the most promising, competitive and viable of these methods.⁹ In particular, CO₂ can be captured through adsorption into highly porous materials due to the relatively low energy requirements and broad applicability over a wide range of pressures and temperatures. Many types of these materials have been investigated for CO₂ separation and capture including inorganic molecular sieves (e.g., zeolites), carbon-based adsorbents (e.g., activated) carbon and organometallic crystals (e.g., Metal Organic Frameworks (MOFs)).¹⁴ MOFs, though relatively new, have been shown to have an enormous potential for CO₂ capture and storage. Under high pressures, MOFs are able to store nearly ten times the CO₂ of an empty container of the same volume. MOFs and, in particular, isoreticular metal-organic frameworks, which are described below, are the primary focus of this chapter of my thesis.

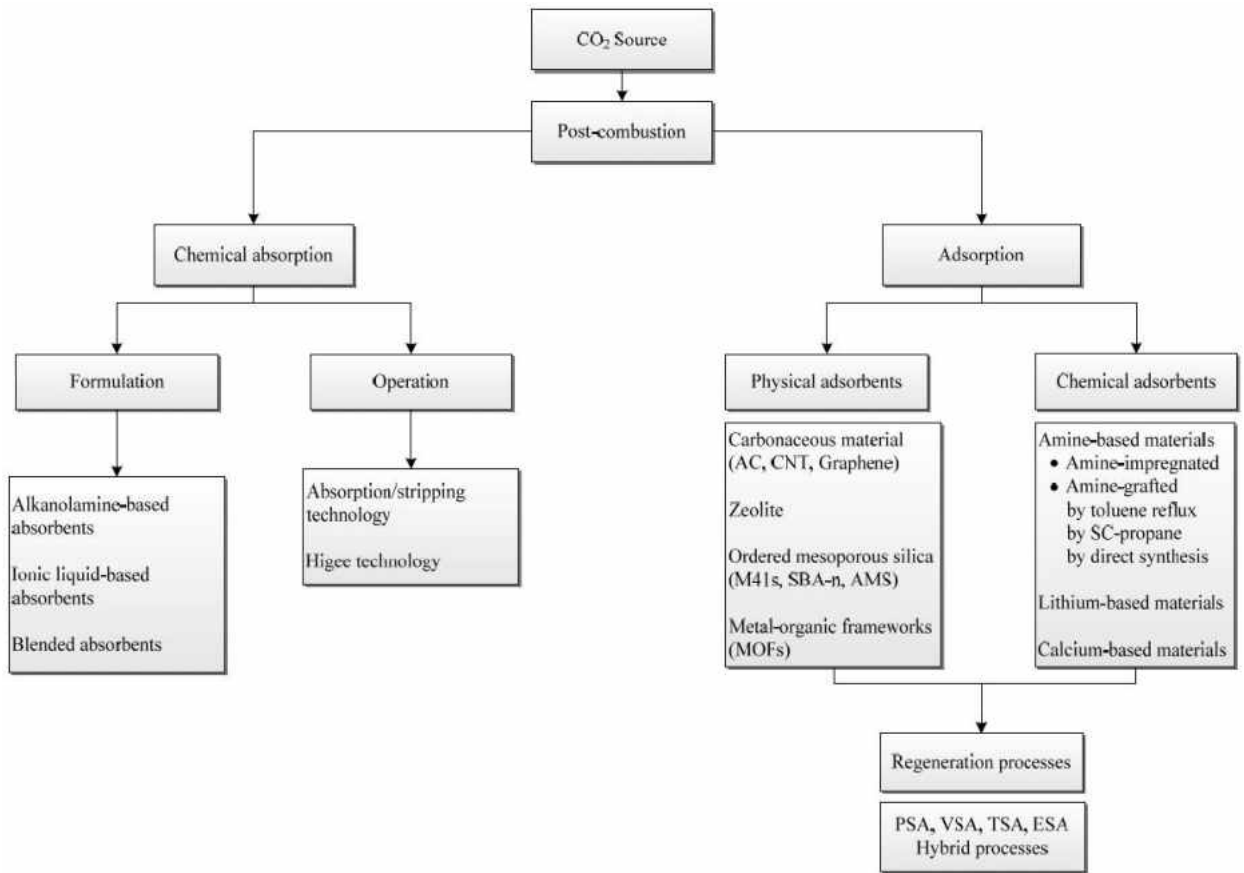


Figure 2.4. Flow chart showing the various methods available for CO₂ capture by absorption and adsorption. Figure taken from reference 9.

2.1.2 Porous Materials

The energy efficiency of CO₂ capture through physical adsorption, by means of materials such as carbonaceous adsorbents, zeolites, and MOFs, is much greater than both that of chemical absorption and chemical adsorption. This is because during the physical adsorption process, there are no new chemical bonds being formed or broken between the sorbate and sorbent, thus the material has a much lower regeneration costs.¹⁵

There are several types of reported carbonaceous adsorbents, with one of the most commonly used being activated carbon.¹⁶ Various carbonaceous adsorbents have already seen

significant use in CO₂ capture since they are widely available, have a high thermal stability, have a relatively low cost, and a low sensitivity to moisture. However, their effectiveness has been limited since they weakly adsorb CO₂ in the temperature range of 50-120°C and they possess a low CO₂/N₂ selectivity. Several common types of carbon-based adsorbents are given in Figure 2.5.

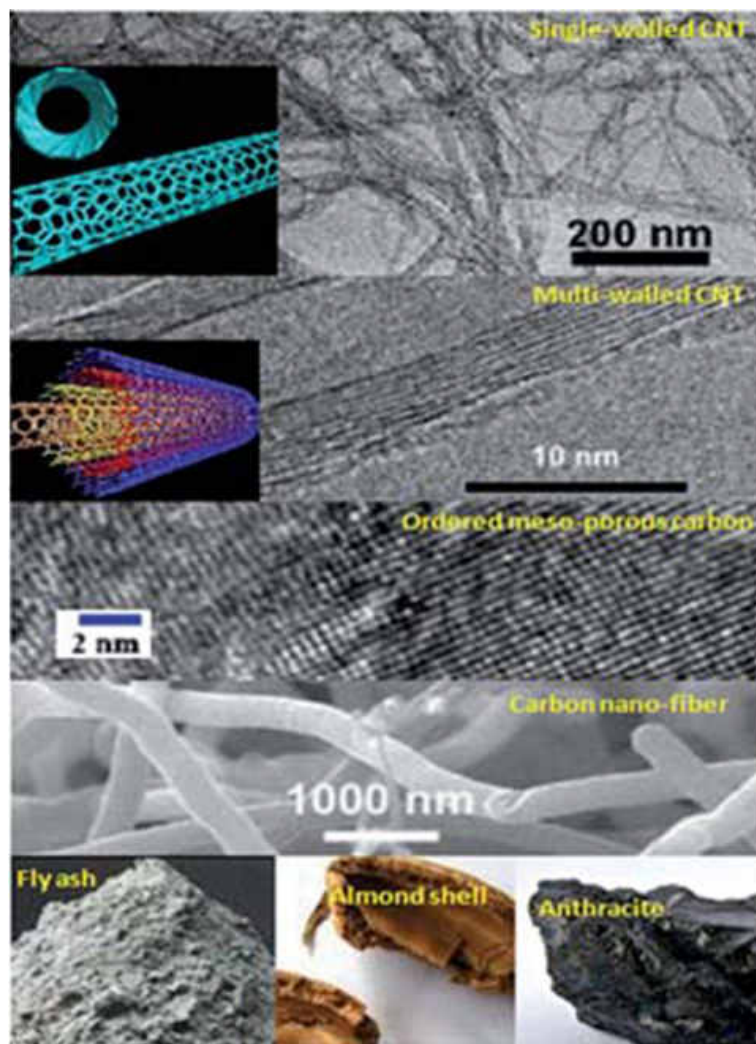


Figure 2.5. Various types of carbonaceous adsorbents. From top to bottom: single-walled CNT, multi-walled CNT, ordered meso-porous carbon, carbon nano-fiber, fly ash, almond shell and anthracite. This figure, which compiles figures taken from references 17–21, is a slightly modified version of figure 1 from reference 22.

However, zeolites, which are the most commonly used type of inorganic molecular sieve in CO₂ adsorption applications, show significantly higher selectivity. There have been many different zeolites reported for CO₂ capture, one example is given in Figure 2.6. The efficiencies of zeolites are primarily dictated by their charge density, size and the chemical composition of the cations in the porous structure of the zeolite.²² Though zeolites have several advantages, they also possess several drawbacks. Zeolites have a relatively low CO₂ loading capacity due to their active sites being highly hydrophobic. This results in a large decrease in CO₂ capacity in the presence of moisture while incurring an increased regeneration cost. However, while they are generally selective, their CO₂/N₂ selectivity is still relatively low. Therefore, there is an urgent need for an adsorbent material which possess both a large CO₂ capacity and a high selectivity toward CO₂. These challenges must be met if this pollutant is to be efficiently and effectively removed from fossil fuel exhaust. MOFs may be precisely what is needed for this task.

Over the last two decades a promising new crystalline porous material has surfaced and has become the focus of a wide variety of studies, namely MOFs.²⁴⁻²⁸ MOFs are made up of both organic and inorganic subunits. The organic subunit is known as the linker and is an organic molecule which possesses a functional group that is able to bind to the metal of the inorganic subunit. The inorganic subunit usually consists of a metal cluster and holds the structure together through strong coordination bonds. Though highly porous, these crystals have been shown to be robust enough to allow for the removal of the guest molecules without breaking down due to their well defined geometric structures, thus allowing for extensive reuse. Through the use of various diffraction methods, MOFs structures can be easily characterized²⁹ thus allowing for logical design of new MOFs. This design is based

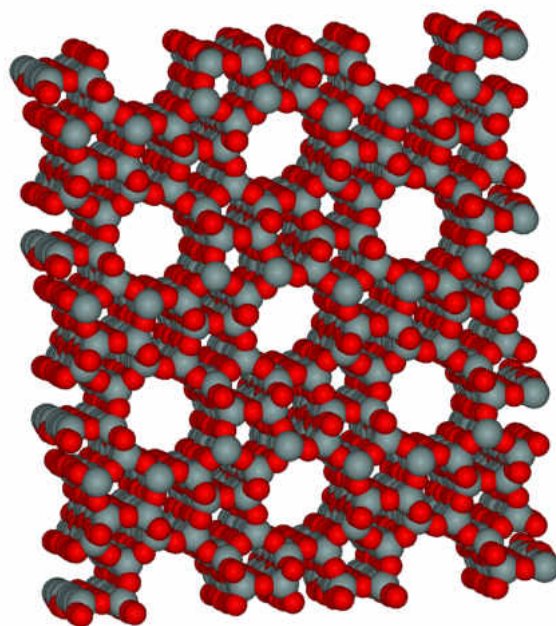


Figure 2.6. The microporous repeating molecular structure of ZSM-5, which is an aluminosilicate zeolite with a chemical formula is $\text{Na}_n\text{Al}_n\text{Si}_{96n}\text{O}_{192} \cdot 16\text{H}_2\text{O}$ (where $0 < n < 27$). Figure taken from reference 23.

on how the organic linkers and metal-containing nodes come together to form a lattice. An example of this is given in Figure 2.7.^{30,31} The properties of a MOF can be relatively easily tuned to best fit its desired application by changing one or both the subunits. This remarkable tunability gives MOFs a significant advantage over traditional adsorbents such as activated carbon or zeolites. Moreover, MOFs may prove to be the best candidate for CO_2 adsorption due to their remarkable tunability, incredibly low densities, thermal stability and incredibly high surface areas.

Since there are so many possible combinations of organic and inorganic subunits and since their design can be done quite logically, MOFs make an excellent potential solution to the problem of finding a porous crystal which can strongly adsorb CO_2 in a desired temperature range while still maintaining excellent selectivity for CO_2 . One such choice made

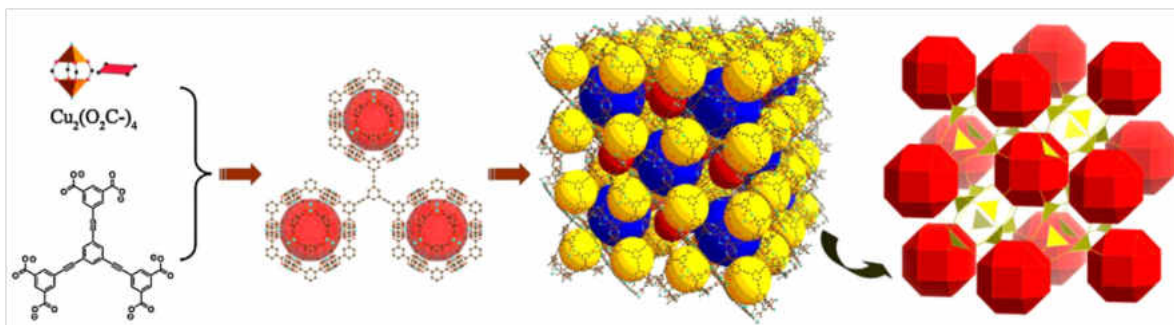
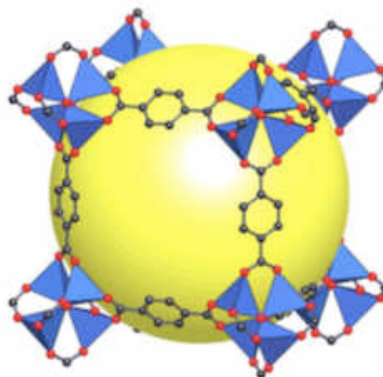


Figure 2.7. Construction of a MOF, from the organic and inorganic subunits to the main building unit and then to three-dimensional framework where the spheres represent the pores (i.e., the empty space available). The last image highlights the geometrical symmetry. This figure, which compiles figures taken from references 30 and 31, is taken from reference 29.

by Yaghi and coworkers¹⁴ led to the development of an entire new series of MOFs known as IsoReticular Metal Organic Frameworks (IRMOFs). These MOFs show an especially strong affinity for the encapsulation of CO₂. The design of the IRMOF series was based on MOF-5, which was synthesized by Yaghi and coworkers.¹⁴ The synthesis of IRMOF-1 was accomplished through the use of an N,N'-diethylformamide (DEF) solution mixture of Zn(NO₃)₂·4H₂O and the acid form of 1,4-benzenedicarboxylate (BDC) which was heated (360K to 378K) in a closed vessel yielding the crystalline MOF-5, Zn₄O(R1-BDC)₃ (where R1 = H). This MOF was later given the name IRMOF-1. This is shown in Figure 2.8.

In the same way as all MOFs, IRMOFs are made up of both organic and inorganic subunits. However, the MOFs which are part of the IRMOF series are included since they are considered to be isorecticular, i.e., they have this repeating netlike network throughout the entire crystal. As different organic linkers are used, the pore size of the IRMOF can change significantly. The first 16 IRMOFs are shown in Figure 2.9. Each of these IRMOFs have a vast amount of empty space inside the crystalline structure with free volume per-



$\text{Zn}_4\text{O}(\text{O}_2\text{C}-\text{C}_6\text{H}_4-\text{CO}_2)_3$: MOF-5

Figure 2.8. Synthesis of IRMOF-1. The yellow sphere represents the pore size. Reproduced from reference 14.

centages varying from 55.8% in IRMOF-5 to 91.1% in IRMOF-16.^{14,32} Also, it can be seen in Figure 2.9, some of the IRMOFs can form within each other, thus causing the unit cells to interlink. This is phenomena is called interpenetration. In Figure 2.10, the numerical values for the corresponding percent free volumes of the first 16 IRMOFs are given in increasing order.

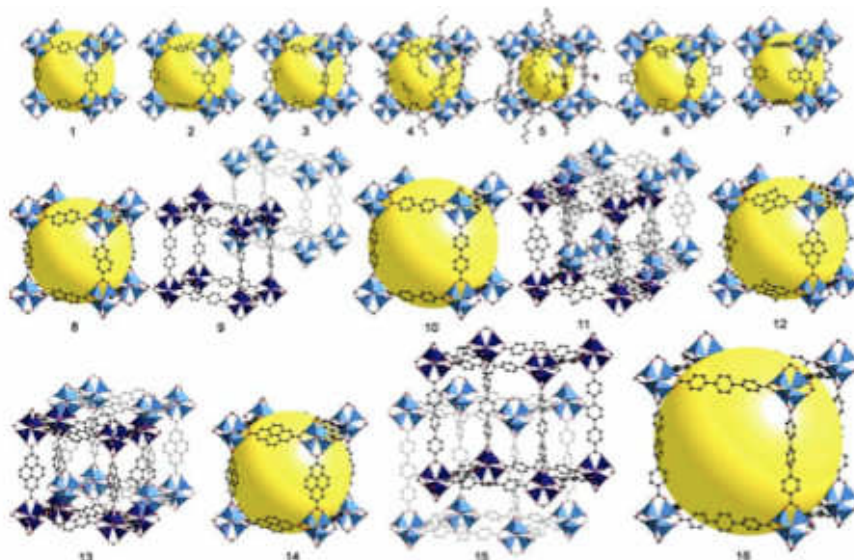


Figure 2.9. First 16 IRMOFs. The yellow spheres inside the IRMOFs represent the free volume. Figure taken from reference 33.

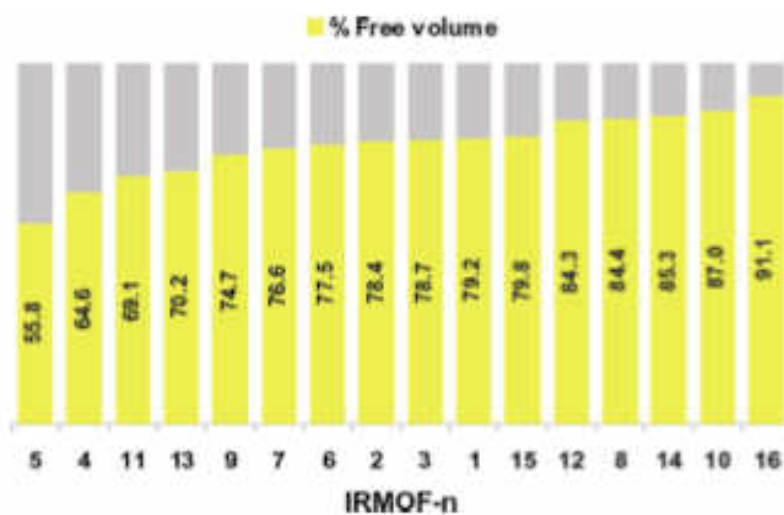


Figure 2.10. The percent free volumes in the first 16 IRMOFs. Figure taken from reference 33.

Though there has been great experimental efforts in characterizing, designing and testing various MOFs for the purpose of encapsulating CO₂ there have also been significant contributions to this end through computation. With the tremendous advances of computational power over the last few decades, the role that computational studies have been able

to play has become increasingly useful. It is on these methods and applications that the rest of this part of the thesis will focus.

2.1.3 State of the Art in Molecular Simulation

Molecular simulations have become a much welcomed complement to experiment, and in some cases, a necessary part in the search for a suitable IRMOF for CO₂ capture. This is because through molecular simulations, valuable microscopic information can be obtained that can be difficult or even impossible to obtain experimentally. Molecular simulations can be used to evaluate the performance of existing porous materials as well as hypothetical adsorbents. Furthermore, molecular simulations can be a valuable tool in the rational design of new crystalline materials to best suit specific applications, e.g., CO₂ adsorption.²⁹

The bulk of the computational effort which has been applied to CO₂ adsorption can be grouped into three main categories: *ab initio* calculations, Molecular Dynamics (MD) simulations and Monte Carlo (MC) simulations. The MC simulation methods primarily used are Grand Canonical Monte Carlo (GCMC) simulations and Grand Canonical Transition-Matrix Monte Carlo (GC-TMMC) simulations. Each of the above listed categories are summarized below.

Ab initio methods are used when pertinent information regarding any chemical or physical interaction is needed, e.g., interaction mechanisms, specific adsorption sites and interaction energies between MOFs and various small molecules, such as CO₂.^{34–38} When studying systems relevant to the adsorption of CO₂ into MOFs, the most common *ab initio* method used is density functional theory (DFT). The reason for this is that DFT includes electron correlation effects while still exhibiting remarkable computation efficiency and it

has been successfully applied to a wide range of system sizes. There are a large number of functionals available to DFT, however, B3LYP^{39,40} has been shown to give good approximations of binding geometries for many systems at a comparable level to that of higher level *ab initio* methods. However, when applied to systems that exhibit weak interactions, e.g., dispersion interactions, DFT has a lot of trouble, while traditional post-HF methods such as 2nd order Møller-Plesset perturbation theory (MP2)⁴¹ are able to adequately describe those systems. One draw back with MP2, however, is that it is relatively computationally expensive and thus it can only be applied to smaller systems. Therefore, when considering the relatively large MOF systems, it is crucial to use a balance between accuracy and efficiency by utilizing both low and higher level *ab initio* calculations.⁴² DFT, however, plays a highly important role in the study of CO₂ adsorption in another way. It can be used to provide force constants and atomic charges which can then be used in classical molecular simulations, e.g., calculation of atomic point charges used to develop force fields (FFs) used in the MD or GCMC methods described below.²⁹

In MD simulations Newton's Laws of motion are used and the system is followed through time. This method has proven to be quite useful for investigating the kinetic properties of the guest molecules in various porous materials, including the diffusion of CO₂ inside of MOFs. When the adsorption equilibrium properties are coupled with the kinetic properties, a powerful tool for the evaluation for the overall performance of the MOF is born. Currently, since there is very little experimental information available with regards to the diffusion of CO₂ in MOFs, MD is the primary means in which that valuable information can be obtained. In particular, MD is extremely helpful for screening and for designing MOFs for CO₂ separation, since it is extremely difficult to measure the diffusion

and transport properties of gas mixtures which may be present in flue gases. Typically in MD simulations, the MOF is assumed to be rigid and force fields are used to describe the nonbonding interactions of the atoms and/or molecules present in the system, which is also the way in which GCMC simulations are run.²⁹

In GCMC simulations,⁴³⁻⁶⁰ the grand canonical ensemble is randomly sampled according as described by the acceptance criteria. This method has been recognized as the most extensively used technique in the study of gas adsorption into MOFs and can yield results such as total gas uptake and the heats of adsorption. In the grand canonical ensemble the system will have a fixed chemical potential, μ , volume, V , and temperature, T while both the number of particles and the energy are allowed to fluctuate, Figure 2.11.

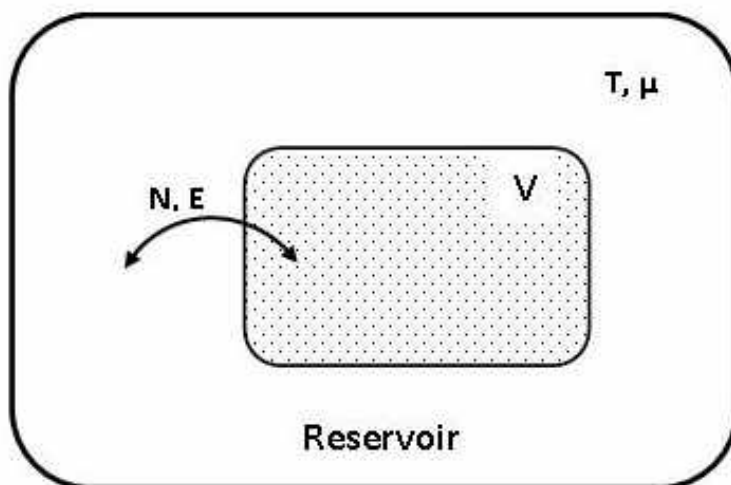


Figure 2.11. A pictorial representation of a GCMC simulation box. Both the number of particles and the energy are allowed to fluctuate, while the chemical potential, temperature and volume are kept constant. Figure taken from reference 61.

GCMC is a natural choice when studying adsorption since it allows for the modeling of the system when it is in equilibrium, where chemical potentials of the adsorbed phase

of the guest is the same as that for its gas phase. In GCMC, an adsorption isotherm can be generated, which is a graphical representation of the relationship between the number adsorbed into the porous material and the bulk activity of the adsorbate (e.g., chemical potential or pressure). In order to generate an adsorption isotherm using GCMC, about 20-30 different simulations are required at varying values of μ . An example of a five isotherms, computed by GCMC at different temperatures are shown in Figure 2.12. The pressure can be obtained for each value of μ through the use of an equation of state.

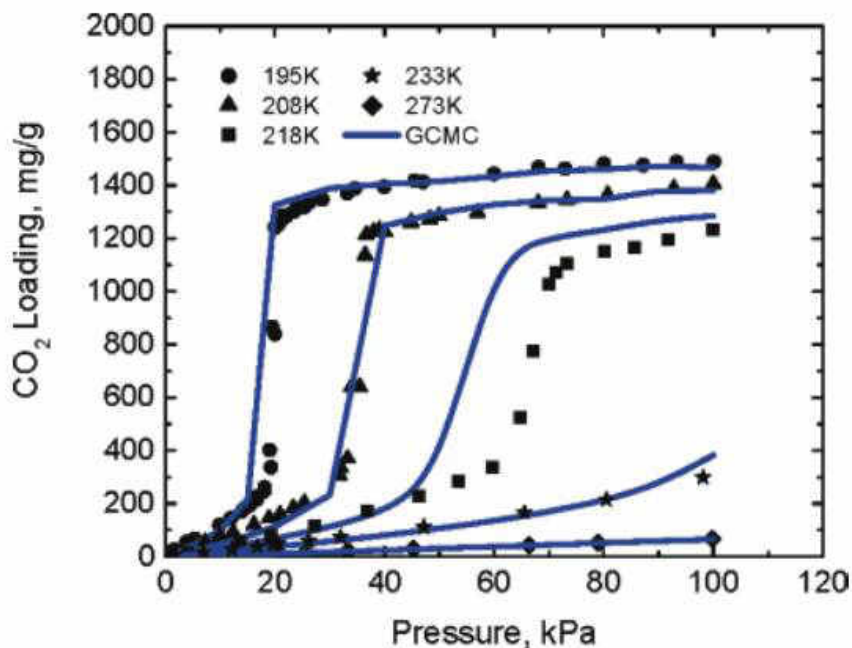


Figure 2.12. Five isotherms computed by CGMC and compared to experimental results. Figure taken from reference 50.

In a GCMC simulation, there are several types of acceptable MC trial moves, governed by the Metropolis acceptance criteria, which are given below. The acceptance criterion for a particle displacement from an old (o) position to a new (n) position in a system with a fixed number of particles N and volume V is given by⁶²

$$\text{acc}(o \rightarrow n) = \min [1, \exp(-\beta[U(\Gamma_o) - U(\Gamma_n)])] \quad (2.1)$$

where $U(\Gamma_o)$ is the internal energy of the old specific configuration of the system (before the move), $U(\Gamma_n)$ is the internal energy of the new specific configuration of the system (after the move) and $\beta = 1/k_B T$. The acceptance criterion for particle insertion in a system containing N particles is given by⁶²

$$\text{acc}(N \rightarrow N + 1) = \min \left[1, \frac{V}{\Lambda^3(N + 1)} \exp(\beta[\mu - U(N + 1) + U(N)]) \right] \quad (2.2)$$

where Λ is the thermal de Broglie wavelength. The acceptance criterion for particle deletion from a system containing N particles is given by⁶²

$$\text{acc}(N \rightarrow N - 1) = \min \left[1, \frac{\Lambda^3 N}{V} \exp(-\beta[\mu + U(N - 1) - U(N)]) \right] \quad (2.3)$$

Though GCMC has been shown to be able to produce adsorption isotherms in excellent agreement with experiment and in the case of gas mixtures predict the selectivity of the porous material being studied, GCMC often suffers from low acceptance of particle creation moves in the dense adsorbed phase, thus causing convergence issues and requiring the addition of enhanced sampling techniques.⁶² Furthermore, traditional GCMC can not readily obtain all of the relevant thermodynamic properties, thus creating additional complications when a complete thermodynamic characterization of the system is desired.

Very recently, the Grand Canonical Transition-Matrix Monte Carlo (GC-TMMC) simulation method was developed for simulating adsorptions of gases into porous materials.⁶³

Traditionally, TMMC is a simulation method that provides uniform sampling.^{64–69} This method only requires a rough estimate of the pressure or chemical potential for phase co-existence *a priori*, which can be obtained easily with a few short preliminary simulations, and has been shown to be highly precise.^{70–74} The GC-TMMC method’s key advantage is that it can generate the entire adsorption isotherm in a single simulation;⁶³ however, it can be relatively time consuming, which can be undesirable when simulating relatively large, complicated systems. Yet, when GCMC simulations are coupled with Wang-Landau (WL) sampling, the drawbacks of both GCMC and GC-TMMC can be overcome and the way that this is accomplished is presented below.

2.2 WANG-LANDAU SAMPLING

Wang-Landau (WL) sampling,^{75,76} is a flat histogram sampling method of the “visited states” class.⁷⁷ Originally the WL method, being that it originated in solid state physics, was applied only to lattice systems.^{75,76} However, more recently it has been applied to off-lattice simulations,^{78,79} formulated to work in various statistical ensembles,^{80,81} applied in the study of vapor-liquid equilibrium^{77,81–87,92} and to the adsorption of atoms and molecules into IRMOF-1.^{93,94} When applied to the adsorption into IRMOFs, WL sampling is used in the grand canonical (μ, V, T) ensemble. It is in that ensemble that many of the advantages WL has over other methods will be highlighted.

With WL, all energies (or in the case of the (μ, V, T) ensemble, all N ’s) available to the system are sampled evenly, which is highly advantageous over conventional MC methods. In traditional MC, Boltzmann sampling is used, in which there is a very low probability for

the system to have a value of the order parameter in between the values for the vapor and liquid states; thus the simulation will get stuck in one state or the other. This issue is shown in Figure 2.13. When WL sampling is used, it biases the probability function so that it has the same value for some specified range of the order parameter, allowing for easy sampling across to both phases. This is shown in Figure 2.14.

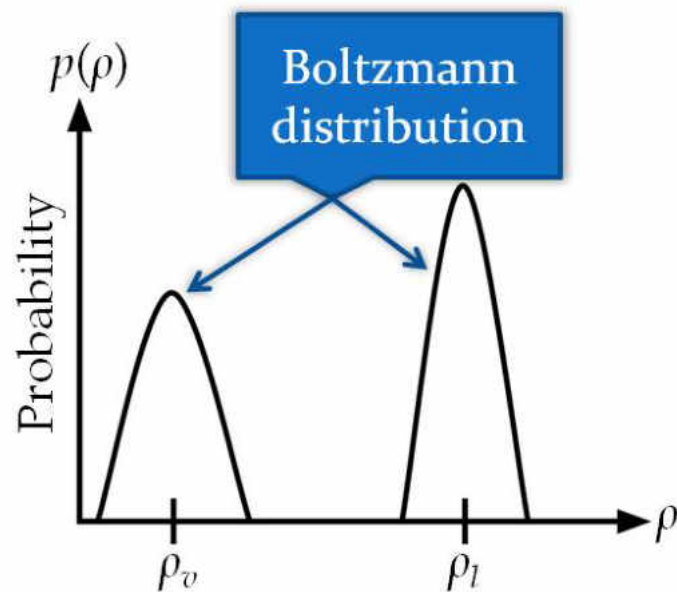


Figure 2.13. When regular Boltzmann sampling is used, the sampling gets trapped in either the vapor or liquid phases (ρ_v and ρ_l respectively) since the probability of the system being in between the two states is near zero.

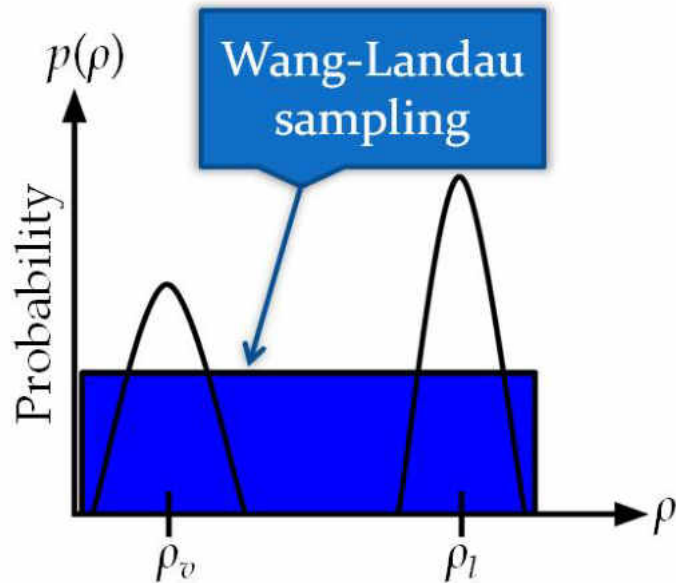


Figure 2.14. When WL sampling is used, all states of the system can be equally sampled. There is no longer any issue traversing from one phase to another since the probability is the same for all values of the order parameter ρ for the entire range the user specifies.

With WL sampling there is no need to run trial-and-error simulations since neither the pressure or chemical potential for phase coexistence must be known *a priori*, which is a great advantage over parallel tempering and multicanonical sampling.⁷⁷ The reason for this will be shown in detail later on in this thesis, but simply put it is because the chemical potential, μ , is canceled from the Metropolis acceptance criteria when the WL biased probability distribution is used. This is also a minor advantage over the TM method, but one of WL sampling's major advantages over the TM method is that it can obtain comparable results much faster. Also since μ is not needed *a priori*, only one simulation run is needed to obtain the entire adsorption isotherm, which is a definite advantage over using GCMC without WL sampling.

Though the above advantages are important, the primary advantage is that, through the formalism of statistical thermodynamics, all the thermodynamic properties of the system

can be calculated over a wide range of conditions from a single simulation run. Additionally, when the solution thermodynamics treatment of adsorption into porous materials of Myers and co-workers⁹⁵⁻⁹⁷ is applied, both the absolute and excess thermodynamic properties can be obtained⁹³ as well as the immersion and desorption thermodynamic functions.⁹⁴ These properties are crucial in characterizing the adsorbent, since, as stated by Myers,⁹⁶ the desorption free energy, enthalpy and entropy provide a complete thermodynamic description of the system. Additionally, the desorption free energy is of special significance from a practical stand point, since it can be interpreted as the minimum isothermal work required to remove the adsorbent from an IRMOF. In particular, the majority of the operating cost in adsorbing pollutants into IRMOFs is in the degassing step, thus the desorption free energy is one way to measure the performance of various IRMOFs.

2.2.1 Quantum Origins

To fully understand Wang-Landau sampling one must first go back to when the method was in its infancy, where it was first proposed by Wang and Landau as a random walk algorithm for Monte Carlo to directly calculate the density of states.^{75,76} As stated in the previous section, WL sampling originated in solid state physics and was initially only applied to lattice systems,^{75,76} in particular the 2D ten state Potts model and Ising model which correspond to 1st- and 2nd-order phase transitions, respectively. These quantized systems were chosen to demonstrate the efficiency and accuracy of WL sampling. The Ising $L \times L$ square lattice with nearest neighbor coupling was used since it is generally viewed as an ideal benchmark for new theories⁹⁸ and simulations algorithms.⁹⁹⁻¹⁰¹ The 2D ten state Potts model¹⁰² with nearest neighbor coupling on square lattices was used to

show how WL sampling can be used to overcome the above mentioned low probability region (i.e., the energetic barrier) that arises between two phases in coexistence at a 1st-order phase transition. A schematic representation of the Ising and Potts models is given in Figure 2.15.

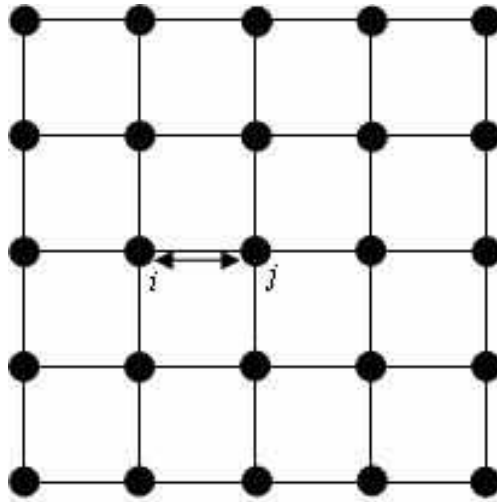


Figure 2.15. Schematic of a 5x5 Ising or 2D Potts model. Figure taken from reference 61

For both of these models, only the interactions of nearest neighbors are considered since solely these interactions contribute to the energy of the system, E . The way these interactions are treated is one way in which the Ising and Potts models differ. In the Ising model, each interaction site is assigned either a +1 or -1, reminiscent of a particle with either spin up or spin down. The spin is denoted σ_i with $i = 1, 2, \dots, N$ where N is the total number of interaction sites in the system. The values of σ_i build the energy space of the system and the Hamiltonian of the system is given by

$$\mathcal{H} = - \sum_{\langle i,j \rangle} J_{ij} \sigma_i \sigma_j \quad (2.4)$$

where J_{ij} is the unit energy of the neighboring interaction and is set equal to 1 for simplicity and the sum $\sum_{\langle i,j \rangle} J_{ij}$ is only over all the neighboring pair interactions.

In the Potts model, which is in a sense a generalization of the Ising model, the interaction sites have 10 possible states, rather than just spin up or spin down. These independent variables are denoted $q_i = 1, 2, \dots, 10$ and again $i = 1, 2, \dots, N$ with N being the total number of interaction sites in the system. Similarly to the Ising model, the values of q_i build the energy space of the system and the Hamiltonian of the system is

$$\mathcal{H} = - \sum_{\langle i,j \rangle} J_{ij} \delta(q_i, q_j) \quad (2.5)$$

where $\delta(q_i, q_j)$ is a delta function and as defined above the unit energy J_{ij} is set to one for each interaction for simplicity. WL sampling applied to these models will be expanded upon further below, but first, the algorithm by which the WL method obtains the density of states, $g(E)$, is given.

As mentioned before, WL sampling accurately estimates the density of states, $g(E)$, through a random walk which produces a flat histogram in energy space. This differs from conventional Monte Carlo methods, which directly generate a canonical distribution at a given temperature $g(E)e^{-E/k_B T}$, where k_B is the Boltzmann constant. In WL sampling, the density of states is unknown *a priori*, so $g(E)$ is set equal to unity and, via the steps outlined below, is estimated.

1. $g(E)$ is first set to 1 for all values of E .
2. As the simulation proceeds, the current estimate of $g(E)$ is used.
3. When a specific E is sampled, $g(E)$ is updated: $g(E) \rightarrow f \times g(E)$ where f is initially

set to e (i.e., Euler's number).

4. At the same time a histogram that keeps track of the visited values of E , $H(E)$, is kept during the simulation and is set to zero for all values of E .
5. Since $g(E)$ is dynamically updated, the simulation is always pushed away from the current value of E to a new one.
6. Thus the histogram, $H(E)$, eventually becomes close to being flat (e.g., $H(E)$, for all possible E , is not less than 80% of the average histogram $\langle H(E) \rangle$).
7. When this happens, $f \rightarrow f^{A/2}$ and $H(E)$ is set back to zero.
8. The simulation will converge once f is arbitrarily close to unity and the updates of $g(E)$ are negligible, thus an estimate of $g(E)$ is obtained.

Now, in order to obtain uniform sampling over all desired energies, whether using the Ising or Potts model, one must have a biased joint probability function. If the sampling is performed without a biased joint probability, the simulation will be excessively long since the density of states would only converge after all states are visited. The states are visited by sampling the various configurations in energy space. This is done by flipping the spin in the Ising model or by assigning one of the ten possible variables in the Potts model of an interaction site. In a 10×10 lattice there are $2^{100} \approx 1.27 \times 10^{30}$ states in the Ising model and in the Potts model there are $10^{100} = 1.00 \times 10^{100}$ states. Thus having a biased probability makes the calculation feasible. The general form of the biased probability function is

$$p_{bias}(\mathbf{\Gamma}, E) = \frac{p(\mathbf{\Gamma}, E)}{p(E)} \quad (2.6)$$

where $\mathbf{\Gamma}$ denotes a specific configuration of the system and $p(\mathbf{\Gamma}, E)$ is the probability of the system being in a given configuration in energy space and is given by

$$p(\mathbf{\Gamma}, E) = \frac{\exp(-E(\mathbf{\Gamma})/k_B T)}{Z} \quad \text{where } Z = \sum_{\mathbf{\Gamma}} \exp(-E(\mathbf{\Gamma})/k_B T) \quad (2.7)$$

where Z is the system partition function and the sum is over all the possible configurations of energy space. Now, by summing over the configurations associated with a particular energy one can obtain the probability density at a given energy, which is given by

$$p(E) = \sum_{\mathbf{\Gamma} \in E} \frac{\exp(-E(\mathbf{\Gamma})/k_B T)}{Z} = \frac{g(E)\exp(-E/k_B T)}{Z} \quad (2.8)$$

where $g(E)$ is the density of states which can also be perceived as the degeneracy of a specific energy level, E . Thus, for the Ising and Potts model, the biased joint probability function is

$$p_{bias}(\mathbf{\Gamma}, E) = \frac{p(\mathbf{\Gamma}, E)}{p(E)} = \frac{1}{g(E)} \quad (2.9)$$

and the biased probability for a specific energy level is the same for all of the energy phase space and is given by

$$p_{bias}(E) = \sum_{\mathbf{\Gamma} \in E} p_{bias}(\mathbf{\Gamma}, E) = 1 \quad (2.10)$$

Therefore, with the probability proportional to the reciprocal of the density of states, a flat histogram can be generated for the energy distribution. As the simulation commences as outlined above, the system will visit specific configurations with the transition probability (i.e., the probability of the system to transition from state 1 with its energy equal to E_1 to state 2 with its energy equal to E_2) is given by

$$p(E_1 \rightarrow E_2) = \min \left[\frac{g(E_1)}{g(E_2)}, 1 \right] \quad (2.11)$$

This can also be given in the form of the Metropolis acceptance criterion for moving from an old configuration in energy space with the system's energy equal to E_o to a new configuration with the system's energy equal to E_n , given as

$$\text{acc}(o \rightarrow n) = \min \left[\frac{g(E_o)}{g(E_n)}, 1 \right] \quad (2.12)$$

It is important to note that the WL algorithm, during the random walk, does not exactly satisfy the detailed balance condition from which the acceptance criterion in eq 2.11 is derived, but is given by

$$\frac{1}{g(E_1)} p(E_1 \rightarrow E_2) = \frac{1}{g(E_2)} p(E_2 \rightarrow E_1) \quad (2.13)$$

This is because the density of states is continuously modified during the random walk in energy space.^{75,76} However, as the modification factor, f , approaches 1 after many iterations, the density of states converges to the true value very quickly. Thus it can be concluded that the detailed balance condition is met to within the accuracy proportional to

$\ln(f)$.

Once the density of states is obtained, the WL method enables one to access a broad range of properties. The canonical distribution at a specific temperature can be found by

$$p(E, T) = \frac{g(E)e^{-E/k_B T}}{Q} \quad (2.14)$$

where Q is the partition function of the system.

It is worth highlighting that the density of states obtained is independent of temperature and thus from a single simulation run any temperature dependent distribution can be obtained. One such distribution is given in Figure 2.16 which was obtained for various sizes of an $L \times L$ 2D ten state Potts model. The double peaked distribution, where the peaks have equal heights, is due to the fact that the transition temperature, T_c , is reached for the various sizes of the lattice system. As the size of the system increases, the valley depth increases. It is here that conventional MC algorithms will have considerable trouble and shows a considerable limitation for other methods to study first order phase transitions. For a lattice of size $L = 200$, we have that $P(E, T_c)$ is as low as 9×10^{-10} and a tunneling barrier of that magnitude makes the calculation unfeasible for conventional MC methods to overcome with modern day computational power. Therefore, WL sampling is a valuable tool when simulating phase coexistence.

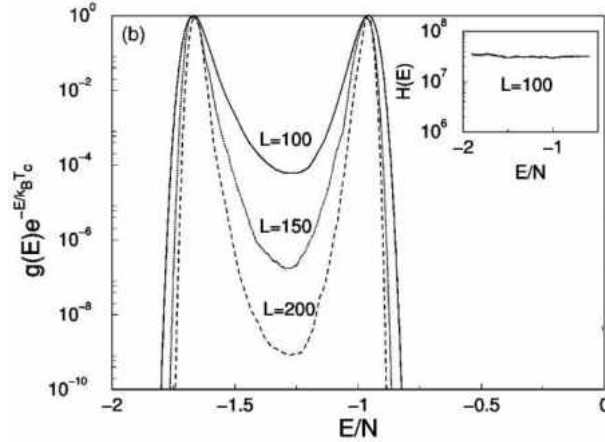


Figure 2.16. The canonical distribution at the transition temperature for various L sizes of the 2D ten Potts model. The histogram of visited states for $L = 100$ is shown in the inset. Figure taken from reference 75

As stated above, WL sampling was also applied to $L \times L$ 2D Ising model in order to test its convergence and accuracy with a 2nd order phase transition by comparing to exact solutions. The density of states distribution obtained from the utilization of the WL method along with the comparison with the results obtained by the Beale method¹⁰³ is given in Figure 2.17. There is no visible difference that can be seen between the simulation and exact density of states; this is due to the remarkably low relative error $\varepsilon(X)$ which is generally defined for any quantity X by

$$\varepsilon(X) \equiv \left| \frac{X_{sim} - X_{exact}}{X_{exact}} \right| \quad (2.15)$$

Its distribution is presented in the inset of Figure 2.17 and it gets as low as 0.035 % on the 32×32 lattice.

Then, from the highly accurate density of states, many thermodynamic quantities can be calculated through the formalism of statistical mechanics. Two particularly interesting

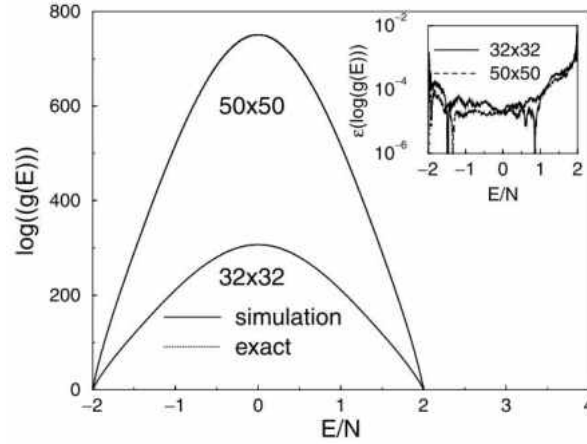


Figure 2.17. The density of states obtained via WL sampling along with exact results obtained by Beale's method.¹⁰³ The inset shows the relative error ($\varepsilon(\log[\Omega(E)])$). Figure taken from reference 75

quantities, being that they are not directly available from conventional MC simulations, is the Gibbs free energy and the entropy. The Gibbs free energy can be readily calculated from the density of states by

$$G(T) = -k_B T \ln(Q) \quad (2.16)$$

where

$$Q = \sum_E g(E) \exp(-E/k_B T) \quad (2.17)$$

Similarly, the internal energy of the system can be obtain by

$$U(T) = \frac{\sum_E E g(E) \exp(-E/k_B T)}{Q} \quad (2.18)$$

Then, from the Gibbs free energy and the internal energy, the canonical entropy can be calculated via

$$S(T) = \frac{U(T) - G(T)}{T} \quad (2.19)$$

Another useful quantity, the specific heat capacity, can be calculated from the fluctuations of the internal energy with respect to temperature fluctuations

$$C(T) = \frac{\partial U(T)}{\partial T} = \frac{\langle E^2 \rangle - \langle E \rangle^2}{k_B T^2} \quad (2.20)$$

Each of the above calculated thermodynamic properties were shown to be highly accurate for the broad range of temperatures that was analyzed for the 2D Ising model, i.e., $T = 0 - 8$.⁷⁶ Thus WL sampling was shown to be both efficient as well as accurate while retaining an excellent generality for lattice systems and more recently WL sampling was applied to off-lattice simulations.

2.2.2 Formalism for Classical Systems

Wang-Landau sampling has also been shown to produce excellent results for off-lattice classical systems in various ensembles. In this section, the way in which Wang-Landau sampling can be applied in the uniform sampling of V through the use of the isothermal-isobaric ensemble (N, P, T) as well as the uniform sampling of N through the grand-canonical ensemble (μ, V, T) will be discussed. The methodology used in the isothermal-isobaric ensemble will be discussed first.

In order to obtain a biased simulation which uniformly samples the volume, V , while N and T are fixed, a biased joint probability function must be used.⁷⁷ This can be obtained in the same way as shown above, where

$$p_{bias}(\mathbf{\Gamma}, V) = \frac{p(\mathbf{\Gamma}, V)}{p(V)} \quad (2.21)$$

Now, in the isothermal-isobaric (N, P, T) ensemble, the joint Boltzmann distribution of $\mathbf{\Gamma}$ and V is given by

$$p(\mathbf{\Gamma}, V) = \frac{V^N \exp(-\beta U(\mathbf{\Gamma}) - \beta PV)}{N! \Lambda^{3N} Q(N, P, T)} \quad (2.22)$$

where $\beta = \frac{1}{k_B T}$, $\Lambda = h / \sqrt{2\pi m k_B T}$ is the thermal de Broglie wavelength, $U(\mathbf{\Gamma})$ is the internal energy of the system of N molecules in the specific configuration, $\mathbf{\Gamma}$, and

$$Q(N, P, T) = \int_0^\infty Q(N, V, T) \exp(-\beta PV) dV \quad (2.23)$$

is the isothermal-isobaric partition function and the volume distribution is given by

$$p(V) = \int p(\mathbf{\Gamma}, V) d\mathbf{\Gamma} = \frac{Q(N, V, T) \exp(-\beta PV)}{Q(N, P, T)} \quad (2.24)$$

Now, the biased distribution can be obtained by substituting eqs 2.22 and 2.24 into eq 2.21 and after simplification,

$$p_{bias}(\mathbf{\Gamma}, V) = \frac{V^N \exp(-\beta U(\mathbf{\Gamma}))}{N! \Lambda^{3N} Q(N, V, T)} \quad (2.25)$$

where $p_{bias} = \int p_{bias}(\mathbf{\Gamma}, V) d\mathbf{\Gamma} = 1$. Then, the detailed balance condition is

$$\frac{V_o^N \exp(-\beta U(\mathbf{\Gamma}_o))}{N! \Lambda^{3N} Q(N, V_o, T)} \text{acc}(o \rightarrow n) = \frac{V_n^N \exp(-\beta U(\mathbf{\Gamma}_n))}{N! \Lambda^{3N} Q(N, V_n, T)} \text{acc}(n \rightarrow o) \quad (2.26)$$

where $\text{acc}(o \rightarrow n)$ is the probability of accepting a trial move from an old state, o to a new state, n . The Metropolis solution to eq 2.26 is the the Metropolis acceptance criteria and is given by⁷⁷

$$\text{acc}(o \rightarrow n) = \min \left[1, \frac{Q(N, V_o, T)}{Q(N, V_n, T)} \times \frac{V_n^N \exp(-\beta U(\mathbf{\Gamma}_n))}{V_o^N \exp(-\beta U(\mathbf{\Gamma}_o))} \right] \quad (2.27)$$

Notice that pressure disappears from the scheme, thus it does not need to be known *a priori*.

Now, the biasing function needed to achieve uniform sampling of V is the canonical partition function, $Q(N, V, T)$, with N and T fixed. However, in most applications, rather than uniformly sampling V , it is more convenient and simpler to sample $\ln[V]$ uniformly. In this case, the factors of V^N should be replaced by V^{N+1} in eq 2.27.⁷⁷ The WL algorithm in the isothermal-isobaric ensemble is given below:

1. $Q(N, V, T)$ is first set to 1 for all values of V .
2. As the simulation proceeds, the current estimate of $Q(N, V, T)$ is used.
3. When a given interval of $\ln[V]$ is sampled, $Q(N, V, T)$ is updated: $Q(N, V, T) \rightarrow f \times Q(N, V, T)$ where f is initially set to e (i.e., about 2.72).
4. At the same time a histogram that keeps track of the visited values V , $H(V)$, is kept during the simulation and is initially set to zero for all values of V . When a specific value of V_i is reached during the simulation, the value of $H_o(V_i)$ is updated to $H_o(V_i) + 1 = H_n(V_i)$.
5. Since $Q(N, V, T)$ is dynamically updated, the simulation is always pushed away from the current value of V to a new one.

6. Thus the histogram, $H(V)$, eventually becomes close to being flat (e.g., $H(V)$, for all possible V , is not less than 80% of the average histogram $\langle H(V) \rangle$).
7. When this happens, $f \rightarrow f^{A/2}$ and $H(V)$ is set back to zero for all values of V .
8. The simulation will converge once f is arbitrarily close to unity and the updates of $Q(N, V, T)$ are negligible, thus an estimate of $Q(N, V, T)$ is obtained, and an example of what this looks like is given in Figure 2.18.

It is worth mentioning that the convergence of the Wang-Landau algorithm has been formally proven.⁸⁸ This method has been shown to be particularly well suited to study phase transitions since this uniform sampling easily overcomes the free energy barriers associated with the interfaces which form, e.g., between the liquid and vapor states. Consequently, WL sampling in the NPT ensemble has been used with great success in studies of vapor-liquid equilibria of the Lennard-Jones fluid,^{78,80,81} various complex fluids^{77,83} and molecular fluids.^{82,85}

In reference 85, Hybrid Monte Carlo (HMC)^{89,90} in the NPT ensemble was combined with WL sampling to both parametrize a force field for polycyclic aromatic hydrocarbons (PAHs) and to show the accuracy that the WL sampling provides for the vapor-liquid equilibria of the PAHs studied, i.e., naphthalene, phenanthrene and anthracene. In HMC, the random moves of MC are replaced by a MD trajectory in the (N, V, E) ensemble. This ensures that the system will be sampled efficiently even at high densities when simulating in the (NPT) ensemble. In the above mentioned study, the results were in good agreement with experimental values and the model was shown to give a better account for the temperature dependence of the vapor pressure, which is a crucial property for airborne pollutants

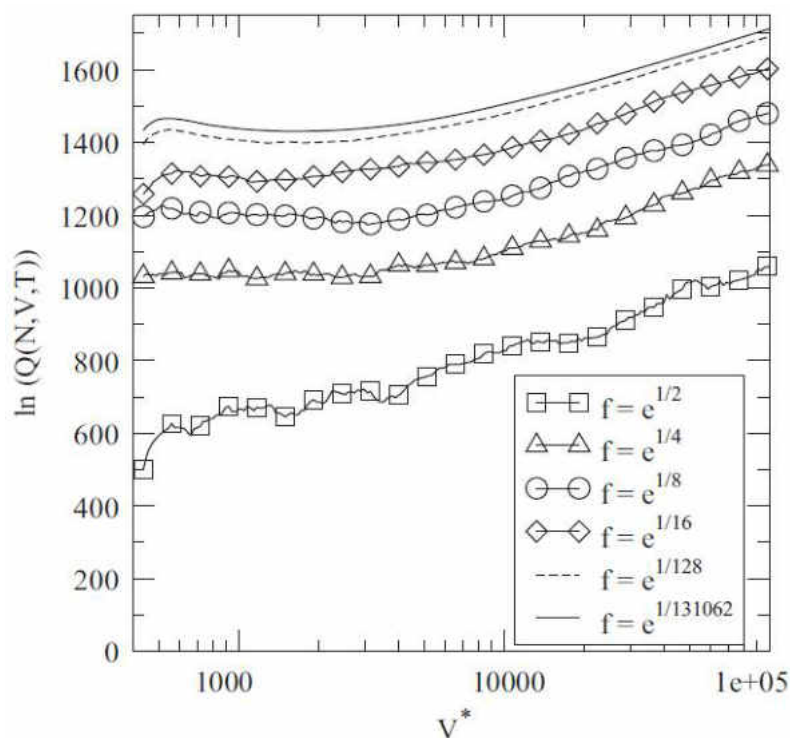


Figure 2.18. Converging estimates of $\ln(Q(N, V, T))$ which draw closer to the true value up to a multiplicative constant as f draws closer to unity.⁸⁵

such as PAHs and CO_2 , than previously used models. The convergence of the biasing function, $Q(N, V, T)$ is shown in Figure 2.18. The vapor-liquid coexistence curve obtained in the study is plotted in Figure 2.19. Also, in Table 2.1 a numerical comparison from the HMC WL results⁸⁵ are compared to experimental results⁹¹ for naphthalene. Uncertainties in the simulated properties are of the order of 10^{-3}g cm^{-3} for densities and of the order of 0.1 bar for vapor pressure. It can be seen that the results are in excellent agreement. This was also found to be the case for both phenanthrene and anthracene.⁸⁵

Wang-Landau sampling has also been shown to work very well in the grand canonical ensemble.⁷⁷ As stated above, the grand canonical ensemble is used when studying adsorption into IRMOFs. The reason for this is that in this ensemble, the chemical potential,

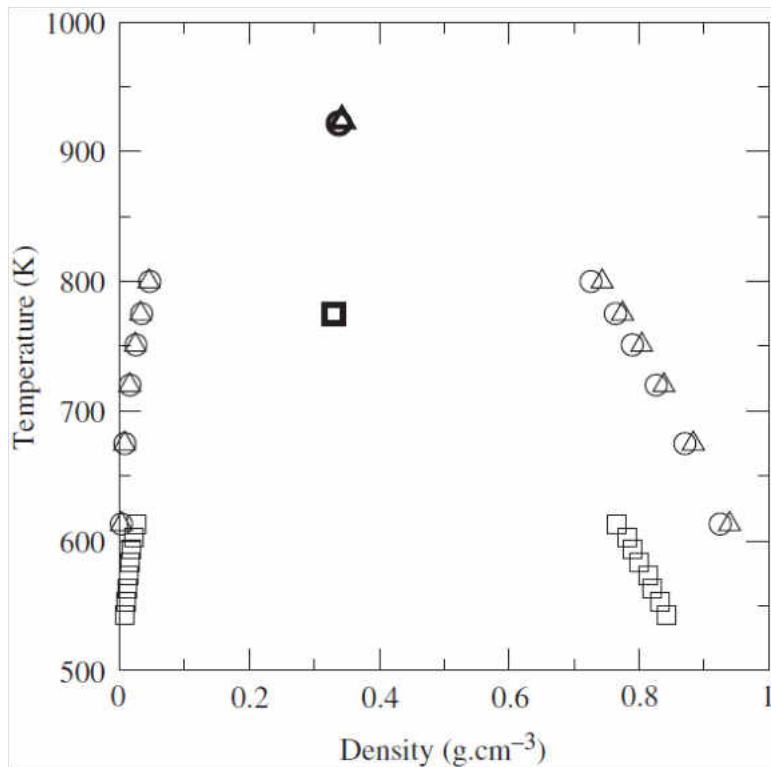


Figure 2.19. Vapor-liquid equilibria for naphthalene (\square), anthracene (\circ) and phenanthrene (\triangle). Estimates for the critical point are plotted in bold.⁸⁵

μ , the volume, V , and the temperature T are held constant which are quite natural conditions when modeling adsorption into IRMOFs, save for the fixed μ . However, with WL sampling this is no longer an issue. Using WL sampling in the grand canonical ensemble when studying adsorption is advantageous. Once the grand canonical partition function is obtained, a wealth of information about the system can be extrapolated and, in particular, all the relevant thermodynamic properties. The grand canonical partition function is given by

$$\Theta(\mu, V, T) = \sum_{N=0}^{\infty} Q(N, V, T) \exp(\beta\mu N), \quad (2.28)$$

where μ is the chemical potential, $\beta = \frac{1}{k_B T}$, N is the particle number and $Q(N, V, T)$ is the

Table 2.1. Densities of the liquid and vapor phases of naphthalene at coexistence as well as the vapor pressure from HMC WL⁸⁵ and experimental data.⁹¹

Temperature (K)	$\rho_{sim,liq}$ (g cm ⁻³)	$\rho_{exp,liq}$ (g cm ⁻³)	$\rho_{sim,vap}$ (g cm ⁻³)	$\rho_{exp,vap}$ (g cm ⁻³)	P_{sim} (bar)	P_{exp} (bar)
613	0.766	–	0.0256	0.0218	8.56	9.05
603	0.781	–	0.0218	0.0194	7.32	7.86
593	0.790	0.794	0.0189	0.0170	6.32	6.79
583	0.800	0.804	0.0162	0.0150	5.42	5.82
573	0.815	0.812	0.0136	0.0129	4.57	4.97
563	0.821	0.820	0.0118	0.0123	3.90	4.23
553	0.832	0.827	0.0097	0.0118	3.19	3.57
543	0.842	0.835	0.0082	0.0094	2.69	2.99

canonical partition function. So, this function must be found in order to obtain the grand canonical partition function. The canonical partition function is given by

$$Q(N, V, T) = \frac{V^N}{N! \Lambda^{3N}} \int \exp(-\beta U(\mathbf{\Gamma})) d\mathbf{\Gamma} \quad (2.29)$$

where $\Lambda = h / \sqrt{2\pi m k_B T}$ is the thermal de Broglie wavelength and $U(\mathbf{\Gamma})$ is the internal energy of the system of N molecules in the specific configuration, $\mathbf{\Gamma}$. The integration is performed over $\mathbf{\Gamma}$, thus over the coordinates of the N molecules of the system. Now in order to obtain an accurate estimate for the canonical partition function when dealing with phase coexistence, both phases must be adequately sampled. Thus the uniform sampling of the WL method is perfect for this task.

In order to uniformly sample all desired values of the order parameter $\rho=N/V$, we must have a biased joint probability function as a function of N , since we are operating in the grand canonical ensemble, which sums over all values of N . This biased joint probability function is

$$p_{bias}(\mathbf{\Gamma}, N) = \frac{p(\mathbf{\Gamma}, N)}{p(N)} \quad (2.30)$$

where the particle number distribution is given by

$$p(N) = \int p(\mathbf{\Gamma}, N) d\mathbf{\Gamma} = \frac{Q(N, V, T) \exp(\beta\mu N)}{\Theta(\mu, V, T)} \quad (2.31)$$

and the joint probability distribution is

$$p(\mathbf{\Gamma}, N) = \frac{V^N \exp(\beta\mu N - \beta U(\mathbf{\Gamma}))}{N! \Lambda^{3N} \Theta(\mu, V, T)} \quad (2.32)$$

and when eqs 2.31 and 2.32 are substituted into eq 2.30, we get

$$p_{bias}(\mathbf{\Gamma}, N) = \frac{p(\mathbf{\Gamma}, N)}{p(N)} = \frac{\frac{V^N \exp(\beta\mu N - \beta U(\mathbf{\Gamma}))}{N! \Lambda^{3N} \Theta(\mu, V, T)}}{\frac{Q(N, V, T) \exp(\beta\mu N)}{\Theta(\mu, V, T)}} = \frac{V^N \exp(-\beta U(\mathbf{\Gamma}))}{Q(N, V, T) N! \Lambda^{3N}} \quad (2.33)$$

Notice that the chemical potential, μ disappears.

Now that we have a biased probability function, we can insert that into the MC acceptance criterion,

$$acc(o \rightarrow n) = \min \left[1, \frac{p_{bias}(\mathbf{\Gamma}_n, N_n)}{p_{bias}(\mathbf{\Gamma}_o, N_o)} \right] \quad (2.34)$$

This criterion, also known as the Metropolis acceptance criterion, represents the probability of accepting a move from the current point in phase space, o , to a new point, n . Or more specifically, the probability of accepting a move from an old configuration $\mathbf{\Gamma}_o$ and number of particles N_o to a new state $\mathbf{\Gamma}_n$ and N_n . The move is accepted one hundred percent

of the time if the fractional term is greater than 1, otherwise it accepts the move based on a fractional probability (e.g., if the the fractional term equaled 1/2 than the move would be accepted fifty percent of the time). When we substitute in the biased probability functions for both an old state and new state, we get

$$acc(o \rightarrow n) = \min \left[1, \frac{Q(N_o, V, T) V^{N_n} N_o! \Lambda^{3N_o} \exp(-\beta U(\mathbf{\Gamma}_n))}{Q(N_n, V, T) V^{N_o} N_n! \Lambda^{3N_n} \exp(-\beta U(\mathbf{\Gamma}_o))} \right] \quad (2.35)$$

Now, since μ is not present in the acceptance criteria, it can be seen why it is no longer necessary to know the chemical potential of coexistence or even to specify a value of μ at all. Though every other term present in the acceptance criteria is known *a priori*, the canonical partition function is not known. This is where the WL algorithm comes into play:

1. $Q(N, V, T)$ is first set to 1 for all values of N .
2. As the simulation proceeds, the current estimate of $Q(N, V, T)$ is used.
3. When a specific N is sampled, $Q(N, V, T)$ is updated: $Q(N, V, T) \rightarrow f \times Q(N, V, T)$ where f is initially set to e (i.e., about 2.72).
4. At the same time a histogram that keeps track of the visited values of N , $H(N)$, is kept during the simulation and is set to zero for all values of N .
5. Since $Q(N, V, T)$ is dynamically updated, the simulation is always pushed away from the current value of N to a new one.
6. Thus the histogram, $H(N)$, eventually becomes flat.

7. When this happens, $f \rightarrow f^{A/2}$ and $H(N)$ is set back to zero.
8. The simulation will converge once f is arbitrarily close to unity and the updates of $Q(N, V, T)$ are negligible, thus an estimate of $Q(N, V, T)$ is obtained.
9. Then from our estimated $Q(N, V, T)$, we can get the GC partition function which is given again below for the reader's convenience.

$$\Theta(\mu, V, T) = \sum_{N=0}^{\infty} Q(N, V, T) \exp(\beta\mu N), \quad (2.36)$$

When WL sampling is used as described above in the grand canonical ensemble, accurate estimates for the corresponding densities of the liquid and vapor phases in coexistence have been shown to be in good agreement with results from the more expensive TM method.⁷⁷ However, it was also shown at the same time that it produced inaccurate results for activity and the chemical potential, which had largest deviations at low temperatures where deviations reached up to 10% from the TM results. This is a serious drawback for modeling adsorption into IRMOFs since an inaccurate value of the chemical potential translates into an inaccurate estimate of the partition function and thus the thermodynamic values. However, recently, a method has been developed to overcome this issue and has been shown to produce highly accurate values for both the activity and the chemical potential.⁹² This is accomplished by carrying out WL sampling of a simplified version of the expanded grand canonical ensemble.^{104–112} This method is known as Expanded Wang-Landau^{92,93} and is described below.

2.3 EXPANDED WANG-LANDAU SAMPLING

2.3.1 Formalism

Before we delve into how Wang-Landau sampling is used in the expanded WL method, we must understand how the simplified expanded grand-canonical (SEGC) partition function is obtained. This formalism was obtained recently,⁹² and is given below starting from the grand canonical partition function. The grand canonical partition function is given again below for the readers convenience, for a system of N atoms or molecules, at volume V and temperature T , which is

$$\Theta(\mu, V, T) = \sum_{N=0}^{\infty} Q(N, V, T) \exp(\beta\mu N), \quad (2.37)$$

and, again, $Q(N, V, T)$ is given by

$$Q(N, V, T) = \frac{V^N}{N! \Lambda^{3N}} \int \exp(-\beta U(\mathbf{\Gamma})) d\mathbf{\Gamma} \quad (2.38)$$

Now, our next step is to obtain the expanded grand canonical (EGC) partition function. In order to do this we must consider the insertion and deletion of particles within the system, which, of course, results in a change in N . It is our goal to accurately sample the grand-canonical ensemble; to accomplish this task, we need an efficient scheme to insert and delete particles. This has proven to be problematic, particularly with large molecules like PAHs. To remedy this issue, it was proposed to divide up the insertion and deletion into M different stages, where M is an integer. Thus, during the simulation, the system would be composed of both N molecules and a fractional particle in stage l , where $0 \leq l \leq M - 1$.

This fractional particle then interacts with the full particles via a coupling parameter ξ_l which will be described further in Subsection 2.4.1. During a simulation l is allowed to change, resulting in a change in N . An example of a fractional particle is given in Figure 2.20.



Figure 2.20. Two molecules of CO_2 , the one on the left is a full particle, while the one on the right is a particle of fraction close to $l = 50$.

When working with a system composed of a fractional particle and N full particles, the grand-canonical partition function must be expanded. Now we must sum over all N and l , rather than just over all N . Also we must add a weighting function, denoted $\psi(l, N)$, to the exponent. This weighting function is generally determined through numerical calculations^{107,113,114} in order to optimize the sampling of the system around a specific value of N . This is the value of N around which a simulation converges when conventional GCMC or Gibbs Ensemble Monte Carlo (GEMC)¹¹⁵ are used.

Therefore, the expanded grand canonical partition function^{104,106–112} is given by

$$\Theta_{\text{EGC}}(\mu, V, T) = \sum_{N=0}^{\infty} \sum_{l=0}^{M-1} Q(N, V, T, l) \exp(\beta\mu N + \psi(l, N)) \quad (2.39)$$

where $Q(N, V, T, l)$ is the canonical partition function for a system of N full particles and a fractional particle at stage $l > 0$ and is given by

$$Q(N, V, T, l) = \frac{V^{N+1}}{N! \Lambda^{3N} \Lambda_l^3} \int \exp(-\beta U(\mathbf{\Gamma})) d\mathbf{\Gamma} \quad (2.40)$$

where Λ_l is the thermal de Broglie wavelength for a fractional particle in stage $l > 0$ and $\mathbf{\Gamma}$ represents a specific configuration of the system made up of N full particles and a fractional particle. Notice that when $l = 0$, the canonical partition function is $Q(N, V, T, l = 0)$ and is for a system of N full particles. Thus, we can recover the partition function of the grand-canonical ensemble if we choose $\psi(l = 0, N) = 0$ and consider only the terms in eq 2.39 in which $l = 0$.

Now that we have the EGC partition function, we can simplify it, thus allowing the simulations to converge much faster. To accomplish this, we first impose that $\psi(l, N) = 0$ for all l and N . We can do this because the choice of the weighting function, $\psi(l, N)$, has no affect on the value of the grand-canonical partition function since we are using Wang-Landau sampling which is a uniform sampling method. Secondly, we can choose that the mass of the fractional particle be the same as the whole particle regardless of the value of l , thus setting $\Lambda_l = \Lambda$. Then, using those simplifications, we obtain the partition function of a simplified expanded grand canonical (SEGC) ensemble,

$$\Theta_{\text{SEGC}}(\mu, V, T) = \sum_{N=0}^{\infty} \sum_{l=0}^{M-1} Q(N, V, T, l) \exp(\beta \mu N) \quad (2.41)$$

and the canonical partition function, for $0 < l < M$,

$$Q(N, V, T, l) = \frac{V^{N+1}}{N! \Lambda^{3N}} \int \exp(-\beta U(\mathbf{\Gamma})) d\mathbf{\Gamma} \quad (2.42)$$

Now that we have the SEGC partition function defined, let's delve into the algorithm that WL sampling follows in this ensemble. Since we have a fractional particle of fraction l , there are two possibilities for the joint Boltzmann distribution depending on the value of l ,

$$p(\mathbf{\Gamma}, N, l) = \begin{cases} \frac{V^{N+1} \exp(\beta\mu N - \beta U(\mathbf{\Gamma}))}{N! \Lambda^{3(N+1)} \Theta_{SEGC}(\mu, V, T)} & \text{for } 0 < l < M \\ \frac{V^N \exp(\beta\mu N - \beta U(\mathbf{\Gamma}))}{N! \Lambda^{3N} \Theta_{SEGC}(\mu, V, T)} & \text{for } l = 0 \end{cases} \quad (2.43)$$

Then, the probability distribution, $p(N, l)$, can be obtained by

$$p(N, l) = \int p(\mathbf{\Gamma}, N, l) d\mathbf{\Gamma} = \frac{Q(N, V, T, l) \exp(\beta\mu N)}{\Theta_{SEGC}(\mu, V, T)} \quad (2.44)$$

The biased distribution for $0 < l < M$, obtained by using eq 2.39, is

$$p_{bias}(\mathbf{\Gamma}, N, l) = \frac{p(\mathbf{\Gamma}, N, l)}{p(N, l)} = \frac{\frac{V^{N+1} \exp(\beta\mu N - \beta U(\mathbf{\Gamma}))}{N! \Lambda^{3(N+1)} \Theta_{SEGC}(\mu, V, T)}}{\frac{Q(N, V, T, l) \exp(\beta\mu N)}{\Theta_{SEGC}(\mu, V, T)}} = \frac{V^{N+1} \exp(-\beta U(\mathbf{\Gamma}))}{Q(N, V, T, l) N! \Lambda^{3(N+1)}} \quad (2.45)$$

while the biased distribution for $l = 0$, also obtained by using eq 2.39, is given by

$$p_{bias}(\mathbf{\Gamma}, N, l = 0) = \frac{p(\mathbf{\Gamma}, N, l = 0)}{p(N, l = 0)} = \frac{\frac{V^N \exp(\beta\mu N - \beta U(\mathbf{\Gamma}))}{N! \Lambda^{3N} \Theta_{SEGC}(\mu, V, T)}}{\frac{Q(N, V, T, l = 0) \exp(\beta\mu N)}{\Theta_{SEGC}(\mu, V, T)}} = \frac{V^N \exp(-\beta U(\mathbf{\Gamma}))}{Q(N, V, T, l = 0) N! \Lambda^{3N}} \quad (2.46)$$

Notice again that in both cases the chemical potential is absent from the biased probability function. Now, the MC acceptance criterion from an old state $(\mathbf{\Gamma}_o, N_o$ and fractional

number l_o) to a new state $(\Gamma_n, N_n$ and $l_n)$ is given generally by

$$acc(o \rightarrow n) = \min \left[1, \frac{p_{bias}(\Gamma_n, N_n, l_n)}{p_{bias}(\Gamma_o, N_o, l_o)} \right] \quad (2.47)$$

To be more specific, there are four different MC acceptance criterion, depending on the value of l and whether the adsorbates are atoms or molecules. The first case is when both l_o and l_n are equal to or larger than 0, and the acceptance criteria for that case is

$$acc(o \rightarrow n) = \min \left[1, \frac{Q(N_o, V, T, l_o) V^{N_n} N_o! \Lambda^{3N_o} \exp(-\beta U(\Gamma_n))}{Q(N_n, V, T, l_n) V^{N_o} N_n! \Lambda^{3N_n} \exp(-\beta U(\Gamma_o))} \right] \quad (2.48)$$

If $l_o = 0$ and $l_n > 0$, then the acceptance criteria is

$$acc(o \rightarrow n) = \min \left[1, \frac{Q(N_o, V, T, l_o) V^{N_n+1} N_o! \Lambda^{3N_o} \exp(-\beta U(\Gamma_n))}{Q(N_n, V, T, l_n) V^{N_o} N_n! \Lambda^{3(N_n+1)} \exp(-\beta U(\Gamma_o))} \right] \quad (2.49)$$

If $l_o > 0$ and $l_n = 0$, then the acceptance criteria is

$$acc(o \rightarrow n) = \min \left[1, \frac{Q(N_o, V, T, l_o) V^{N_n} N_o! \Lambda^{3(N_o+1)} \exp(-\beta U(\Gamma_n))}{Q(N_n, V, T, l_n) V^{N_o+1} N_n! \Lambda^{3N_n} \exp(-\beta U(\Gamma_o))} \right] \quad (2.50)$$

When this method is applied to molecular fluids by including the molecular partition function for the internal degrees of freedom of rotation and vibration, q_{int} , the acceptance criteria becomes

$$acc(o \rightarrow n) = \min \left[1, \frac{Q(N_o, V, T, l_o) V^{N_n} q_{int}^{N_n} N_o! \Lambda^{3N_o} \exp(-\beta U(\Gamma_n))}{Q(N_n, V, T, l_n) V^{N_o} q_{int}^{N_o} N_n! \Lambda^{3N_n} \exp(-\beta U(\Gamma_o))} \right] \quad (2.51)$$

Again, there is no chemical potential in any of the acceptance criteria, thus μ does not

need to be specified to start the simulation. The algorithm of WL sampling in the SEGC ensemble is identical to when it's in the grand canonical ensemble as explained above, except now $Q(N, V, T, l)$ needs to be estimated. Thus rather than just visiting various values of N , now various fractions, l , also must be sampled. So, two histograms are kept, one to keep track of the visited values of N and one for the visited values of l . Once the simulation has converged, $Q(N, V, T, l)$ is provided up to a multiplicative constant. Then by using the fact that $Q(N = 0, V, T, l = 0) = 1$, we can obtain the actual value of $Q(N, V, T, l)$. Finally, through a Laplace transform, we can obtain the grand canonical partition function

$$\Theta(\mu, V, T) = \sum_{N=0}^{\infty} Q(N, V, T, l = 0) \exp(\beta\mu N) \quad (2.52)$$

2.3.2 Determination of Thermodynamic Properties

Recently, when expanded WL was first presented it was applied to the determination of the thermodynamic properties of liquid-vapor coexistence as well as to the determination of the thermodynamic properties of the bulk phases of atomic (i.e., argon) and molecular (i.e., CO₂) systems.⁹² This was done to establish the accuracy of the method concerning the calculation of the relevant thermodynamic properties. This section will focus on how the thermodynamic properties can be obtained, through the use of the obtained grand-canonical partition function, for both the liquid-vapor coexistence and of the bulk for molecular systems such as CO₂. Though the method given will be for CO₂ due to the nature of this thesis, some figures of argon will be given for pedagogical purposes.

First, the determination of the conditions of coexistence through the use of the obtained grand-canonical partition function will be given. Now, in order to find those conditions, the

phase transition must first be located. This can be accomplished by determining μ_{coex} , the chemical potential at coexistence, for each temperature considered through analyzing the number distribution

$$p(N) = \frac{Q(N, V, T) \exp(\beta \mu N)}{\Theta(\mu V, T)} \quad (2.53)$$

where, depending on the value of μ , the number distribution will exhibit one peak corresponding to the bulk or it will exhibit two peaks corresponding to the system being close to coexistence. In Figure 2.21, examples of the particle number distributions of argon for various values of μ , which correspond to the liquid phase (Figure 2.21a), vapor phase (Figure 2.21b) and coexistence of the phases (Figure 2.21c), are given.

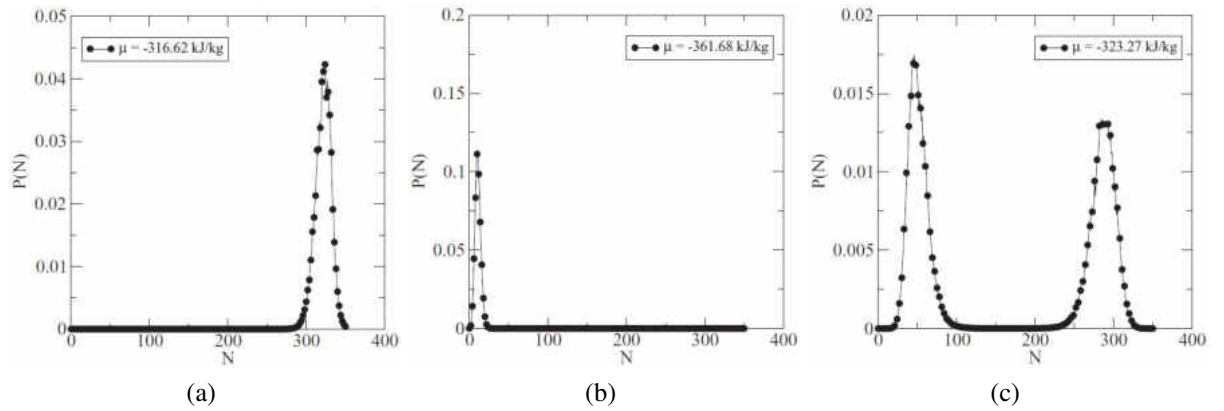


Figure 2.21. The number distribution $p(N)$ of argon at $T = 140.46K$ for different values of μ : (a) $\mu = -316.62$ kJ/kg (bulk liquid), (b) $\mu = -361.68$ kJ/kg (bulk vapor), and (c) $\mu = -323.27$ kJ/kg (liquid-vapor coexistence). Figures taken from reference 92

The chemical potential at coexistence, μ_{coex} , corresponds to the value at which the area under both peaks are equal to each other (Figure 2.21c). This indicates that both phases are equally probable for $\mu = \mu_{coex}$. Once μ_{coex} is determined for each temperature, the

saturation pressure, P_{sat} , was obtained through

$$P = \frac{k_B T \ln \Theta(\mu, V, T)}{V} \quad (2.54)$$

Next, the densities of the two coexisting phases can be obtained by applying

$$\langle \rho_{liq} \rangle = \frac{\sum_{N > N_b} \frac{N}{V} Q(N, V, T) \exp(\beta \mu N)}{\sum_{N > N_b} Q(N, V, T) \exp(\beta \mu N)} \quad (2.55)$$

for the liquid density, where N_b is the number of CO₂ molecules at which $p(N)$ reaches its minimum between the phases, and

$$\langle \rho_{vap} \rangle = \frac{\sum_{N < N_b} \frac{N}{V} Q(N, V, T) \exp(\beta \mu N)}{\sum_{N < N_b} Q(N, V, T) \exp(\beta \mu N)} \quad (2.56)$$

for the vapor density. Next, it will be shown how to use the grand-canonical partition function to evaluate the state functions at coexistence. First, for the entropy at coexistence, we have

$$S_{liq} = \frac{k_B \ln[\Theta(\mu, V, T)]}{\langle N_{liq} \rangle} + \frac{(U_{liq} - \mu)}{k_B T} \quad (2.57)$$

for the liquid phase at coexistence, where,

$$\langle N_{liq} \rangle = \frac{\sum_{N > N_b} N [Q(N, V, T) \exp(\beta \mu N)]}{\sum_{N > N_b} Q(N, V, T) \exp(\beta \mu N)} \quad (2.58)$$

and for the vapor phase at coexistence we have

$$S_{vap} = \frac{k_B \ln[\Theta(\mu, V, T)]}{\langle N_{vap} \rangle} + \frac{(U_{vap} - \mu)}{k_B T} \quad (2.59)$$

where

$$\langle N_{vap} \rangle = \frac{\sum_{N < N_b} N [Q(N, V, T) \exp(\beta \mu N)]}{\sum_{N < N_b} Q(N, V, T) \exp(\beta \mu N)} \quad (2.60)$$

and the internal energy for the liquid at coexistence is given by

$$U_{liq} = \frac{\sum_{N > N_b} (\bar{E}_{pot}(N) + \frac{5}{2} k_B T) p(N)}{\sum_{N > N_b} p(N)} \quad (2.61)$$

where $\bar{E}_{pot}(N)$ is the average potential energy per CO₂ molecule (note that any quantity X noted as \bar{X} denotes a quantity per molecule in this chapter of this thesis), which is collected during the expanded WL simulation, for a system containing N full CO₂ molecules. The term $\frac{5}{2} k_B T$ is the ideal gas kinetic contribution arising from the 3 translational degrees of freedom (DoF) and from the 2 rotational DoF per CO₂ molecule. For the vapor phase at coexistence we have the internal energy given by

$$U_{vap} = \frac{\sum_{N < N_b} (\bar{E}_{pot}(N) + \frac{5}{2} k_B T) p(N)}{\sum_{N < N_b} p(N)} \quad (2.62)$$

After these values are calculated, the Helmholtz free energy can be obtained by

$$A_{liq} = U_{liq} - T S_{liq} \quad (2.63)$$

for the liquid phase, and by

$$A_{vap} = U_{vap} - TS_{vap} \quad (2.64)$$

for the vapor phase.

Now the way in which the bulk phase properties can be determined will be given. The thermodynamic properties for either of the bulk phases can be easily obtained from its corresponding grand-canonical partition function. This can be accomplished by gradually adjusting the chemical potential with $\mu \geq \mu_{coex}$ to determine the properties for the liquid phase from the corresponding partition function, $\Theta^l(\mu^l, V^l, T^l)$ and $\mu \leq \mu_{coex}$ to determine the properties of the vapor phase (i.e., the gas phase) from the corresponding partition function, $\Theta^g(\mu^g, V^g, T^g)$. In each case the molecular number distribution will exhibit a single peak (Figure 2.21a and 2.21b).

Only the equations for the gas phase will be given here for two reasons. Firstly, the equations for the density and the thermodynamic functions are the same except for the superscript l rather than g . Secondly, since when simulating the adsorption phenomena into porous material by means of the expanded WL method, its necessary to run a gas phase bulk simulation of the given atom or molecule as well as calculate the corresponding thermodynamic functions. This has a twofold purpose: (i) they are used to obtain the equilibrium pressure and (ii) they are used to determine the excess thermodynamic properties (which will be explained further in Section 4.2).⁹³

So, when using expanded WL simulations for the gas phase at a given temperature T , the system's canonical partition function is evaluated as $Q^g(N^g, V^g, T, l = 0)$. Then, the grand-canonical partition function of the gas phase, for any value of μ^g , is given as

$$\Theta^g(\mu^g, V^g, T) = \sum_{N^g=0}^{\infty} Q^g(N^g, V^g, T) \exp(\beta \mu^g N^g) \quad (2.65)$$

where μ^g is the chemical potential for the gas phase, V^g is the volume of the gas phase and N^g is the number of molecules in the gas phase. Notice also that $l = 0$ is dropped from $Q^g(N^g, V^g, T)$, which is just the canonical partition function for a system of N^g molecules and a void fractional molecule.

After $\Theta^g(\mu^g, V^g, T)$ is known, all the thermodynamic properties of the system can be obtained for any value of μ^g and the expressions are given below starting with the pressure, P^g ,

$$P^g = \frac{k_B T \ln[\Theta^g(\mu^g, V^g, T)]}{V^g} \quad (2.66)$$

Then the grand potential, Ω^g , can be calculated by

$$\Omega^g = -k_B T \ln[\Theta^g(\mu^g, V^g, T)] = -P^g V^g \quad (2.67)$$

The density of the bulk gas phase can be calculated for any value of μ as

$$\rho^g = \frac{\sum_{N^g} \frac{N^g}{V^g} Q^g(N^g, V^g, T) \exp(\beta \mu^g N^g)}{\sum_{N^g} Q^g(N^g, V^g, T) \exp(\beta \mu^g N^g)} \quad (2.68)$$

Also, the internal energy of the gas phase per molecule, \bar{U}^g can be obtained by

$$\bar{U}^g = \frac{\sum_{N^g} (\bar{E}_{pot}^g(N^g) + \frac{5}{2} k_B T) Q^g(N^g, V^g, T) \exp(\beta \mu^g N^g)}{\sum_{N^g} Q^g(N^g, V^g, T) \exp(\beta \mu^g N^g)} \quad (2.69)$$

where $\bar{E}_{pot}^g(N^g)$ is the average potential energy per molecule collected during the simulation of the gas phase for a system containing N^g molecules. Here, as above in eqs 2.61 and 2.62, the $\frac{5}{2}$ is due to carbon dioxide's DoF. Next, the Gibbs free energy is just given by

$$\bar{G}^g = \mu^g \quad (2.70)$$

The entropy can be calculated as

$$\bar{S}^g = \frac{k_B \ln[\Theta^g(\mu^g, V^g, T)]}{\langle N^g \rangle} + \frac{(\bar{U}^g - \mu^g)}{k_B T} \quad (2.71)$$

where $\langle N^g \rangle$ is given by

$$\langle N^g \rangle = \frac{\sum_{N^g} N^g [Q^g(N^g, V^g, T) \exp(\beta \mu^g N^g)]}{\sum_{N^g} Q^g(N^g, V^g, T) \exp(\beta \mu^g N^g)} \quad (2.72)$$

Also, the Helmholtz free energy is

$$\bar{A}^g = \bar{U}^g - T \bar{S}^g \quad (2.73)$$

and, finally, the enthalpy can be obtained by

$$\bar{H}^g = \bar{U}^g + P^g \bar{V}^g \quad (2.74)$$

2.3.3 Applied to Vapor-Liquid Equilibrium

As mentioned above, expanded WL was applied to both the determination of the thermodynamic properties of liquid-vapor coexistence and to the determination of the ther-

modynamic properties of the bulk phases of atomic (i.e., argon) and molecular (i.e., CO₂) systems.⁹² In this section the results of the CO₂ simulations will be presented. First, however, the potentials used and the simulation details used are given below.

When using expanded WL simulations, a potential must be used for both the full particles as well as the fractional particles. In our simulations, the force field that was used for CO₂ was the TraPPE potential.¹¹⁶ This consists of three Lenard-Jones (LJ) sites and three point charges per molecule. The interactions between two atoms i and j belonging to two different full CO₂ molecules is

$$\phi(r_{ij}) = 4\epsilon_{ij} \left[\left(\frac{\sigma_{ij}}{r_{ij}} \right)^{12} - \left(\frac{\sigma_{ij}}{r_{ij}} \right)^6 \right] + \frac{q_i q_j}{4\pi\epsilon_0 r_{ij}} \quad (2.75)$$

where r_{ij} is the distance between atom i and atom j . The parameters for the model, ϵ_{ij} (i.e., the depth for the potential energy well), σ_{ij} (i.e., the exclusion diameter) and q_i (i.e., the charge of atom i) were taken from the literature.¹¹⁶ For unlike atoms, the Lorentz-Berthelot mixing rules¹¹⁷ were used.

The interaction of one atom from a full molecule with an atom from a fractional molecule is

$$\phi(r_{ij}) = 4\epsilon_{ij,\xi_l} \left[\left(\frac{\sigma_{ij,\xi_l}}{r_{ij}} \right)^{12} - \left(\frac{\sigma_{ij,\xi_l}}{r_{ij}} \right)^6 \right] + \frac{q_{i,\xi_l} q_j}{4\pi\epsilon_0 r_{ij}} \quad (2.76)$$

where ξ_l denotes the coupling parameter between the full and the fractional particle, $\epsilon_{ij,\xi_l} = (l/M)^{1/3} \epsilon_{ij}$, $\sigma_{ij,\xi_l} = (l/M)^{1/4} \sigma_{ij}$ and $q_{i,\xi_l} = (l/M)^{1/3} q_i$, where $M = 100$. Additionally to the partial coupling for the nonbonded interactions, a homothetic transformation to the skeleton of the fractional CO₂ molecule was applied as the fractional molecule grew and shrank. Thus at

a given stage l , the distance between a carbon and an oxygen atom in the fractional CO_2 molecule is given by $(l/M)^{1/4}d_{C-O}^{eq}$, where $d_{C-O}^{eq} = 1.16\text{\AA}$ is the distance between a carbon and an oxygen in a full CO_2 molecule. Most of the results obtained were obtained with a boxlength of $L = 31.05\text{\AA}$ with a pair interactions cutoff set to half the boxlength.⁹²

Now, for the results,⁹² starting with the reduced canonical partition function, $Q^*(N, V, T)$, which is presented as a function of the number of CO_2 molecules for temperatures ranging from 220 K to 280 K in Figure 2.22. Here, the canonical partition function is reduced with respect to the partition function of an ideal gas which is composed of rigid, linear molecules.

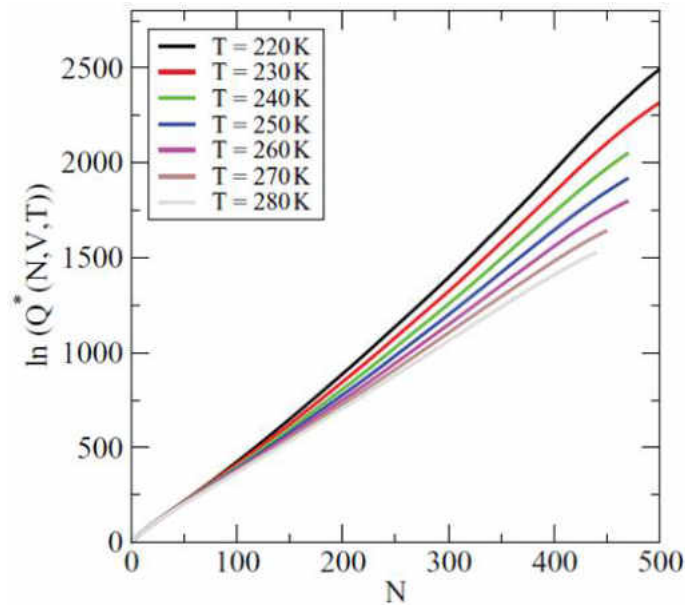


Figure 2.22. The logarithm of the reduced canonical partition function for carbon dioxide plotted against the number of CO_2 molecules, where $Q^*(N, V, T) = \frac{\Lambda^{3N} Q(N, V, T)}{\left(\frac{8\pi^2 I k_B T}{2h^2}\right)^N}$. Figure taken from reference 92

Thus, the grand-canonical partition functions were evaluated through the use of eq 2.52. Then the saturation pressure, as obtained through eq 2.54, was obtained as is presented as

a function of temperature in Figure 2.23a. Also after the densities for the two coexisting phases were found by applying eqs 2.55 and 2.56, the phase diagram of CO₂ in the volume-temperature plane was obtained and is presented in Figure 2.23b. The results in both diagrams as well as the critical points are in excellent agreement with experimental data⁹¹ as well as prior simulation work.¹¹⁶

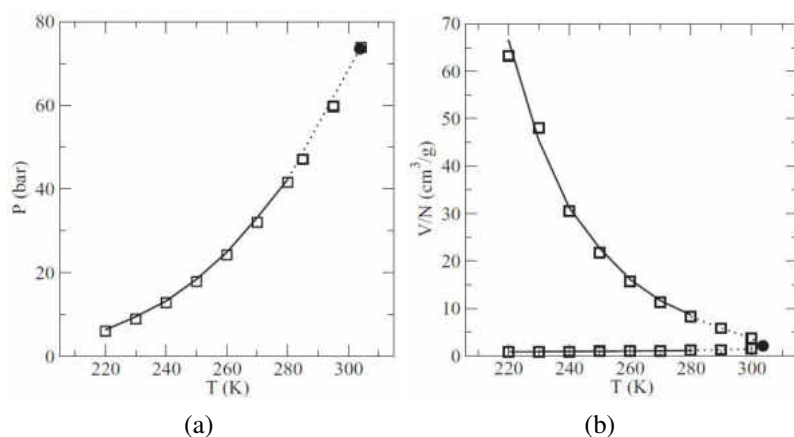


Figure 2.23. Vapor-liquid phase diagrams for CO₂ in the (a) pressure-temperature plane and in the (b) volume-pressure plane. Results from expanded WL are connected by a solid line, where the experimental data are shown with empty squares.⁹¹ The estimated critical point is given as a filled circle. Figures taken from reference 92

Through the use of eqs 2.57 and 2.59, the entropies of the two coexisting phases were obtained and the results are presented in Table 2.2 and compared to experimental data.⁹¹ As can be seen, the results are in excellent agreement with the experimental data for both the liquid (with deviations around only 3%) and for the vapor (with deviations around only 1%) for the whole range of temperatures. This is due to the increased accuracy of expanded WL over GCMC with WL sampling concerning the results for the chemical potential. This is especially true at low temperatures, as explained earlier, where WL sampling was used with GCMC and the chemical potential deviated over 10% from the more accurate and expensive method of TMMC.⁷⁷ This increased accuracy of expanded WL simulations is due to the highly accurate estimate of the systems partition function.

Table 2.2. Entropies at coexistence for CO₂ from expanded WL simulations (S_{sim}) compared to experimental data (S_{exp}).⁹¹

Temperature (K)	$S_{sim,liq}$ (kJ/kg/K)	$S_{exp,liq}$ (kJ/kg/K)	$S_{sim,vap}$ (kJ/kg/K)	$S_{exp,vap}$ (kJ/kg/K)	ΔS_{sim} (kJ/kg/K)	ΔS_{exp} (kJ/kg/K)
280.00	3.12	3.18	3.90	3.93	0.78	0.75
270.00	3.04	3.10	3.95	4.00	0.91	0.90
260.00	2.95	3.02	4.01	4.06	1.06	1.04
250.00	2.89	2.94	4.07	4.11	1.18	1.18
240.00	2.82	2.86	4.12	4.17	1.30	1.31
230.00	2.74	2.78	4.18	4.21	1.40	1.43
220.00	2.64	2.70	4.24	4.26	1.60	1.56

Now the results for the bulk phase simulations will be given. As an example of the gas phase results, the variations of the density with pressure is given in Figure 2.24a and the variations of entropy with pressure is given in Figure 2.24b. As with the results obtained at coexistence, the bulk gas phase properties are in very good agreement with experimental data.⁹¹

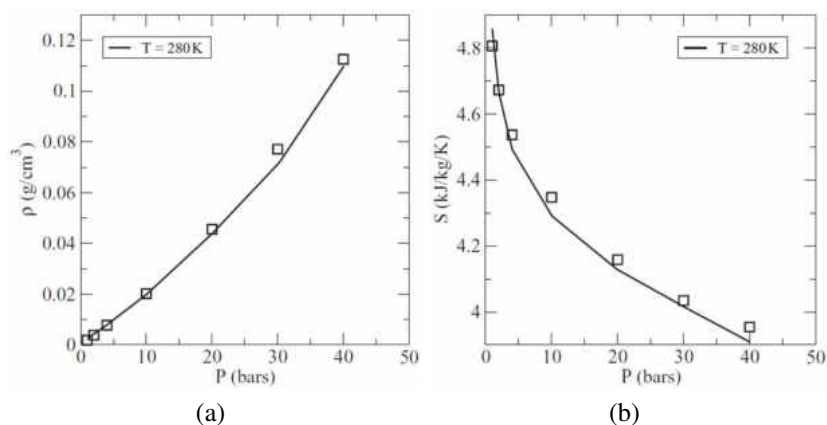


Figure 2.24. Single-phase bulk properties for carbon dioxide: Variations of (a) density and (b) entropy as a function of pressure for the gas phase. The simulation results obtained are shown with lines, while the experimental data are shown as empty squares.⁹¹ Figure taken from reference 92.

Once the expanded WL simulation method was shown to obtain a high-accuracy estimate for the grand-canonical partition function of atomic and molecular systems, and thus the corresponding thermodynamic properties, this method was applied to atomic and molecular adsorption into IRMOF-1.⁹³ It was shown that expanded WL simulations produced a high-accuracy estimate for the grand-canonical partition function of atomic and molecular fluids adsorbed in a porous material while also, through the prediction of absolute and excess thermodynamic properties, providing the user with an excellent way to compare and characterize the performance of various porous materials.⁹³ This is what led to my work described in detail in Section 2.4.

2.4 APPLICATIONS TO CO₂ ADSORPTION INTO IR-MOFS

When studying adsorption phenomena, the approach of understanding the system with 2-D surface thermodynamics has been most often used.¹¹⁹⁻¹²² This approach has proven to be highly useful when dealing with relatively large and simple pores. However, recent advancements in the development of porous materials, such as MOFs, which possess complex pore geometries can no longer be accurately described with the 2-D model. This influx of promising materials has inspired the development of new ways to thermodynamically characterize and assess the performance of these complex porous materials.

About a decade ago, Myers and co-workers⁹⁵⁻⁹⁷ proposed to study adsorption using a solution thermodynamics approach rather than the typical 2-D surface thermodynamics. Solution thermodynamics approaches adsorption in a similar way that a binary mixture is considered. More specifically, the adsorbate is considered the solute while the solid adsorbent takes the part of the solvent. Through this treatment of the adsorption process many useful thermodynamic quantities can be obtained, with the two most important being the immersion and desorption thermodynamic functions. These functions are essential in the characterization of the adsorbent. In particular, as discussed by Myers et al.,⁹⁶ the desorption free energy, enthalpy, and entropy provide a complete thermodynamic description of the system. The desorption free energy rises in importance above the rest being that it is a measure of the performance of the adsorbent, since it can be interpreted as the minimum isothermal work required to regenerate the porous material. From a practical standpoint, this is crucial, since a large sum of the operating cost of the adsorption of post combustion

CO₂ capture is associated with degassing the adsorbent in preparation for the next cycle.

Each of the above mentioned thermodynamic functions can be directly obtained from expanded WL simulations in which a highly accurate estimate of the grand canonical partition function of the adsorbed fluid is obtained. This is particularly advantageous, since once the partition function has been evaluated, all thermodynamic properties, including the desorption free energy and entropy, can be directly evaluated through the formalism of statistical mechanics. Expanded WL was recently shown, as described above in Section 2.3, to produce excellent results when simulating the bulk⁹² as well as for predicting adsorption isotherms of argon and CO₂ in IRMOF-1.⁹³ The work presented below built off of those studies by applying expanded WL simulations to predict the immersion and desorption thermodynamic functions, which provided a complete thermodynamic characterization of the adsorption of CO₂ in a series of isorecticular^{27,32} metal-organic frameworks^{28,123–132} that were studied (i.e., IRMOF-1, IRMOF-8, and IRMOF-10). From this, the relative performance of the three IRMOFs were assessed for CO₂ encapsulation.⁹⁴

2.4.1 Simulation Details and Models used for CO₂ and the IRMOFs

In this work CO₂ adsorption was studied in IRMOF-1, IRMOF-8, and IRMOF-10 for temperatures ranging from 220 K to 360 K. At each temperature, four expanded WL simulations were run. One simulation for each of the IRMOFs and a fourth simulation of the bulk gas phase of CO₂ were used to determine the excess thermodynamic properties measured in experiments.⁹⁵ Since experiments are carried out in the presence of the gas phase, the measurements taken yield only the excess thermodynamic properties, while in simulation one has direct access to the absolute properties. In general, the corresponding

excess property M^e can be calculated from the corresponding absolute property M by

$$M^e = M - V^{void} \bar{M}^g \rho^g \quad (2.77)$$

where V^{void} is the void volume of the porous material⁹⁵ and \bar{M}^g and ρ^g are the molar property M and the molar density (as described above in eq 2.68), respectively, of the gas phase in equilibrium with the adsorbed fluid in the porous material. The simulation of the bulk gas phase allows direct determination of both \bar{M}^g and ρ^g through the grand-canonical partition function for the gas phase $\Theta^g(\mu^g, V^g, T)$ as shown above in Subsection 2.3.2.

During an expanded WL simulation, the Monte Carlo (MC) steps consist of either the translation of a single molecule of CO₂ (37.5% of the MC steps) or the rotation of a single molecule (37.5% of the MC steps) or a change in (N, l) (25% of the MC steps). As shown above, the grand canonical partition function is obtained by setting the canonical partition function, $Q(N, V, T, l)$, equal to unity followed by iteratively improving it through the Wang-Landau algorithm given above. In this work, the criterion for flatness of the histogram $H(N, l)$ required that each (N, l) be visited a minimum of 1000 times and the minimum threshold value for $\ln[f]$ was set to 10^{-8} . This means that the iterative process was repeated 27 times which led to a highly accurate numerical estimate for $Q(N, V, T, l)$. The computational cost of the determination of the adsorption properties through expanded WL simulations was approximately 5×10^9 MC steps for each system. This is comparable to the GCMC simulations of CO₂ adsorption into IRMOF-1¹³³ where the entire adsorption isotherm was produced from ca. 25 runs of 4.0×10^7 MC steps each, amounting to a total of ca. 1.0×10^9 MC steps.

The statistical efficiency of the flat histogram method, TMMC,⁷⁰ to that of GCMC simulations for the determination of adsorption isotherms by molecular simulation was previously compared by Chen and Sholl.¹³⁴ They found that both methods produced results in excellent agreement at low pressures. However, at high pressures, they found that the flat histogram method was more accurate due to the increased scattering GCMC data exhibited. The method used in this work, expanded WL simulations, combines the the advantage of high accuracy of the flat histogram method, TMMC, with the lower computational cost of GCMC though an efficient method for the insertion of molecules, i.e., the gradual insertion of additional molecules through the expanded ensemble scheme. The error bars for each of the thermodynamic properties determined by expanded WL simulations were obtained by carrying out independent simulation runs and given in previous work.^{92,93} It was found that in terms of the adsorption isotherms, the statistical uncertainty of the amount adsorbed was 0.3%.

In these simulations, the force fields that were used for both the full and fractional CO₂ molecules were the same as presented above in Subsection 2.3.3. IRMOF-1, IRMOF-8 and IRMOF-10 were treated as rigid structures. The atomic coordinates and the lattice constants were taken from reference 27. To model the van der Waals interactions of the adsorbed CO₂ molecules and the IRMOFs, the DREIDING force field¹¹⁸ was used, while the parameters for the Lennard-Jones interactions between different kinds of atoms were obtained through the use of the Lorentz-Berthelot mixing rules. This approach has seen extensive use in the modeling of adsorption into MOFs,^{43,47,50,93,138} and was shown to produce results in excellent agreement with the available experimental data. A ball-stick and a space-fill model of IRMOF-1 is given in Figure 2.25 and several snapshots of

IRMOF-1 with various amounts of CO₂ adsorbed into its pores is given in Figure 2.26.

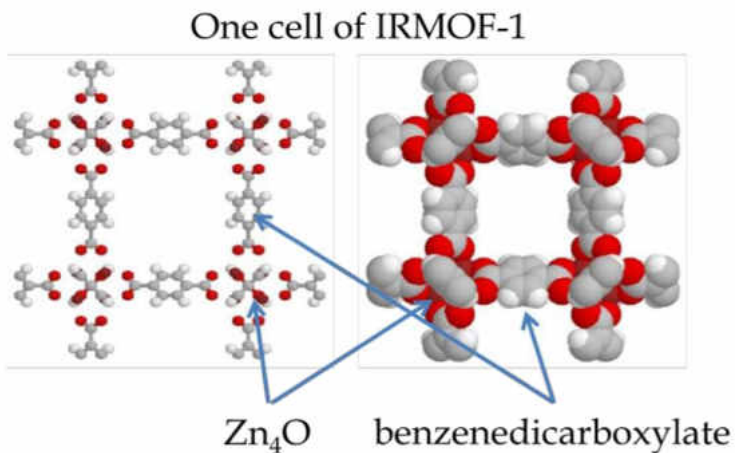


Figure 2.25. Ball-stick and space-fill models of IRMOF-1, showing the inorganic and organic subunits.

2.4.2 Solution Thermodynamics Approach

The thermodynamic analysis of CO₂ adsorption into IRMOFs, as stated above, relies on treating the adsorption process with a solution thermodynamics approach^{95–97,135,136} rather than the conventional concepts of 2-D surface thermodynamics as explained earlier in the beginning of Section 2.4.

This subsection will delve into the details on how the immersion and desorption thermodynamic functions can be determined through expanded WL simulations. As described earlier, the output generated by expanded WL simulations of CO₂ adsorbed in IRMOFs is a highly accurate estimate for the grand-canonical partition function of the system, $\Theta(\mu, V, T)$, which provides direct access to the grand potential through the following relation¹³⁷

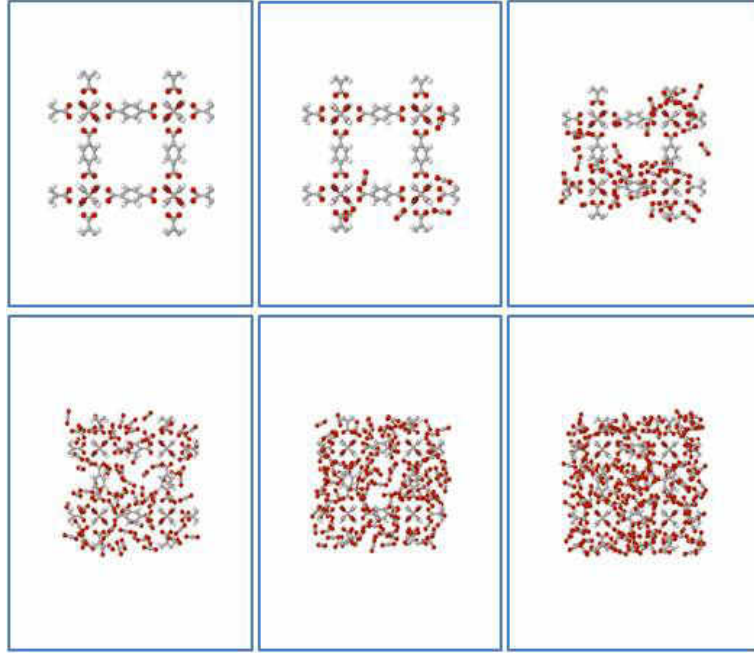


Figure 2.26. Six snapshots of CO₂ adsorption into a single cell of IRMOF-1, for which all the volumes and temperatures are the same.

$$\Omega = -k_B T \ln [\Theta(\mu, V, T)] = -k_B T \ln \left[\sum_{N=0}^{\infty} Q(N, V, T) \exp(\beta \mu N) \right] \quad (2.78)$$

In this equation and in the rest of this thesis the $l = 0$ is not included and $Q(N, V, T)$ is the canonical partition function for a system with N full molecules and a void fractional molecule.

Once the grand canonical partition function is estimated, the molecule number distribution $p(N)$ for the adsorbate can be determined by

$$p(N) = \frac{Q(N, V, T) \exp(\beta \mu N)}{\Theta(\mu, V, T)} \quad (2.79)$$

and the absolute amount adsorbed follows as

$$N_{ads} = \sum_{N=0}^{\infty} Np(N) \quad (2.80)$$

Then the excess adsorption N^e can be calculated by substituting the value for N_{ads} into

$$N^e = N_{ads} - V^{void} \rho^g \quad (2.81)$$

where, again, V^{void} is the void volume of the porous material⁹⁵ and ρ^g is the molar density of the gas phase in equilibrium with the adsorbed fluid in the IRMOF as described above in eq 2.68. Then from eqs 2.79 and 2.80, the absolute internal energy can be calculated through

$$U = N_{ads} \frac{\sum_N (\bar{E}_{pot} + \frac{5}{2}k_B T) p(N)}{\sum_N p(N)} \quad (2.82)$$

where $\bar{E}_{pot}(N)$ is the average potential energy per adsorbed molecule, collected during the expanded WL simulation, for a system containing N molecules and $\frac{5}{2}k_B T$ is the kinetic (ideal gas) contribution for a rigid linear molecule. The absolute Helmholtz free energy can be calculated from the obtained grand canonical partition function and N_{ads} by

$$A = -k_B T \ln[\Theta(\mu, V, T)] + \mu N_{ads} \quad (2.83)$$

Then, the absolute Gibbs free energy is

$$G = A + P^g V \quad (2.84)$$

where V is the volume of the IRMOF and P^g is the external pressure in the gas-phase which was calculated during the expanded WL simulations of the gas phase at μ and T . Similarly, the absolute enthalpy is given by

$$H = U + P^g V \quad (2.85)$$

Additionally, from eqs 2.82 and 2.83 the absolute entropy can be determined through the relation

$$S = \frac{U - A}{T} \quad (2.86)$$

Once the absolute thermodynamic functions are evaluated, the excess thermodynamic properties can then be easily calculated using the properties of the external gas phase following the format of eq 2.77. The excess Gibbs free energy is

$$G^e = G - V^{void} \bar{G}^g \rho^g \quad (2.87)$$

the excess enthalpy is

$$H^e = H - V^{void} \bar{H}^g \rho^g \quad (2.88)$$

and the excess entropy is

$$S^e = S - V^{void} \bar{S}^g \rho^g \quad (2.89)$$

After the excess properties have been calculated, the excess properties relative to an ideal gas reference state can be calculated through the following expressions. The change in the excess Gibbs free energy, excess enthalpy and excess entropy from their respective values in the reference state to their calculated excess values are

$$\Delta G^e = G^e - N^e \mu_o \quad (2.90)$$

$$\Delta H^e = H^e - N^e \bar{H}_o \quad (2.91)$$

$$\Delta S^e = S^e - N^e \bar{S}_o \quad (2.92)$$

where μ_o , $\bar{H}_o = \frac{7}{2}RT$ and \bar{S}_o are the chemical potential, the molar enthalpy, and the molar entropy of an ideal gas composed of linear rigid molecules.

Now, there are two steps for the adsorption process when the system is treated with solution thermodynamics,⁹⁵ where the first step is the isothermal compression of the gas from its ideal gas reference state to the equilibrium pressure P and the second step is the isothermal-isobaric immersion of the clean IRMOF in the compressed gas. To accomplish the first step, a compression function must be defined for each corresponding thermodynamic quantities. These compression functions are associated with the isothermal compression of the gas from the ideal gas reference state, defined above, to the actual pressure of the system, P , and are given below

$$\Delta G^{comp} = N^e (\mu - \mu_o) \quad (2.93)$$

$$\Delta H^{comp} = N^e (\bar{H}^g - \bar{H}_o) \quad (2.94)$$

$$\Delta S^{comp} = N^e (\bar{S}^g - \bar{S}_o) \quad (2.95)$$

In the second step, the clean IRMOF is immersed in the compressed gas through an isothermal-isobaric process. The first step (i.e., compression) depends only on the properties of the bulk gas phase while the second step (i.e., immersion) yields thermodynamic properties that are a function of the physical properties of the adsorbent. Thus, it is these immersion functions that allow for thermodynamic characterization of porous materials. The immersion functions are given below

$$\Delta G^{imm} = \Delta G^e - \Delta G^{comp} = \Delta G^e - N^e(\mu^g - \mu_o) \quad (2.96)$$

$$\Delta H^{imm} = \Delta H^e - \Delta H^{comp} = \Delta H^e - N^e(\bar{H}^g - \bar{H}_o) \quad (2.97)$$

$$\Delta S^{imm} = \Delta S^e - \Delta S^{comp} = \Delta S^e - N^e(\bar{S}^g - \bar{S}_o) \quad (2.98)$$

Then, the desorption free energy, which is the minimum isothermal work required to regenerate the IRMOF, is

$$|\Omega^e| = -\Delta G^{imm} \quad (2.99)$$

This is a particularly useful thermodynamic quantity, since, as noted above, most of the operating cost of adsorptive separations is associated with degassing the adsorbent in preparation of the next cycle. Thus this desorption Gibbs free energy is crucial in the comparison of the performance of different adsorbents.

2.4.3 Performance of IRMOF-1, 8 and 10 in Supercritical and Subcritical Regimes

This section will focus on the results obtained from applying expanded WL to the adsorption of CO₂ into IRMOF-1, IRMOF-8 and IRMOF-10 at eight different temperatures⁹⁴ (five of which are in CO₂'s subcritical regime and three of which are in CO₂'s supercritical regime, where for CO₂, $T_c = 304$ K^{91,92}).

The first results obtained were the main output of expanded WL simulations, the canonical partition functions $Q(N, V, T)$. In Figure 2.27, the converged estimates of the reduced canonical partition functions are plotted as a function of the N CO₂ molecules adsorbed in each of the IRMOFs for all temperatures studied. Here the canonical partition function is reduced with respect to the partition function of an ideal gas which is composed of rigid, linear molecules. It was found that, for a given IRMOF and a given N , the canonical partition function was strongly dependent on the temperature. $Q(N, V, T)$ sharply decreases with temperature when N becomes large (i.e., an almost saturated IRMOF), with $\ln[Q(N, V, T = 360 \text{ K})]$ being roughly a third of its value at $T = 220$ K. It can also be

seen that the features of the canonical partition function, plotted as a function of N , are qualitatively similar for all three IRMOFs.

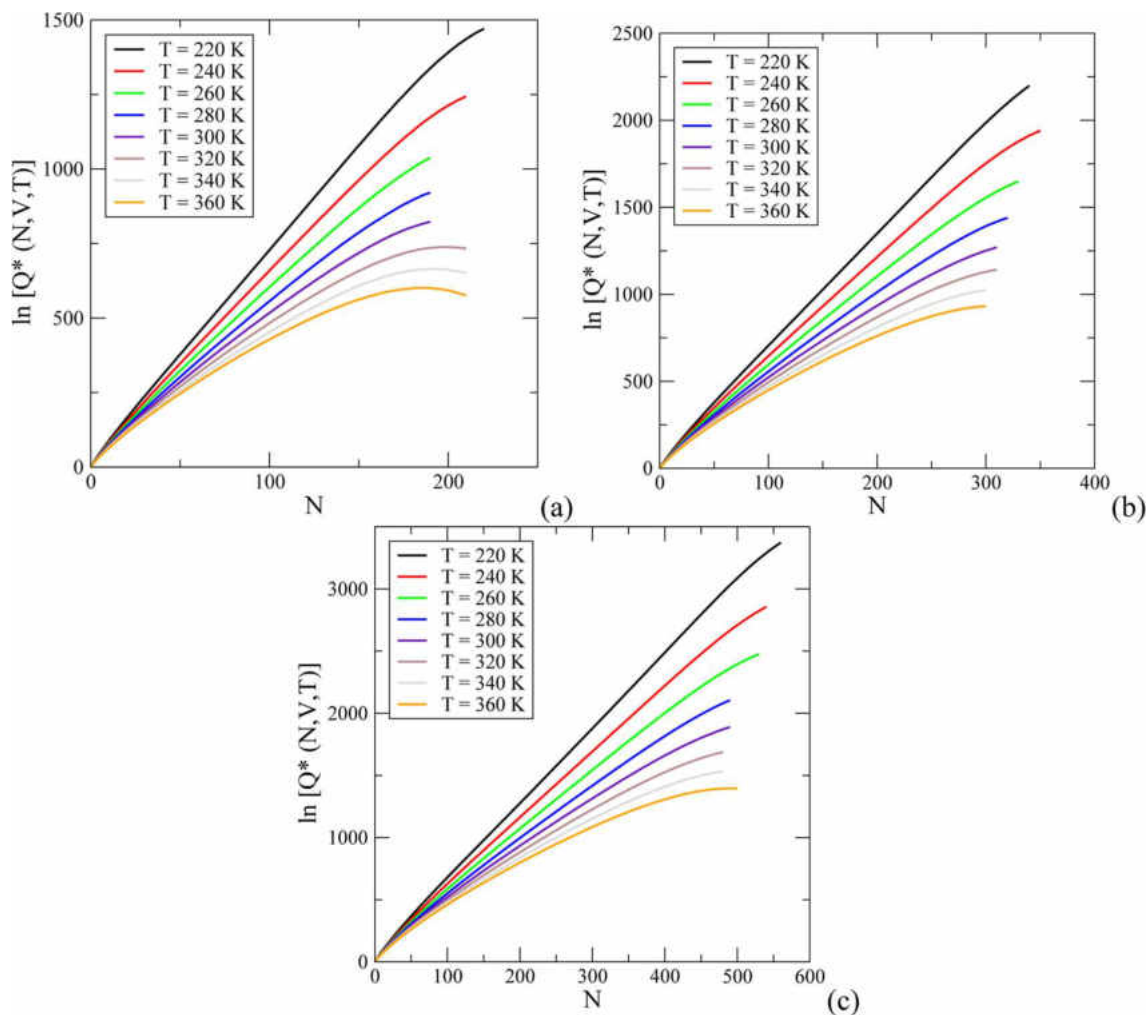


Figure 2.27. The natural logarithm of the reduced canonical partition function $Q^*(N, V, T)$ plotted against the number of atoms adsorbed per unit cell at eight different temperatures for: (a) IRMOF-1, (b) IRMOF-8, and (c) IRMOF-10. The reduced canonical partition function is reduced with respect to the partition function of an ideal gas which is composed of rigid, linear molecules.⁹⁴

As described above, once the canonical partition function is estimated, the grand-canonical partition function, $\Theta(\mu, V, T)$, can be obtained through eq 2.52 and the grand potential, Ω , through eq 2.78. Then through the use of eq 2.80, the absolute adsorption isotherms were obtained and are presented in Figure 2.28 for all three IRMOFs studied in this work. In Figure 2.28a the results obtained from expanded WL simulations at 220 K for IRMOF-1 are compared with the results obtained from prior GCMC simulations at 225 K⁵⁹ and they are found to be in excellent qualitative agreement. There are a few observations related to the pore size in each of the IRMOFs that can be made, where the size of the pores, in ascending order, are IRMOF-1 < IRMOF-8 < IRMOF-10. One such observation is that the steps in the isotherms for the IRMOFs are shifted to higher pressures as the pore size increases, which is due to the decreased degree of confinement in the IRMOFs with a larger pore size. It should also be noted that the maximum loading increases as the size of the pores increase.

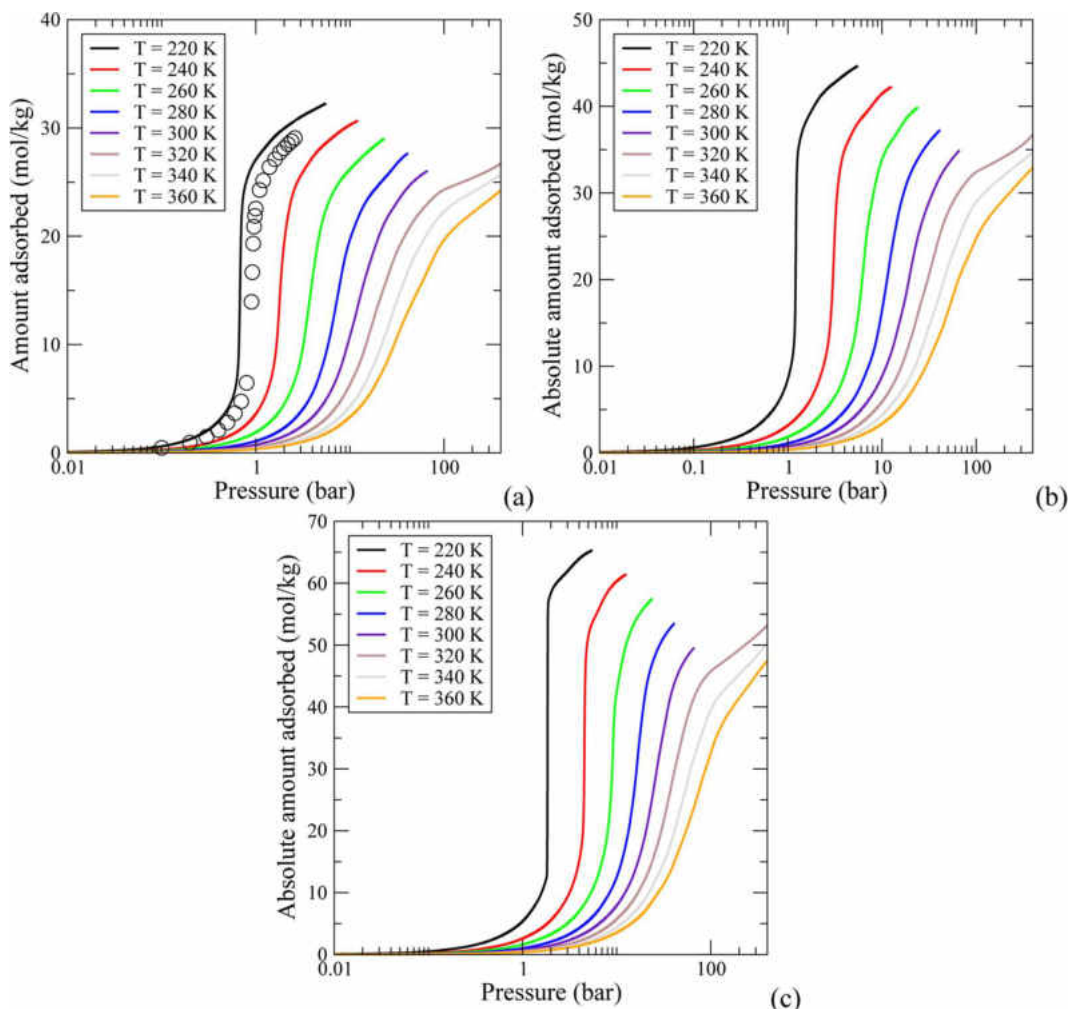


Figure 2.28. Adsorption isotherms of eight temperatures for: (a) IRMOF-1, (b) IRMOF-8, and (c) IRMOF-10.⁹⁴ The results from a set of GCMC simulations⁵⁹ at 225 K for IRMOF-1 is included for comparison (black circles).

The excess adsorption isotherms were also determined. In Figure 2.29 a comparison between the absolute and excess number of molecules adsorbed in IRMOF-8 is presented for both the subcritical ($T = 220$ K) and the supercritical ($T = 360$ K) regimes. In the subcritical regime (Figure 2.29a), both the absolute amount adsorbed and the excess amount adsorbed behave similarly. This is because, at low temperatures, the density of the gas-phase ρ^g is very low, implying that the second term in the equation defining N^e is negligible

(see eq 2.81). However, in the supercritical regime (Figure 2.29b) the absolute and excess adsorption isotherms behave significantly different. A maximum for a pressure of 98 bars is present in the excess adsorption isotherm, while the absolute adsorption isotherm increases monotonically with pressure. This maximum in the excess adsorption isotherm comes from the variations of the second term in the equation defining N^e with pressure (again, see eq 2.81). Since this term is negligible at low pressures the excess adsorption isotherm closely follows the absolute adsorption isotherm. However, as the pressure increases, the density of the bulk steadily increases since $T = 360$ K is well above the critical point of the CO_2 fluid ($T_c = 304$ K^{91,92}) and, though the amount adsorbed in the IRMOF also increases with pressure, it increases more slowly since the IRMOF starts to become saturated. Thus, this leads to the maximum and to the eventual decrease observed for the excess adsorption isotherm. So, it can be deduced from these sets of results that there is significantly different behavior for excess amount adsorbed during subcritical (Figure 2.29a) and supercritical (Figure 2.29b) adsorption.

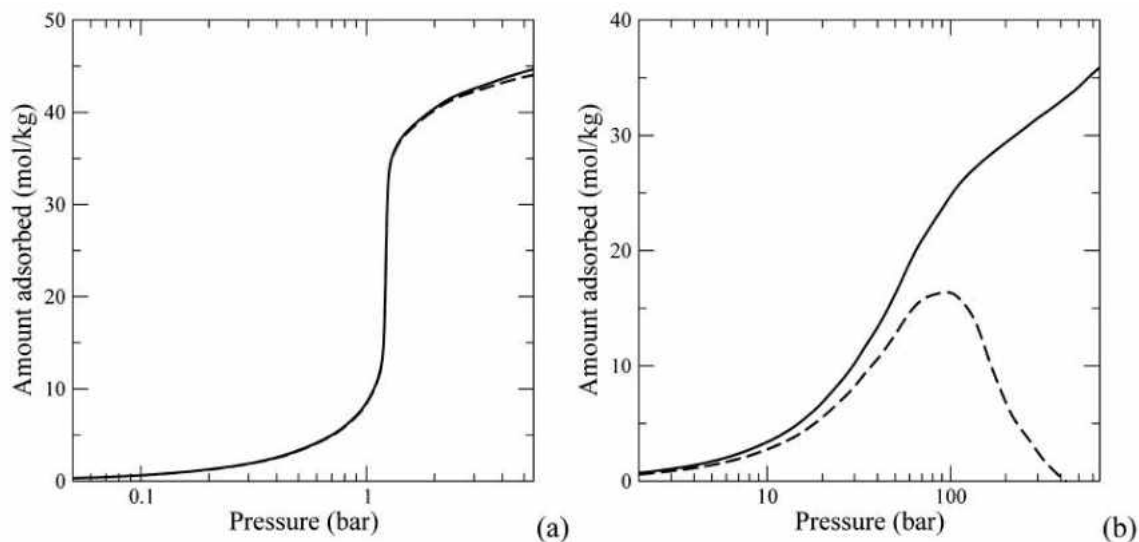


Figure 2.29. Absolute amount (solid line) and excess amount (dashed line) adsorbed per unit cell of IRMOF-8 (in mol/kg) against pressure at: (a) 220 K (subcritical temperature) and (b) 360 K (supercritical temperature).⁹⁴

The rest of the results presented will be the various thermodynamic functions relevant to the adsorption process, the first of which is the Gibbs free energy. In Figure 2.30, the excess Gibbs free energy (ΔG^e), the compression Gibbs free energy (ΔG^{comp}) and the immersion Gibbs free energy (ΔG^{imm}) functions are given for each IRMOF in both the subcritical ($T = 220$ K) and supercritical ($T = 360$ K) regimes. It is worth noting that the reason all of the immersion properties are negative is that adsorption is a spontaneous, exothermic process.

First the results obtained for $T = 220$ K (the left panel of Figure 2.30) will be discussed. It can be observed that ΔG^e drops off sharply for all three IRMOFs. Those drop offs all coincide with the steps observed in the corresponding isotherms and they are also shifted toward higher pressure as the pore size increases from IRMOF-1 to IRMOF-8 and to IRMOF-10. The value reached by ΔG^e at saturation pressure increases from IRMOF-1

to IRMOF-10 as a result of the greater excess amount adsorbed for the larger pore size possessed by each IRMOF. For every IRMOF studied, the predominant contributor to the value of ΔG^e was the compression Gibbs free energy, ΔG^{comp} (e.g., at $P = 5$ bars, the immersion Gibbs free energy, ΔG^{imm} , only represents 10%, 8%, and 6% of ΔG^e for IRMOF-1, IRMOF-8, and IRMOF-10, respectively).⁹⁴

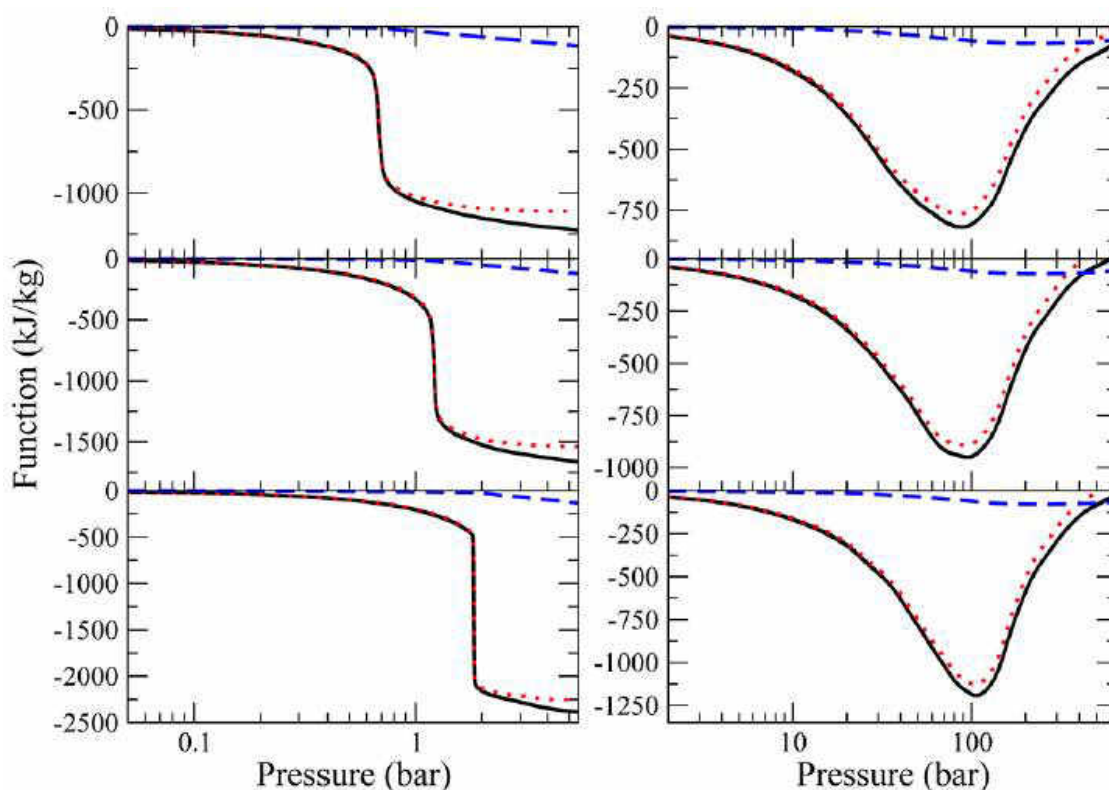


Figure 2.30. ΔG^e (solid line), ΔG^{comp} (dotted line), and ΔG^{imm} (dashed line) against pressure at 220 K (left panel) and at 360 K (right panel). On both panels, results are shown for IRMOF-1 (top), IRMOF-8 (middle), and IRMOF-10 (bottom).⁹⁴

Now, the results obtained for $T = 360$ K (the right panel of Figure 2.30) will be discussed. It can be observed that the ΔG^e function obtained in the supercritical regime exhibits a significantly different behavior than the ΔG^e function obtained in the subcritical regime and reaches a minimum for a pressure of about 90 bars for IRMOF-1, 98 bars for IRMOF-8

and 107 bars for IRMOF-10. It can also be observed that the minima grow deeper as the pore size increases. This reflects the fact that the excess amount adsorbed is greater for the larger IRMOFs. Again for every IRMOF studied, the contribution from the compression Gibbs free energy, ΔG^{comp} , to the value of ΔG^e greatly exceeded the contribution from the immersion Gibbs free energy, ΔG^{imm} .⁹⁴

The next thermodynamic property discussed will be the enthalpy. In Figure 2.31, the excess enthalpy function (ΔH^e), the compression enthalpy function (ΔH^{comp}) and the immersion enthalpy function (ΔH^{imm}) are given. In a similar way to ΔG^e , the trends of ΔH^e can be understood by inspecting the excess amount adsorbed for both the subcritical and supercritical regimes. In the case of ΔH^e , however, it is the immersion enthalpy, ΔH^{imm} , which gives the greatest contribution to ΔH^e rather than the compression enthalpy, ΔH^{comp} , which strongly contrasts the case of the ΔG^e function. This is especially noticeable in the subcritical regime (the left panel of Figure 2.31). It is important to note that ΔH^{comp} is proportional to the enthalpy difference between the bulk gas phase and an ideal gas composed of linear molecules (see eq 2.94). At pressures of the order of 1 bar and below, this difference is very small, which leads to the small contribution of ΔH^{comp} to ΔH^e . At higher pressures, this enthalpy difference increases, which leads to a greater contribution to ΔH^e from ΔH^{comp} at much higher pressures. This is easiest to see in the results obtained at 360 K, for all IRMOFs, the contribution from ΔH^{comp} climbs to about 20% of ΔH^e close to the minima in the ΔH^e functions).⁹⁴

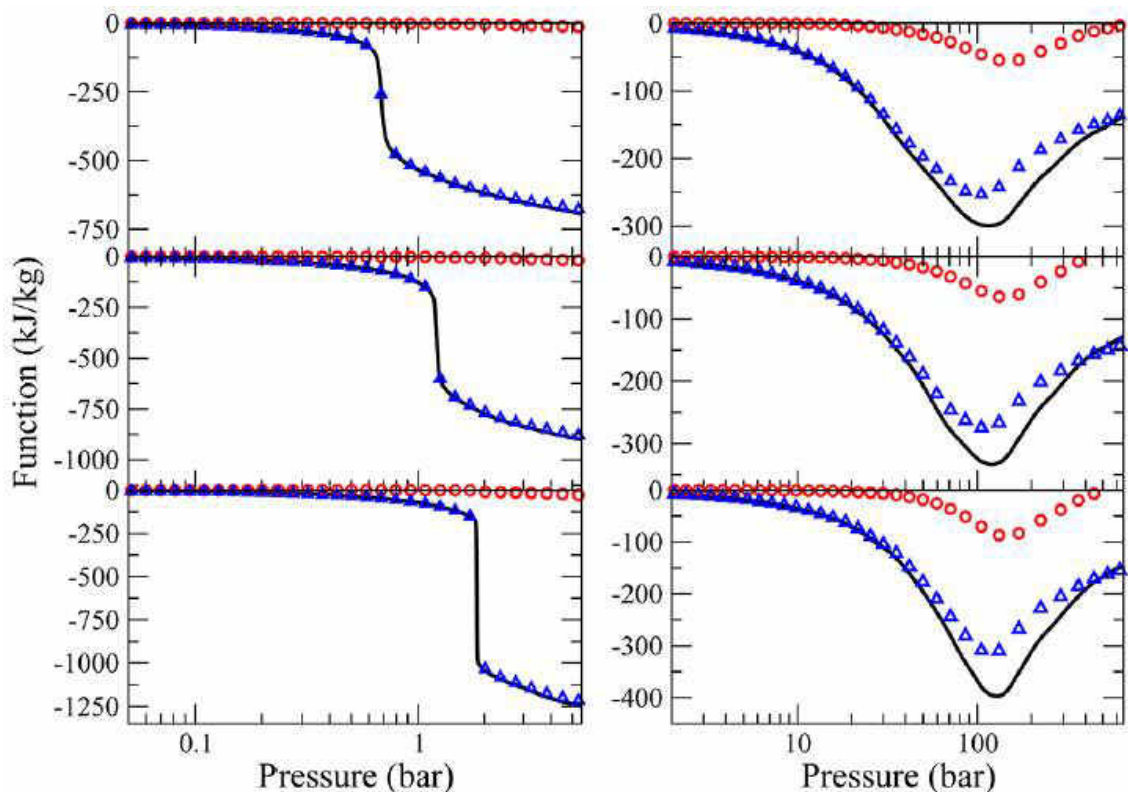


Figure 2.31. ΔH^e (solid line), ΔH^{comp} (circles), and ΔH^{imm} (triangles) against pressure at 220 K (left panel) and at 360 K (right panel). On both panels, results are shown for IRMOF-1 (top), IRMOF-8 (middle), and IRMOF-10 (bottom).⁹⁴

The next thermodynamic property discussed will be the entropy. The excess entropy functions (ΔS^e), the compression entropy functions (ΔS^{comp}), and the immersion entropy functions (ΔS^{imm}) for each IRMOF is given in Figure 2.32. In the same way that the variations in the results obtained for ΔG^e and ΔH^e , with respect to pressure, followed the trends of the excess adsorption isotherms in the subcritical and supercritical regimes, the variations in ΔS^e follow those same trends. However, in contrast to both of the behaviors of ΔG^e and ΔH^e , Figure 2.32 shows a significant contribution to ΔS^e from both ΔS^{comp} as well as ΔS^{imm} , with ΔS^{comp} playing a slightly more visible role in both the subcritical and supercritical regimes. The significance of the contribution of ΔS^{comp} can be attributed to

the sharp entropy loss as the gas is isothermally compressed from its ideal gas reference state to its equilibrium pressure. Quantitatively, e.g., at $P = 5$ bars and $T = 220$ K, ΔS^{comp} accounts for approximately 60% of the value of ΔS^e for each of the IRMOFs. In the case of $T = 360$ K and at a pressure close to the minimum of ΔS^e , ΔS^{imm} is about -0.5 kJ/kg/K for the three IRMOFs, which amounts to 20%, 16%, and 12% for IRMOF-1, IRMOF-8, and IRMOF-10, respectively.⁹⁴

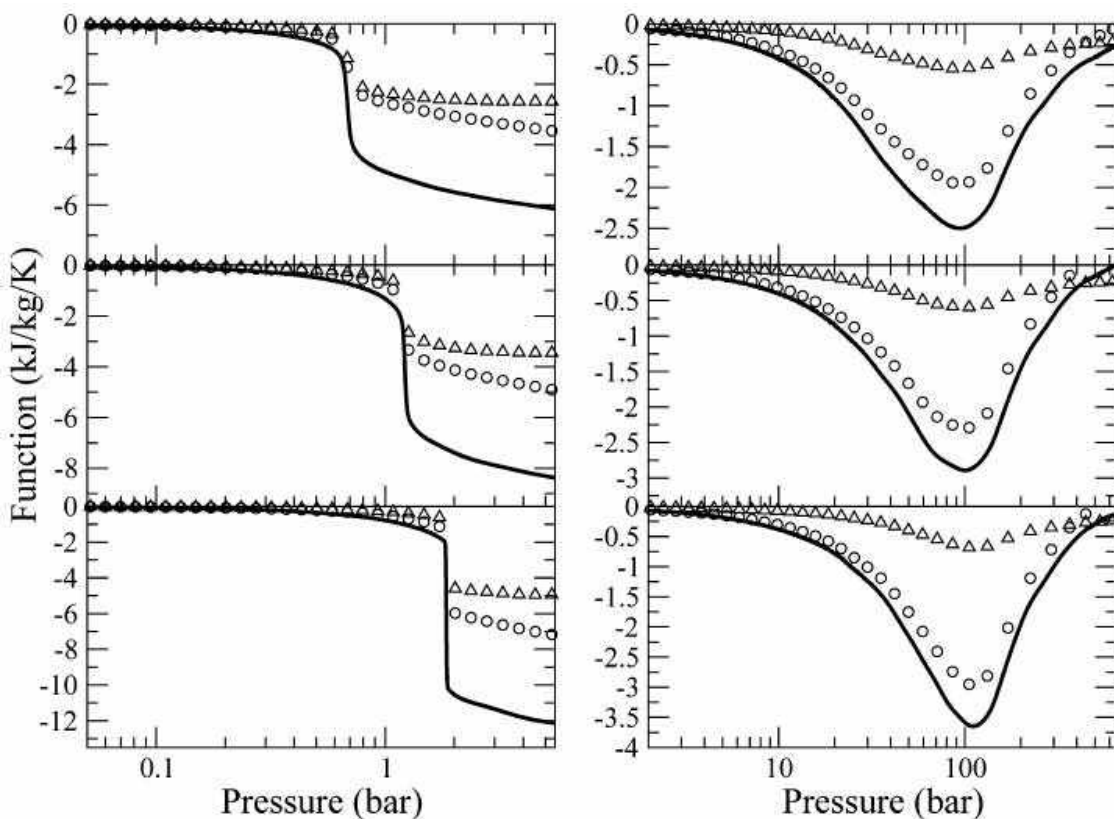


Figure 2.32. ΔS^e (solid line), ΔS^{comp} (circles), and ΔS^{imm} (triangles) against pressure at 220 K (left panel) and at 360 K (right panel). On both panels, results are shown for IRMOF-1 (top), IRMOF-8 (middle), and IRMOF-10 (bottom).⁹⁴

The next presented results are the desorption Gibbs free energy, enthalpy, and entropy which are plotted against pressure in Figure 2.33 in the subcritical (left panel) and supercritical (right panel) regimes for all three IRMOFs. As discussed above, since adsorption is a spontaneous and exothermic process, all of the immersion properties are all negative. Thus this implies that all the desorption properties are positive. For a given temperature, it was found that the features of these functions were qualitatively similar for the three IRMOFs. The desorption functions monotonically increase with pressure in the subcritical regime and possess a maximum in the supercritical regime.⁹⁴ It is worth noting that their relative magnitude, i.e., $H > TS > G$, follows the trend generally obtained for desorption properties.⁹⁵

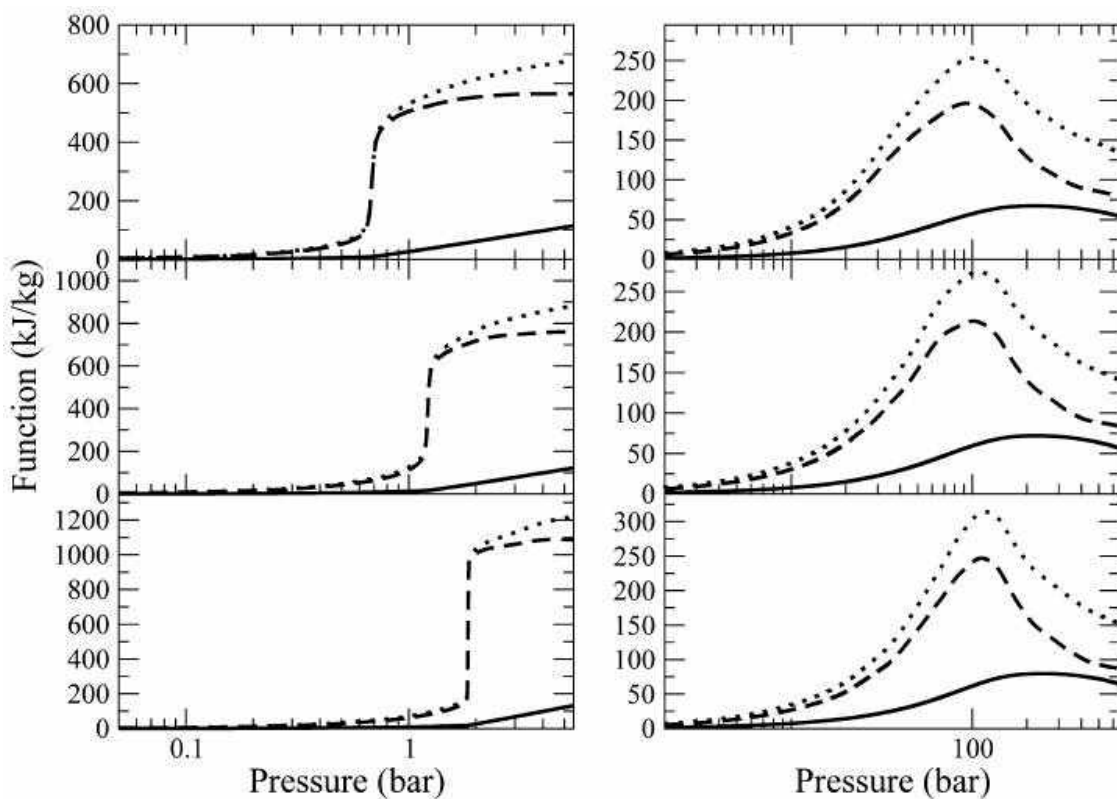


Figure 2.33. Desorption functions as a function of pressure at 220 K (left panel) and at 360 K (right panel). On both panels, results are shown for IRMOF-1 (top), IRMOF-8 (middle), and IRMOF-10 (bottom). G is shown with a solid line, H with a dotted line, and TS with a dashed line.⁹⁴

In Figure 2.34, the desorption free energy functions, or $|\Omega^e|$, for each of the IRMOFs studied in this work are presented. As mentioned earlier, $|\Omega^e|$ can be interpreted as the isothermal work required to degas each IRMOF at the various temperatures and pressures. In the displayed results, it can be seen that these desorption function exhibit two different trends, one that corresponds to the subcritical regime where $|\Omega^e|$ monotonically increases with pressure and one that corresponds to the supercritical regime with $|\Omega^e|$ exhibiting a maximum for each IRMOF. In a similar way to the results obtained for the other thermodynamic quantities, the sharp rise present in $|\Omega^e|$ is shifted toward high pressures as the pore size of the IRMOF increases.⁹⁴

Now in order to compare the performance of the three IRMOFs, the results given in Figure 2.34 must be examined more closely. When considering the maximum reached by the desorption free energy in the subcritical regime (220 K), the following ranking can be found: $|\Omega^e|(\text{IRMOF-1}) = 114 \text{ kJ/mol} < |\Omega^e|(\text{IRMOF-8}) = 121 \text{ kJ/mol} < |\Omega^e|(\text{IRMOF-10}) = 131 \text{ kJ/mol}$. When considering the maximum reached by the desorption free energy in the supercritical regime (360 K), the ranking is in the same order: $|\Omega^e|(\text{IRMOF-1}) = 67 \text{ kJ/mol} < |\Omega^e|(\text{IRMOF-8}) = 72 \text{ kJ/mol} < |\Omega^e|(\text{IRMOF-10}) = 79 \text{ kJ/mol}$. In both regimes, the cost of regenerating the adsorbent increased with the size of the IRMOF pores. Thus, at first inspection it would appear that IRMOF-1 would be the most efficient.

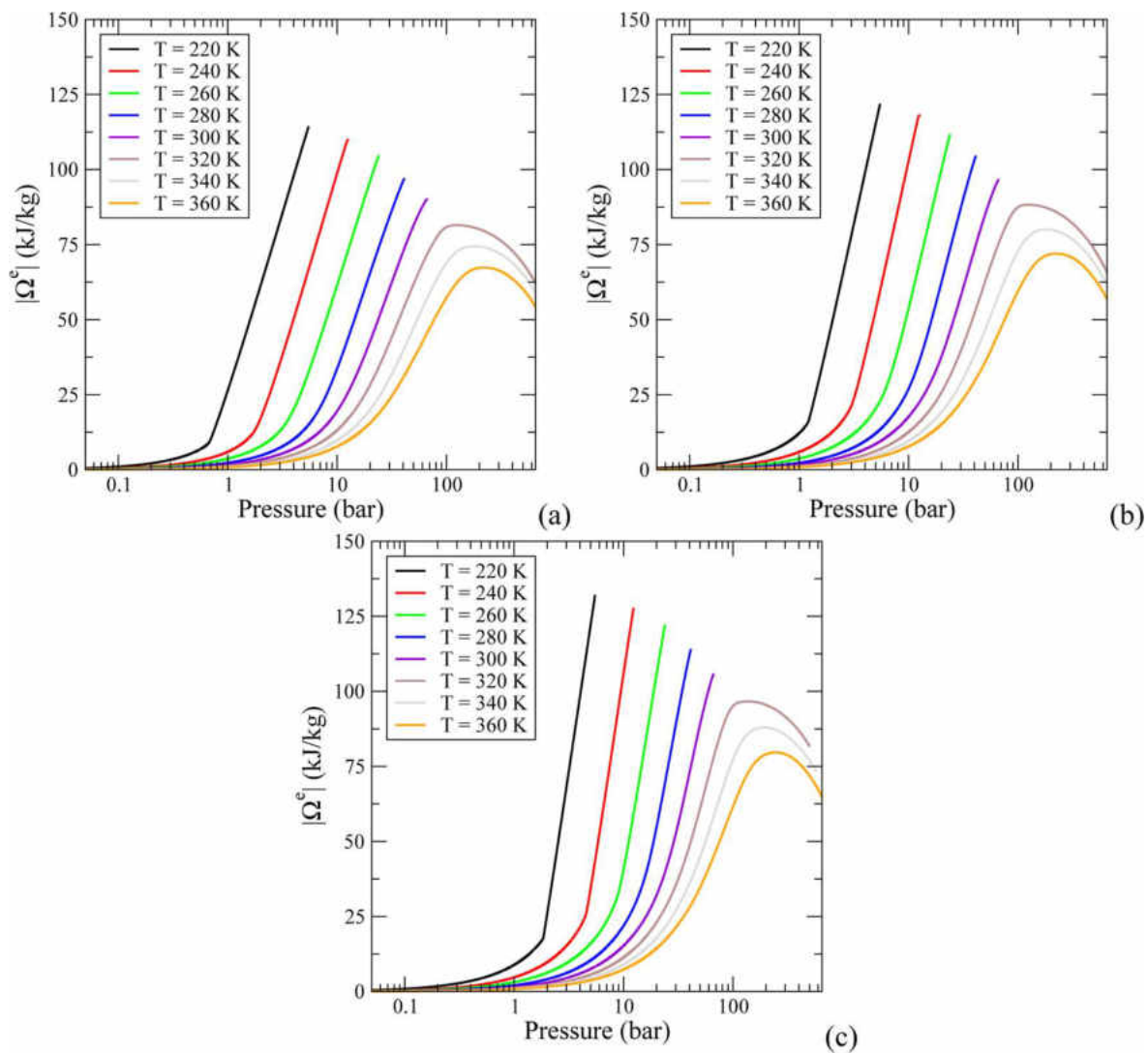


Figure 2.34. The desorption free energy, $|\Omega^e|$, plotted against pressure for: (a) IRMOF-1, (b) IRMOF-8, and (c) IRMOF-10.⁹⁴

However, the results presented in Figure 2.28 must also be considered, since the larger free volume allows for an increased maximum loading capacity of CO₂ molecules. Thus when considering both the maximum number adsorbed along with $|\Omega^e|$, one can see that the benefit IRMOF-10 has of having larger pore size more than makes up for its increased degassing cost. More specifically, this is because while there is about an 18% increase in the IRMOF regeneration cost, when comparing IRMOF-1 to IRMOF-10, there is about a 100% increase in the maximum amount of molecules that can be adsorbed. Thus, after careful inspection IRMOF-10 was found to be the most efficient, followed by IRMOF-8 and then by IRMOF-1.

2.5 CHAPTER CONCLUSION

From a methodological stand point, it can be concluded that WL sampling in the grand-canonical ensemble is a convenient and efficient method, since neither the pressure or chemical potential is needed *a priori*. It is also accurate when used to determine the densities of both phases of a vapor-liquid coexistence simulation. When WL sampling is used in the SEGC ensemble, a highly accurate estimate for the partition function can be obtained and through the formalism of statistical mechanics all the relevant thermodynamic properties can be obtained for a wide range of conditions. This can be accomplished in just a single simulation of the bulk gas phase and once per each porous crystal studied and thus yield the entire isotherm for the adsorbate.

From the standpoint of the discussed application, by studying CO₂ adsorption into IRMOF-1, IRMOF-8 and IRMOF-10, the minimum isothermal work required to regen-

erate each IRMOF was found and compared along with the maximum loading of each of those IRMOFs. It was found that as the free volume increased the cost of degassing also increased. However, the increased free volume more than offsets the extra cost of degassing. Thus from this work it was found that out of the IRMOFs studied, IRMOF-10 had the best performance for adsorbing CO₂, followed by IRMOF-8 and then by IRMOF-1.

Chapter 3

THEORETICAL STUDIES OF THE RELATIVE ENERGIES OF DIMERIC ARSENIC AND SELENIUM OXIDES

3.1 BACKGROUND

3.1.1 Motivations

The production of electricity through the combustion of coal has seen considerable use and is still being used more extensively than any other fuel to generate electricity. (A schematic representing the world's total electricity generation by fuel in 2009¹³⁹ is given in Figure 3.1). This is due to coal's availability, relatively high energy density and low costs. However, this process not only emits large quantities of CO₂ into the atmosphere, but the emitted hot flue gases are known to contain potentially hazardous trace elements. Since these trace elements can be harmful to the environment and human health as well as have adverse effects on the production of power, there has been an increasing interest in their mitigation. This requires a more detailed understanding of their kinetic reactivities and thermodynamic stabilities. This is especially true for the oxides of hazardous trace element present in the flue gases.¹⁴⁰ If a complete understanding of the chemical forms, oxidation states and structures are obtained, one should be able to use that information to aid in the alleviation of the trace elements' adverse effects on the environment, human health and power production.^{141–143} Two particularly relevant hazardous trace elements found in flue gases are arsenic^{140,144–146} and selenium.¹⁴⁷

Arsenic's level of toxicity depends on its form, concentration and oxidation state. The oxidation states in which arsenic is found are -3, +3 and +5, where arsenic in the +3 oxidation state in an inorganic compound is its most toxic form.¹⁴⁰ Arsenic is a chronic poison and poses a significant risk to humans, animals and plants alike. The organs which are most severely affected by arsenic poisoning are the gastrointestinal tract, the kidneys,

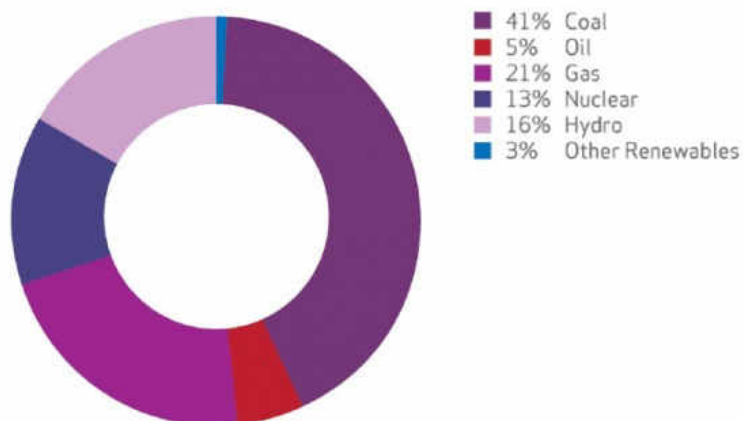


Figure 3.1. The 2009 total world electricity generation by fuel. Within the “Other Renewables” category are solar, wind, combustible renewables, geothermal and waste. Figure taken from reference 139.

the circulatory system, the liver, and the skin.¹⁴⁸ It is known to cause several illnesses such as ischemic heart disease,¹⁴⁹ diabetes,¹⁵⁰ hypertension,¹⁵¹ peripheral vascular disease and cancers of the bladder, liver, lung and skin.^{152–154} In Bangladesh, for example, there has been a history of similar illnesses to those listed above because of excess arsenic in their drinking water.¹⁵⁵ Besides arsenic’s terrible effect on human health and the environment, it is also known to have adverse effects on the production of power. Specifically, it poisons the catalytic converter used in the selective catalytic reduction of NO_x , thereby increasing the cost of NO_x control.^{140,156} It is clear that controlling the emission of arsenic in flue gases is of utmost importance.

In order to control the emission of arsenic, it is necessary, among other things, to understand the mechanisms that lead to the formation of the various arsenic containing compounds as well as the relative energies of their corresponding isomers. The forms in which arsenic is likely to occur in flue gases during coal combustion is either in its elemental

form or in the form of oxides.^{144,157} Up to present there have been a few experimental and theoretical studies on the monomeric oxides, AsO, AsO₂ and AsO₃.^{158–160} However, there is even less known concerning the corresponding dimeric oxides, As₂O₃ and As₂O₅, although these compounds are expected based on the similarity to nitrogen and phosphorus chemistry. From an experimental perspective, they are very challenging to study due to the high temperatures, complex chemical environments and low concentrations needed for a direct study of the form and structures of the dimeric oxides in flue gases. Thus, a theoretical study may be the best way to study these compounds.

Similar to arsenic, selenium's biochemical impact depends on its form, concentration and oxidation state. Selenium is known to exist with oxidation numbers of -2, 0, +2, +4, and +6; therefore, selenium can support many different bonding environments.^{147,161} Due to selenium's relatively high volatility when compared to other trace elements present in coal, e.g., arsenic, it has one of the highest concentrations present in flue gases being released to the environment.^{161–163} Selenium, unlike arsenic, is both an essential and toxic element where the margin between the essential and toxic quantity is known to be small and not known precisely.^{143,147,164–166} Selenium is known to act as an antioxidant and to protect cell membranes¹⁴³ and it was also reported to act as an anti-carcinogenic agent, where, through the use of selenium enriched yeast, the development of lung, colorectal and prostate cancers were significantly limited.¹⁶⁷ However, animals that have ingested forage with a concentration of selenium of 1mg/kg or more were reported to have selenium poisoning. About 500 cases of human selenium poisoning, i.e., selenosis, were reported in southern China due to corn grown in soil laden with stony coal (i.e., carbonaceous shale).¹⁶⁸ There have even been cases where selenium deficiencies as well as selenium poisoning

were reported in regions quite similar and relatively close to one another.¹⁴⁷

Though the amount of selenium one is exposed to is a crucial variable for the determination of whether it will be harmful or beneficial, the form in which the selenium exists plays a undeniable role in its toxicity as well. More specifically, selenium's form is known to be directly related to its metabolic activity, anti-carcinogenic activity and absorption (e.g., the inorganic forms of selenium are known to be more toxic than some organic forms like selenomethionine).^{164,169} Thus, since selenium can be either beneficial or toxic depending on its concentration as well as the form in which it exists, there is a definite need to better understand the various forms and relative abundances of those forms in the environment. In particular, there is a need to study the mechanisms which lead to the formation of the various selenium containing compounds in flue gases and the relative energies of the various isomers of those compounds, since those may be the compounds being released into the environment.

Like arsenic, selenium is known to exist in flue gases and thus released into the environment in its elemental form, Se, or in the form of the monomeric oxides, SeO and SeO₂.^{146,147,161,163} There have been several experimental studies concerning the selenium monomeric oxides, SeO, SeO₂ and SeO₃,^{147,158,161,163,170,171} as well as a few theoretical studies.^{158,159,172} However, little is known concerning the corresponding selenium dimeric oxides,^{171,175,176} Se₂O₃ and Se₂O₅, which can be expected from the consideration of sulfur chemistry, where polymeric forms of the monomeric oxides exist. Understanding these dimeric oxides may play a significant role in understanding selenium's environmental chemistry,^{170,173-175} little is known about these compounds. In the same way that experimental studies of the arsenic dimeric oxides would be quite difficult, an *in situ* experimen-

tal study on the structure and form of the selenium oxides would prove to be a significant challenge. However, both arsenic and selenium oxides can be studied theoretically and this is the primary focus of the work presented in this chapter of my thesis.

3.1.2 Computational Chemistry

In order to effectively and efficiently study these oxides theoretically, high level *ab initio* methods, which provide a balanced treatment of both dynamical and non-dynamical (i.e., multireference) electron correlation, are needed. This is particularly important when mapping the potential energy surface of a species (e.g., Se_2O_5) where bond breaking and forming is experienced as the isomers interconvert. Previously, Monahan-Pendergast et al. used several *ab initio* methods to study arsenic and selenium monmeric oxides released into the atmosphere due to coal-fired power plant emissions, and they found five thermodynamically favored reactions which where were more likely to go to completion under tropospheric conditions than stratospheric conditions.¹⁵⁸ More relevant to this thesis, several arsenic and selenium monomeric oxides were studied by Urban and Wilcox.^{159,172} Their results showed that the quadratic configuration interaction that corrects for size-consistency errors in the all singles and double excitation CI methods, i.e., QCISD, the further improved method, i.e., QCISD(T), which perturbatively includes the unlinked triples, the coupled cluster method with single and double excitation, i.e., CCSD, and the improved method which perturbatively includes the unlinked triples, i.e., CCSD(T), outperformed DFT using the B3LYP functional^{39,40} involving a relativistic effective core potential, i.e., B3LYP/RECP. However, since all of the above listed methods are single reference-based approaches, the multireference character of the selenium and arsenic oxides must be as-

sessed. In this thesis, a relatively recently developed method, which allows for the potential multireference character of the species studied is used; in particular, the second-order generalized Van Vleck variant of multireference perturbation theory (GVVPT2) was used.^{177–179}

GVVPT2 has proven itself successful in many similar applications where difficult multireference structures were studied. A few relevant examples include disulfur monoxides, i.e., S_2O ,¹⁸⁰ mercury oxidation and binding on activated carbon present in flue gas,¹⁸¹ azabenzenes,¹⁸² and, even more relevant to the work presented in this thesis, dioxiranes and other compounds similar in nature.¹⁸³ GVVPT2 has been shown to produce results in good agreement with CCSD¹⁸⁴ and CCSD(T)¹⁸⁵ when those methods are applicable.

In this thesis, only the results obtained from my work directly will be presented in detail, while the relevant results obtained by others will be briefly described. In particular, the relative energies, obtained using GVVPT2 with the cc-pVDZ¹⁸⁶ and cc-pVTZ¹⁸⁷ basis sets, of the various isomers of As_2O_3 , As_2O_5 , Se_2O_3 and Se_2O_5 along with the relevant transition states between them, were studied and will be presented in-depth. One isomer of each species is shown in Figure 3.2 to give examples of the compounds studied. The details on the general procedure used to obtain the GVVPT2 energies of the arsenic and selenium oxides is given below in Section 3.2 along with a brief introduction on each of the methods used.

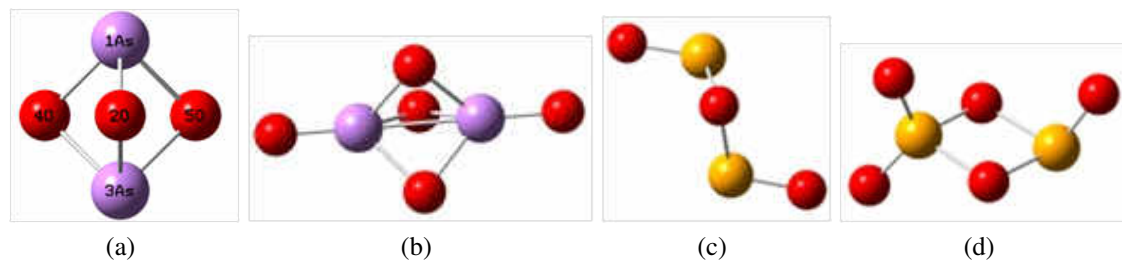


Figure 3.2. Examples of the isomers of As_2O_3 (a), As_2O_5 (b), Se_2O_3 (c) and Se_2O_5 respectively. Oxygen is red, arsenic is purple and selenium is yellow.

3.2 METHODS

The general process or computational protocol used in this thesis can be broken up into the following six steps. First, the basis sets were obtained from literature which, when simply put, are the functions needed to describe the atomic orbitals (AOs). Second, the geometries for the isomers and their transition states were generated through the use of density functional theory (DFT) with the B3LYP functional as implemented in the Gaussian 03 program.¹⁸⁸ Third, a restricted Hartree-Fock (RHF) and a restricted Møller-Plesset perturbation (RMP2)¹⁹¹ calculation was performed to obtain an initial approximation of the molecular orbitals (MOs). Fourth, the obtained data, along with chemical knowledge concerning e.g., valence orbitals, was used to generate an active space that can accurately describe each of the structures considered. Fifth, a multiconfigurational self-consistent field (MCSCF) calculation was performed to further refine the MOs. Sixth, a 2nd order generalized Van Vleck perturbation theory (GVVPT2)¹⁷⁷⁻¹⁷⁹ calculation was conducted to add in the dynamical electron correlation resulting in an accurate value of the single point energy of the molecule. The results were then compared to those obtained with established theoretical methods and experimental data when available. The obtained energies of each

of the structures were then compared with the other structures of a given species to discover their relative stabilities.

Being that there was no experimental or theoretical data currently in the literature on the structures of Se_2O_3 , Se_2O_5 , As_2O_3 or As_2O_5 , a way was needed to test if the above protocol is giving accurate results. Therefore, the above protocol was first tested by characterizing the arsenic and selenium monomeric oxides, which have both experimental and theoretical data. This was conducted by Wanyi Jiang and Rashel M. Mokambe and the results were found to be in excellent agreement with the established literature values.

The simplest electronic structure method employed in the above mentioned protocol, the Hartree-Fock approximation, is described first in this section. This is for two reasons: (i) introduce notation so as to make this thesis easier to follow; and (ii) the Hartree-Fock approximation serves as a useful reference for many of the other higher level theoretical methods. Once the Hartree-Fock foundation has been laid, a brief description of MP2 is given. Lastly, a summary of the MCSCF and GVVPT2 methods will be given along with a description of the macroconfigurational approach used in the work presented in this thesis.

3.2.1 Hartree-Fock Approximation

The well-known Schrödinger equation or more specifically, the time-independent Schrödinger equation, is given by

$$\hat{H}\Psi = E\Psi \tag{3.1}$$

where \hat{H} is the Hamiltonian operator, Ψ is the wavefunction of a specific state of the system and E is the corresponding energy corresponding to that state. A commonly used notation in quantum chemistry is Dirac notation, in which eq 3.1 is written as

$$\hat{H}|\Psi\rangle = E|\Psi\rangle \quad (3.2)$$

It is on this foundational equation that modern quantum chemistry is built upon. Once the wave function is known for the system, all (time-independent) chemical and physical information can be obtained. The non-relativistic Hamiltonian operator, \hat{H} , which is the operator corresponding to the total energy of the system is given by

$$\hat{H} = \hat{T} + \hat{V} = -\frac{\hbar}{2m}\nabla^2 + V(\mathbf{r}) \quad (3.3)$$

where \hat{T} is the kinetic energy operator, \hat{V} is the potential energy operator, $\hbar = h/2\pi$, m is the mass of the particle and ∇ is the gradient operator so that ∇^2 is the Laplacian operator. When the Hamiltonian operator, for a system containing M atoms and N electrons, is separated out so that each term represents a specific contribution, it can be written using atomic units as¹⁸⁹

$$\hat{H} = -\sum_{i=1}^N \frac{1}{2}\nabla_i^2 - \sum_{A=1}^M \frac{1}{2M_A}\nabla_A^2 - \sum_{i=1}^N \sum_{A=1}^M \frac{Z_A}{r_{iA}} + \sum_{i=1}^N \sum_{j>i}^N \frac{1}{r_{ij}} + \sum_{A=1}^M \sum_{B>A}^M \frac{Z_A Z_B}{R_{AB}} \quad (3.4)$$

where M_A is the ratio of the mass of the nucleus A to the mass of an electron, Z_A is the atomic number of nucleus A , the Laplacian operators ∇_i^2 and ∇_A^2 involves differentiation

with respect to the coordinates of the i th electron and the A th nucleus. As mentioned above, each term corresponds to a specific contribution. The first term is the kinetic energy operator for the electrons, the second term is the kinetic energy operator for the nuclei, the third term represents the coulomb attraction between electrons and nuclei, the fourth term repulsion potential between electrons and the fifth term represents the repulsion potential between the nuclei.

Since the nuclei have significantly larger masses than the electrons, they move much slower than the electrons. Therefore, one can invoke the first (and most common) of many approximations in quantum chemistry: the Born-Oppenheimer approximation.¹⁹⁰ In this approximation, the nuclei are considered fixed and the electrons are moving in the potential field of the nuclei. Thus, the wavefunction of the electrons and the nuclei can be treated separately from each other

$$|\Psi\rangle = |\Psi^{el}\rangle|\Psi^{nuc}\rangle \quad (3.5)$$

where the superscripts el and nuc correspond to the electrons and nuclei, respectively. The electronic Hamiltonian is then given by

$$\hat{H}_{el} = - \sum_{i=1}^N \frac{1}{2} \nabla_i^2 - \sum_{i=1}^N \sum_{A=1}^M \frac{Z_A}{r_{iA}} + \sum_{i=1}^N \sum_{j>i}^N \frac{1}{r_{ij}} \quad (3.6)$$

Then, since the first term corresponds to the kinetic energy of the electrons, the second term corresponds to the nuclear-electron attraction and the third term corresponds to the electron-electron repulsion, the electronic Schrödinger equation can be written as

$$\hat{H}_{el}|\Psi^{el}\rangle = \left[\sum_{i=1}^N \hat{T}_i^{el} + \sum_{i=1}^N \sum_{A=1}^M \hat{V}_{i,A}^{el,nuc} + \sum_{i=1}^N \sum_{j>i}^N \hat{V}_{i,j}^{el,el} \right] |\Psi^{el}\rangle = E_{el}|\Psi^{el}\rangle \quad (3.7)$$

When this is solved for various nuclear positions or geometries, a potential energy surface can be obtained. This is important when attempting to find equilibrium geometries and vibrational frequencies. Unfortunately, eq 3.7 can only be solved exactly for a few very simple systems. This is because of the $\hat{V}_{i,j}^{el,el}$ term (i.e., the electron-electron repulsion term).

At the most naive level, $\hat{V}_{i,j}^{el,el}$ can be approximated by replacing it with an average or mean electric field generated by all of the other electrons in the system, $\hat{V}_{i,j}^{el,el} \approx V_i(\phi_1, \phi_2, \dots, \phi_N)$. Thus, by neglecting the instantaneous interactions, the electronic Hamiltonian and the total electronic energy can be separated and the electronic wavefunction, $|\Psi^{el}(\mathbf{r}_1, \mathbf{r}_2, \dots, \mathbf{r}_N)\rangle$, would just become the product of N one-electron wavefunctions, $\prod_i^N |\phi_i^{el}(\mathbf{r}_i)\rangle$. This is known as the Hartree approximation. Through the use of this approximation, the electronic Schrödinger equation becomes

$$\hat{H}_{el}|\Psi^{el}\rangle = \sum_{i=1}^N \left[\hat{T}_i^{el} + \sum_{A=1}^M \hat{V}_{i,A}^{el,nuc} + \hat{V}_i(\phi_1, \phi_2, \dots, \phi_N) \right] \prod_i^N |\phi_i^{el}(\mathbf{r}_i)\rangle = \sum_i^N E_i \prod_i^N |\phi_i^{el}(\mathbf{r}_i)\rangle = E_{el}|\Psi^{el}\rangle \quad (3.8)$$

However, the Hartree approximation has a serious problem in that it does not account for the Pauli exclusion principle. More specifically, the antisymmetry principle states that a wave function of fermions must be antisymmetric with respect to the interchange of any set of spin space coordinates $\mathbf{x} = \{\mathbf{r}, \omega\}$. Here, ω represents the spin coordinate (i.e., spin

α or spin β) and \mathbf{r} corresponds to the three spatial degrees of freedom. When including the spin degrees of freedom, the product of orbitals changes from the exclusively spatial orbital form, $\phi^{el}(\mathbf{r}_i)$ to the spin orbital form, $\chi^{el}(\mathbf{x})$, then

$$\Psi^{el}(\mathbf{x}_1, \mathbf{x}_2, \dots, \mathbf{x}_N) = \chi_i^{el}(\mathbf{x}_1), \chi_j^{el}(\mathbf{x}_2), \dots, \chi_k^{el}(\mathbf{x}_N) \quad (3.9)$$

Now, in order to satisfy the antisymmetry principle the relation,

$$\Psi^{el}(\mathbf{x}_1, \mathbf{x}_2) = -\Psi^{el}(\mathbf{x}_2, \mathbf{x}_1) \quad (3.10)$$

must be obeyed. This is accomplished through the use of what is called a Slater determinant; its inclusion alters the Hartree approximation to become the Hartree-Fock approximation. A Slater determinant is a determinant of spin orbitals and, for a system of N electrons, it can be written as

$$\Psi^{el}(\mathbf{x}_1, \mathbf{x}_2, \dots, \mathbf{x}_N) = \frac{1}{\sqrt{N!}} \begin{vmatrix} \chi_1(\mathbf{x}_1) & \chi_2(\mathbf{x}_1) & \dots & \chi_N(\mathbf{x}_1) \\ \chi_1(\mathbf{x}_2) & \chi_2(\mathbf{x}_2) & \dots & \chi_N(\mathbf{x}_2) \\ \vdots & \vdots & \ddots & \vdots \\ \chi_1(\mathbf{x}_N) & \chi_2(\mathbf{x}_N) & \dots & \chi_N(\mathbf{x}_N) \end{vmatrix} \quad (3.11)$$

where the factor $\frac{1}{\sqrt{N!}}$ is the normalization factor. Note that the rows of the determinant are labeled by electron coordinates and the columns are labeled by the spin orbitals. Therefore, if two rows are interchanged, it would be as if the coordinates of two electrons were interchanged. Thus, due to the mathematical nature of the determinant, this would change its sign, resulting in satisfaction of the requirements of the antisymmetry principle. Fur-

thermore, if two electrons with the same coordinates occupy the same spin orbital, there would be two equal columns in the determinant, making the determinant equal to zero. This representation fully satisfies the Pauli exclusion principle.¹⁸⁹ By this representation, as an example, the Hartree-Fock wavefunction for a simple two electron system is given as

$$\Psi^{el}(\mathbf{x}_1, \mathbf{x}_2) \cong \Psi_{HF}(\mathbf{x}_1, \mathbf{x}_2) = \frac{1}{\sqrt{2!}} [\chi_1(\mathbf{x}_1)\chi_2(\mathbf{x}_2) - \chi_1(\mathbf{x}_2)\chi_2(\mathbf{x}_1)] \quad (3.12)$$

Typically, in the Hartree-Fock approximation, the electronic Hamiltonian is written as

$$\hat{H}_{el} = \sum_{i=1}^N [h(i) + \hat{V}_i(\phi_1, \phi_2, \dots, \phi_N)] = \sum_{i=1}^N [h(i) + v^{HF}(i)] = \sum_{i=1}^N \hat{f}_i \quad (3.13)$$

where \hat{f}_i is the Fock operator, $v^{HF}(i)$ is the average potential experienced by the i th electron due to the electric field from the rest of the electrons and $h(i)$ is a term containing only one-electron terms, given by

$$h(i) = -\frac{1}{2}\nabla_i^2 - \sum_{A=1}^M \frac{Z_A}{r_{iA}} \quad (3.14)$$

The Hartree-Fock method is used to obtain a starting guess of the MOs from the AOs, where the MOs would then be used in some higher levels of theory to generate a more accurate description of the system. In practice, the MOs are obtained as a linear combination of a set of AO basis functions, which are typically Gaussian-type functions centered around the atoms.¹⁸⁹ Thus, the optimized MOs, denoted by ψ_i , are given by

$$\psi_i = \sum_{\mu=1}^n C_{\mu i} \phi_{\mu} \quad (3.15)$$

where ϕ_μ is the μ th basis function and n is the total number of the basis functions in the basis set. Now, the way that the Hartree-Fock method obtains the MOs is by iteratively minimizing the energy, E_{HF} , where each iteration results in a new, more correct value of the coefficients, $C_{\mu i}$, which are then used in the next iteration. Because the iterations continuously improve the energy until the change to the energy with respect to the change in the coefficient, $C_{\mu i}$, is negligible, the Hartree-Fock method is often called the self-consistent field (SCF) method. This eventually results in a decent starting guess for the MOs, ψ_i . This minimization process an example of the variational method. The variational theorem states that the energy of an approximate wavefunction is always larger than the true energy. The Hartree-Fock energy, when the wavefunctions are normalized, is calculated by

$$E_{HF} = \langle \Psi_{HF} | \hat{H}_{el} | \Psi_{HF} \rangle \quad (3.16)$$

The type of HF used in this thesis is known as restricted Hartree-Fock, or RHF, where the same set of spatial orbitals are used to describe two electrons that possess opposite spins. Though the HF method is computationally inexpensive and it can give good starting estimates for MOs, neglecting electron correlation can lead to large deviations from experimental results. There have been a number of approaches to attempt to remedy this weakness, collectively these methods are known as post-Hartree-Fock methods. They have been devised to include electron correlation to the multi-electron wave function. One of these approaches, 2nd order Møller-Plesset perturbation theory (MP2),¹⁹¹ treats correlation as a perturbation of the Hartree-Fock wavefunction, and a summary of that method is given below.

3.2.2 Second Order Møller-Plesset Perturbation Theory

Møller-Plesset perturbation theory improves on the Hartree-Fock method by adding electron correlation effects by means of Rayleigh-Schrödinger perturbation theory (RS-PT), usually to second order, i.e., MP2. MP2 is considered the simplest and computationally least expensive *ab initio* method for including electron correlation effects.^{192,193} In the work presented in this thesis, it was used to take the HF solution, including basis set and molecular geometry information, of a given isomer and create a rough estimate of the unoccupied MOs energy and give the relative occupancies of the occupied MOs (i.e., it gives natural orbitals). This information was then used to develop an active space, i.e., the MO's which are considered as the most chemically relevant which are typically broken up into different categories, e.g., mostly occupied and mostly unoccupied.

In MP2 rather than approaching the system variationally, like the HF treatment of orbitals, the total Hamiltonian of the system is expanded into two parts. The first part, \hat{H}_0 , is called the zero order term, while the second part, $\lambda\hat{V}$, is called the perturbation term. The form of the MP Hamiltonian is then

$$\hat{H} = \hat{H}_0 + \lambda\hat{V} \quad (3.17)$$

where λ is an arbitrary real parameter and \hat{H}_0 is given by

$$\hat{H}_0 = \sum_{i=1}^N [h(i) + v^{HF}(i)] \quad (3.18)$$

and the perturbation, V , is given by

$$V = \sum_{i < j}^N \frac{1}{r_{ij}} - \sum_{i=1}^N v^{HF}(i) \quad (3.19)$$

Now, MP theory is a special case of RS-PT. In RS-PT the perturbed wave function and perturbed energy are expressed as a power series in λ . Then, the perturbed wavefunction of the system is

$$\Psi = \lim_{n \rightarrow \infty} \sum_{i=0}^n \lambda^i \Psi^{(i)} \quad (3.20)$$

and the perturbed energy of the system is

$$E = \lim_{n \rightarrow \infty} \sum_{i=0}^n \lambda^i E^{(i)} \quad (3.21)$$

When eqs 3.17, 3.20 and 3.21 are substituted into the time-independent Schrödinger equation (i.e., eq 3.1), then a new equation is obtained

$$(\hat{H}_0 + \lambda \hat{V}) \left(\lim_{n \rightarrow \infty} \sum_{i=0}^n \lambda^i \Psi^{(i)} \right) = \left(\lim_{n \rightarrow \infty} \sum_{i=0}^n \lambda^i E^{(i)} \right) \left(\lim_{n \rightarrow \infty} \sum_{i=0}^n \lambda^i \Psi^{(i)} \right) \quad (3.22)$$

where $n \rightarrow \infty$ and λ^k corresponds to a k th-order perturbation and in the case of MP2, $k = 2$.

Now, since the Hartree-Fock Slater determinant, $|\Psi_0^{(0)}\rangle$, is an eigenfunction of \hat{H}_0 ,

$$\hat{H}_0 |\Psi_0^{(0)}\rangle = E_0^{(0)} |\Psi_0^{(0)}\rangle \quad (3.23)$$

where the eigenvalue is given by

$$E_0^{(0)} = \sum_i \varepsilon_i \quad (3.24)$$

in which ε_i is the orbital energy of the i th electron. It is important to note that the Hartree-Fock energy of the system is different than the 0th-order energy given above since the Hartree-Fock Hamiltonian is the exact Hamiltonian.

Now, the 1st-order correction to the energy of the system is given by

$$E_0^{(1)} = \langle \Psi_0 | \hat{V} | \Psi_0 \rangle \quad (3.25)$$

and after the expression for \hat{V} , given in eq 3.19, is substituted in,

$$E_0^{(1)} = \langle \Psi_0 | \sum_{i < j} \frac{1}{r_{ij}} | \Psi_0 \rangle - \langle \Psi_0 | \sum_i v^{HF}(i) | \Psi_0 \rangle \quad (3.26)$$

then,

$$E_0^{(1)} = \frac{1}{2} \sum_i \sum_j ([ii|jj] - [ij|ji]) - \sum_i [i|v^{HF}(i)|j] \quad (3.27)$$

which simplifies to give the 1st-order energy

$$E_0^{(1)} = -\frac{1}{2} \sum_i \sum_j ([ii|jj] - [ij|ji]) \quad (3.28)$$

Note that when $E_0^{(0)}$ and $E_0^{(1)}$ are summed together, one simply gets the Hartree-Fock energy, E_0^{HF} . Thus, in order to obtain the needed correlation energy, 2nd-order or higher is needed.

Now, the 2rd-order correction to the energy of the system is given by

$$E_0^{(2)} = \sum_n \frac{|\langle \Psi_0 | \hat{V} | \Psi_n \rangle|^2}{E_0^{(0)} - E_n^{(0)}} \quad (3.29)$$

where $|\Psi_n\rangle$ is a Slater determinant corresponding to an excited electron configuration relative to the HF reference state. Only a double excitation determinant, $|\Psi_{ij}^{ab}\rangle$, yields a non-zero contribution to the energy with

$$\langle \Psi_0 | \sum_{i<j} \frac{1}{r_{ij}} |\Psi_{ij}^{ab}\rangle = [ia|jb] - [ib|ja] \quad (3.30)$$

The energy eigenvalue of the doubly excited determinate is $E_0^{(0)} - \varepsilon_i - \varepsilon_j + \varepsilon_a + \varepsilon_b$, i.e.,

$$\hat{H}_0 |\Psi_{ij}^{ab}\rangle = (E_0^{(0)} - \varepsilon_i - \varepsilon_j + \varepsilon_a + \varepsilon_b) |\Psi_{ij}^{ab}\rangle \quad (3.31)$$

Therefore, the second order energy correction is given by

$$E_0^{(2)} = \sum_{i<j} \sum_{a<b} \frac{|\langle \Psi_0 | \sum_{i<j} \frac{1}{r_{ij}} |\Psi_{ij}^{ab}\rangle|^2}{\varepsilon_i + \varepsilon_j - \varepsilon_a - \varepsilon_b} = \sum_{i<j} \sum_{a<b} \frac{[ia|jb] - [ib|ja]}{\varepsilon_i + \varepsilon_j - \varepsilon_a - \varepsilon_b} \quad (3.32)$$

Thus, the MP2 energy can be written as

$$E_0^{MP2} = E_0^{(0)} + E_0^{(1)} + E_0^{(2)} = E_0^{HF} + E_0^{(2)} \quad (3.33)$$

The type of MP2 used in this thesis is known as restricted Second Order Møller-Plesset Perturbation Theory, or RMP2, where the same set of spatial orbitals are used to describe two electrons that possess opposite spins. RMP2 provides an initial approximation of the molecular orbitals using what is known as natural orbitals (NOs) in its output. These nat-

ural orbitals give value ranging from 2.00-0.00, where an NO with a value of 2.00 would correspond to an MO that is always doubly occupied and an NO with a value of 0.00 would correspond to an MO that is never occupied. The NOs generated from the RMP2 calculations were helpful in devising the active spaces used in later, higher level calculations.

Since MP2 is a single-reference method, only ground state electron configurations can be well described, but this limitation can be addressed through another post-Hartree-Fock method, like the multi-configurational self-consistent field (MCSCF) method, which includes some electron correlation by expanding the multi-electron wave function in terms of a linear combination of Slater determinants and is explained in greater detail below.

3.2.3 Multi-Configurational Self-Consistent Field Theory

MCSCF is a multi-configurational method since several electron configurations are used rather than just one. In the presented work of this thesis, MCSCF was used to refine the MOs and energies obtained from RMP2; using the natural orbitals obtained from RMP2 cut down on the total time required for the above described computational protocol.

There are, in fact, some systems which can be reasonably described through the use of single-reference methods, where Hartree-Fock is a decent zero-order approximation from where correlation energies can be calculated. However, there are many cases in chemistry where a single-reference description just is not accurate enough. Processes such as bond breaking and forming as well as many excitations of the electronic state of an atom or molecule require a multi-reference method. This is because the Hartree-Fock determinant may no longer dominate the system's wavefunction due to other important electronic configurations. Several known examples where a single-reference description fails are: diradi-

cals, unsaturated transition metals, excited states and often transition states. In these cases the use of a Hartree-Fock wavefunction as a reference fails to produce sufficiently accurate results thereby causing subsequent higher level methods to also produce inaccurate results.

Therefore a multi-configurational method is needed to generate a reference wavefunction which can be used by a multireference perturbation theory, such as GVVPT2. This is particularly true for the work presented in this thesis since many of the systems involve the formation and breaking of bonds and many molecules considered are transition state structures. The MCSCF method has shown itself to be an excellent way to generate a multi-reference wavefunction, the general form of which is given by

$$|\Psi_{MCSCF}\rangle = \sum_I A_I |\Psi_I\rangle \quad (3.34)$$

where A_I are the corresponding configuration mixing coefficients of the I th configuration state function (CSF), Ψ_I , which is given by

$$\Psi_I = \mathcal{A}_I \left\{ \prod_{i \in I} \psi_i \right\} \quad (3.35)$$

The difference in the arrangement of electrons in the molecular orbitals, ψ_i , and the spin-coupling differentiate one electronic configuration from another where ψ_i was given earlier by eq 3.15. It is worth noting that in MCSCF the configuration mixing coefficients, A_I , as well as the MO expansion coefficients, $C_{\mu i}$, are variationally optimized, while in a method like configuration interaction (CI), only the configuration mixing coefficients are optimized.

In an MCSCF calculation, the user developed active space (or model space) dictates

which electron configuration to use in the calculation. There are two widely used approaches, the complete active space SCF (CASSCF)¹⁹⁴ approach and the restricted active space SCF (RASSCF).^{195,196} In CASSCF the valence electrons are distributed in all possible ways among MOs in the active space. However, this can be very computationally expensive since the number of CSFs rapidly increase with the number of active MOs. In RASSCF, a smaller set of CSFs can be obtained by restricting the number of electrons in certain orbital groups. More specifically, the orbitals in a RAS model space are broken up into three categories: orbitals with a limited number of vacancies (i.e., holes), fully active orbitals and orbitals with a limited number of electrons. Rather than being limited to a CASSCF or a RASSCF, the work in this thesis used what is known as the macroconfiguration approach developed in Prof. Hoffmann's group.¹⁹⁷

In the macroconfiguration approach, the construction of chemically relevant, physically reasonable and relatively compact model spaces can be achieved. This approach can provide significant efficiency improvements in the results obtained from methods like MCSCF and GVVPT2. It allows the user to construct truncated configuration spaces, which describe the non-dynamic part of the correlation energy while still providing good references for obtaining a proper description of the dynamic electron correlation. This can be accomplished due to the macroconfiguration approach's excellent but systematic flexibility.

Generally, when considering a fixed partitioning, $N = (N_1, N_2, \dots, N_g)$ of N electrons in g disjoint orbital groups $\{G_1, G_2, \dots, G_g\}$, the corresponding macroconfiguration is given by

$$(N) : \{G_1^{N_1}, G_2^{N_2}, \dots, G_g^{N_g}\} \quad (3.36)$$

Rather than giving the occupancies of separate orbitals as in a conventional electron configuration, a macroconfiguration specifies occupation numbers of fixed groups. Here the user is able to choose both the number of groups and which orbitals are in each group. The user is also able to specify which occupancies they would like to consider in each group. In MCSCF-type schemes, when based on macroconfiguration descriptions of configuration spaces, the adequate treatment of non-dynamic electron correlation effects for all states considered can be accomplished.

Whether the macroconfiguration approach is used or not, the main drawback of the MCSCF method is still present, since it is inherent in the method. This drawback is that MCSCF is only able to account for non-dynamic electron correlation. However, in order to accurately and effectively characterize the species studied in the work presented in this thesis, dynamic electron correlation must be accounted for. This can be done very effectively and efficiently through the use of GVVPT2 which is described below.

3.2.4 Second-Order Generalized Van Vleck Perturbation Theory

Second-Order Generalized Van Vleck Perturbation Theory (GVVPT2) is a multi-configurational perturbative method developed by Dr. Hoffmanns group.^{177–179} In GVVPT2 the MCSCF wavefunction, which is only able to account for non-dynamic electron correlation, can be used as the zeroth-order wavefunction. Then, through a perturbative treatment it can add dynamic electron correlation to the MCSCF wavefunction while still accounting for the non-dynamic electron correlation. Besides GVVPT2, dynamic electron correlation can be added onto the MCSCF wavefunction by other methods as well. The Multi-reference Configuration Interaction including Single and Double excitations (MRCISD) method is one

such method and is known to be highly accurate.¹⁸⁹ However, MRCISD scales as approximately N^6 , where N is the number of basis functions (i.e., a calculation twice as large takes 64 times longer to complete).¹⁸⁹ Thus, it is considered computationally expensive and is typically only used on relatively small systems, e.g., composed of three to four atoms when a potential energy surface is needed.

GVVPT2 is a type of multi-reference perturbation theory (MRPT) or quasidegenerate perturbation theory (QDPT). These methods are significantly more computationally efficient since they scale as approximately N^5 (i.e., a calculation twice as large takes 32 times longer to complete). However, these methods too have drawbacks, most notably by what is known as the “intruder state” problem. This problem occurs when the energy of an excited configuration is comparable to that of the zeroth-order wavefunction. This results in a denominator of the perturbative correction having a value close to zero, thus causing a highly divergent behavior in the potential energy curve. Because of this “intruder state” problem and the complexity of their removal, the general applicability of MRPT and QDPT methods have been limited.

GVVPT2, however, is able to generate smooth potential energy surfaces, similar to the MRCISD method, while still retaining the scalability of MRPT and QDPT (i.e., as approximately N^5). GVVPT2 is considered to be of the “perturb-then-diagonalize” variant of multireference perturbation theory and it is an intermediate Hamiltonian variant of QDPT, making it a subspace selective method. It is worth noting that intermediate Hamiltonians have been shown to be a useful framework in a variety of both multireference (or quasidegenerate) perturbation and coupled cluster theories,^{198–206} and they are seeing continued use and development.

In GVVPT2, a configuration space, L , that is used to describe the states of interest contains an expansion of the set of target wavefunctions,

$$|\Psi_P\rangle = |\psi_1, \psi_2, \dots, \psi_{N_P}\rangle \quad (3.37)$$

where N_P is the number of the low-lying electronic states of interest. The reference space, L , is partitioned into two subspaces: (i) the model space, L_M , and (ii) the external space, L_Q . The model space, L_M (where the dimension of $L_M > N_P$), is usually of the MCSCF-type (i.e., it generally coincides with the MCSCF space). It describes, semi-quantitatively, the most important configurations needed to describe the state(s) of interest and is further divided into two subspaces: (i) the primary subspace, L_P , and (ii) the secondary subspace, L_S .

The primary subspace is composed of a small set of reference functions (e.g., one or more MCSCF CI vectors or MCSCF wave functions), $\{\Phi_P\}_{P=1}^{N_P}$, which involve internal (doubly occupied core plus active) orbitals and are used to generate the L_M space. The secondary subspace, L_S , is the orthogonal complement to L_P in the model space, so

$$L_M = L_P \oplus L_S \quad (3.38)$$

The external space, L_Q , is composed of electron configurations that are connected to and obtained from the model space, L_M , through single and double electron excitations. In order to generate external configurations that can be expected to have only a perturbative effect on the lowest MCSCF states of interest, they need to be energetically well separated, which requires a physically reasonable MCSCF model space. It is also worth noting that

the possible problem of quasidegeneracy between the secondary subspace, L_S , and the external subspace, L_Q , is completely avoided in the GVVPT2 method.^{207–209} The way in which the GVVPT2 method takes into account the interactions of the perturbed primary states in L_P with the unperturbed secondary states in L_S is by a final diagonalization of the effective Hamiltonian, \mathbf{H}^{eff} , (which is the same size as the MCSCF matrix) over the entire model space, L_M . This allows for the effects of dynamic electron correlation on the non-dynamic electron correlation part. A graphical representation of this process, in which the Hamiltonian matrix is shown as a box divided up into its various parts, is given in Figures 3.3a and 3.3b.

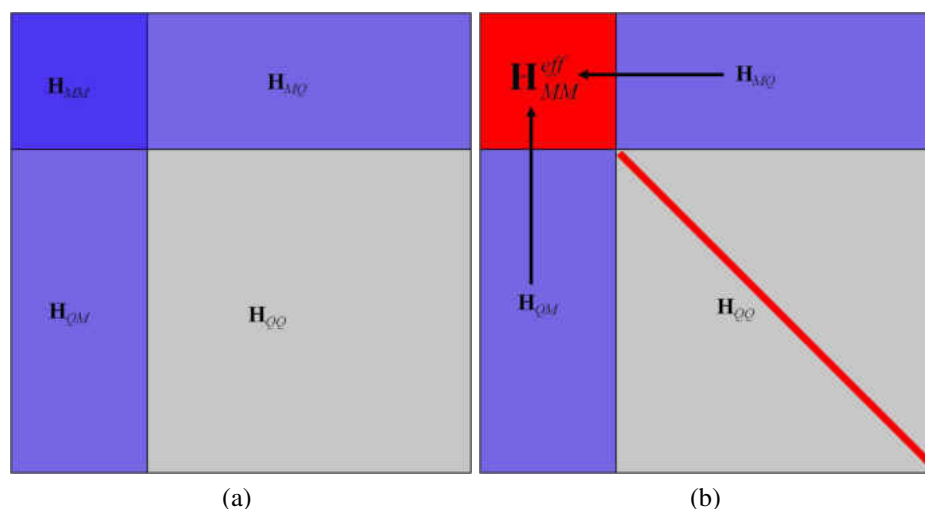


Figure 3.3. The Hamiltonian matrix represented as a box. (a) The \mathbf{H}_{MM} matrix has a small number of electron configurations and neglects dynamic correlation while the full H matrix has a large number of configurations and includes dynamic correlation. (b) By a final diagonalization, dynamic electron correlation is included into \mathbf{H}_{MM}^{eff} by the contributions from \mathbf{H}_{QM} and \mathbf{H}_{MQ} while only the diagonal elements of \mathbf{H}_{QQ} are kept.

To be more specific on the workings of the GVVPT2 method, consider a more general construction of an intermediate Hamiltonian in which the P-Q interactions are taken into account to the first-order in the system's wavefunction using a non-diagonal variant

of QDPT²⁰⁸ where the block-diagonal part of the Hamiltonian matrix in the L_M space is considered as the unperturbed Hamiltonian, given by

$$H_0 = PHP + QHQ \quad (3.39)$$

and the off-diagonal block is considered as the perturbation, given by

$$V = PHQ + QHP \quad (3.40)$$

Then the expressions for the second-order perturbatively corrected Hamiltonian matrix, i.e., the effective Hamiltonian matrix, \mathbf{H}_{MM}^{eff} , is given in the model space L_M as

$$\mathbf{H}_{PP}^{eff} = \mathbf{H}_{PP} + \frac{1}{2} (\mathbf{H}_{PQ} \mathbf{X}_{QP} + \mathbf{X}_{QP}^\dagger \mathbf{H}_{QP}), \quad (3.41)$$

$$\mathbf{H}_{SP}^{eff} = \mathbf{H}_{SQ} \mathbf{X}_{QP}, \quad (3.42)$$

$$\mathbf{H}_{SS}^{eff} = \mathbf{H}_{SS}. \quad (3.43)$$

In the above equations, the elements of the anti-hermitian matrix, \mathbf{X}_{QP} , (i.e., the P-Q rotational parameters) determine the contributions from the external CSFs to the final wavefunction. The P-Q rotation parameters satisfy the system of linear equations

$$(\mathbf{H}_{QQ} - E_0^P) \mathbf{X}_{QP} = -\mathbf{H}_{QP} \quad (3.44)$$

where $P \in [1, N_P]$ (i.e., P a member of the primary space), and $\{E_0^P = \langle \Phi_P | H | \Phi_P \rangle\}_{P=1}^{N_P}$ are the corresponding energies of the reference states, i.e., the MCSCF energies within the L_M space. However, in GVVPT2, the above second-order QDPT basic equations are approximated further, since they are block-diagonal and scale approximately as N^6 . In so-defined QDPT methods, the effects of the secondary states in L_S on the perturbed primary states in L_P is allowed by $\mathbf{H}_{SP}^{eff} = \mathbf{H}_{SQ} \mathbf{X}_{QP}$. This is not the case in several other widely used multi-reference second-order perturbation methods, e.g., MRPT2,²¹⁰ CASPT2²¹¹ and MCQDPT.²¹² It has been shown that these effects can be important, though they are usually small.¹⁷⁷

In the GVVPT2 method, as mentioned above and shown in Figure 3.3b, the off-diagonal matrix elements of the \mathbf{H}_{QQ} matrix are discarded. The required diagonal elements, $H_{qq} - E_0^P$ of the matrices $(\mathbf{H}_{QQ} - E_0^P)$ are also approximated.^{213,214} This can be done with conventional, Møller-Plesset-type, one-electron Hamiltonians,

$$(\mathbf{H}_{qq} - E_0^P) \approx \varepsilon_q^P - \varepsilon_0^P. \quad (3.45)$$

In many cases, this approximation works well; however, in some cases the above mentioned "intruder states" problem would occur, where the difference $\varepsilon_q^P - \varepsilon_0^P$ would be small and in some cases, even negative. This issue was overcome in GVVPT2;¹⁷⁷ "intruder state" are no longer a problem and smooth potential energy surfaces (PES) can be obtained even when two surfaces are quite close to one another. This was accomplished through the use of what could be called stabilized perturbation theory where the rotational parameter, \mathbf{X}_{qp} , can be calculated by

$$X_{qp} = -\frac{\tanh(\varepsilon_{\mathbf{m}_e}^p - \tilde{E}_{0,\mathbf{m}_e}^p)}{\varepsilon_{\mathbf{m}_e}^p - \tilde{E}_{0,\mathbf{m}_e}^p} H_{qp} \quad (3.46)$$

where $\tilde{E}_{0,\mathbf{m}_e}^p$ is the degeneracy-corrected zero-order energy of the p th primary state and \mathbf{m}_e represents a given external configuration. Thus, all external CSFs that are created by a given external configuration, \mathbf{m}_e (which possesses degenerate energy $\varepsilon_{\mathbf{m}_e}^p$), are considered simultaneously. More specifically, $\tilde{E}_{0,\mathbf{m}_e}^p$ is given by

$$\tilde{E}_{0,\mathbf{m}_e}^p = \frac{1}{2}(\varepsilon_{\mathbf{m}_e}^p - \varepsilon_0^p) - \frac{1}{2}\sqrt{(\varepsilon_{\mathbf{m}_e}^p - \varepsilon_0^p)^2 + 4\sum_{q\in\mathbf{m}_e} H_{qp}^2}. \quad (3.47)$$

These new X_{qp} parameters are continuous for all regions of the PES regardless of how small the difference $\varepsilon_q^p - \varepsilon_0^p$ becomes. It is worth noting that where $\varepsilon_{\mathbf{m}_e}^p \gg \varepsilon_0^p$, eqs 3.46 and 3.47 reduce to the same result as the original theory (eq 3.45), yet where $\varepsilon_{\mathbf{m}_e}^p \leq \varepsilon_0^p$, eqs 3.46 and 3.47 give small finite rotation parameters and small negative contributions of the “intruder states” to the correction energy of a given primary state. Thus, the “intruder state” problem is not an issue with GVVPT2, while it still possesses a lower computational cost than MRCISD with a scaling of approximately N^5 . This gives GVVPT2 excellent prospects and it is particularly useful for complicated chemical systems. GVVPT2 can give information on the energies and the occupancies of the MOs and the multi-reference character of the systems studied while costing significantly less than other methods of comparable accuracy. Thus GVVPT2 was a natural choice for the work presented in this thesis.

Its important to note that GVVPT2 is sensitive to the user-specified active space, so a reasonably accurate, chemically intuitive description is required. GVVPT2 does not have

any restrictions on the model space that can be used and both complete and incomplete model spaces are supported. GVVPT2 does not vary with the choice of many-electron functions, e.g., configuration state functions (CSFs), within each subspace. The construction of a well balanced model space is known to be the main challenge when using multi-reference methods like GVVPT2. Fortunately, the macroconfiguration approach, developed by Prof. Hoffmann's group,¹⁹⁷ is available and it can provide significant aid in this challenge.

In GVVPT2, as well as in other similar multi-reference methods, the use of the macroconfiguration approach enables: (i) the use of chemical intuition in constructing compact model spaces and in generating external spaces; (ii) the elimination of the need to store large lists of external configurations and the desired subsets of such configurations can be efficiently regenerated during the calculation; and (iii) the potentially drastic decrease of the number of configuration pairs that must be explicitly calculated, because of the screening of the effective Hamiltonian matrix blocks corresponding to non-interacting macroconfiguration pairs. Therefore, the macroconfiguration approach was used in the construction of the active spaces used in GVVPT2 which are given below, along with the obtained results.

3.3 RESULTS

3.3.1 Computational Details

Due to size restrictions, GVVPT2 calculations on the dimeric selenium and arsenic oxides were of the MCSCF incomplete active space variety. More specifically, the active spaces were spanned by all CSFs that could be obtained from distributing all electrons in one orbital group (G_1), all but 1 electron in G_1 (with one electron in a second orbital group,

G_2), and all but 2 electrons in G_1 (with 2 electrons in G_2). The efficacy of this active space for reactive oxygen-rich systems has been recently demonstrated.²¹⁹ The effectiveness of this type of model space for the compounds studied was also assessed by comparing results obtained using them, denoted MCSD, with CASSCF-based GVVPT2 results. In the GVVPT2 study presented in this thesis, single and double excitations from all macroconfigurations used to describe the model space were used. Also, excitations were allowed from the highest-lying doubly occupied orbitals.

The active orbitals for both the selenium and arsenic dimeric oxides were divided into two subgroups in accordance with the above mentioned MCSD spaces. Concerning the dimeric selenium oxides, the calculations of the isomers and transition states of Se_2O_3 used 17 active orbitals (i.e., the 2p of O, and the 4s and 4p of Se) which contained 24 electrons (24e, 17o) that were distributed as $G_1 = (27-34a' 9-12a'')$, in C_s symmetry, or simply 35-46a in C_1 symmetry) and $G_2 = (35-39a' 13a'')$. In the GVVPT2 treatment, the oxygen 2s dominated molecular orbitals were also correlated. The energy calculations of the isomers and transition states of Se_2O_5 used 23 active orbitals (i.e., the 2p of O, and the 4s and 4p of Se) containing 32 electrons (32e, 23o) that were distributed as $G_1 = (29-38a' 11-16a'')$, C_s) and $G_2 = (39-43a' 17-18a'')$. Again, in the GVVPT2 treatment, the oxygen 2s dominated molecular orbitals were correlated, which introduced 5 additional orbitals into the GVVPT2 occupied space (25-28a' 10a''), C_s).

Concerning the dimeric arsenic oxides, the energy calculations of the isomers and transition states of As_2O_3 used 20 active orbitals (i.e., the 2s and 2p of O, and the 4s and 4p of As) which contained 28 electrons (28e, 20o) that were distributed as $G_1 = (13-18a_1 5a_2 6-9b_1 11-13b_2)$, in C_{2v} symmetry for isomer 1, 23-31a' 10-14a''), in C_s symmetry for isomer 2,

or simply 32-45a in C_1 symmetry) and $G_2 = (19-20a_1 6a_2 10b_1 14-15b_2, \text{ in } C_{2v} \text{ symmetry, } 32-35a' 15-16a'', \text{ in } C_s \text{ symmetry, or simply } 46-51a \text{ in } C_1 \text{ symmetry})$. For isomer 4 of As_2O_3 , the MCSCF calculation used 17 active orbitals (i.e., the 2p of O, and the 4s and 4p of As) which contained 22 electrons (22e, 17o) that were distributed as $G_1 = (27-33a' 9-12a'')$ and $G_2 = (34-38a' 13a'')$, while in the GVVPT2 treatment, the oxygen 2s dominated molecular orbitals were correlated which introduced 3 additional orbitals into the GVVPT2 occupied space (24-26a'', in C_s symmetry). The single point energy calculations of the isomers and transition states of As_2O_5 used 28 active orbitals (i.e., the 2s and 2p of O, and the 4s and 4p of As) containing 40 electrons (40e, 28o) that were distributed as $G_1 = (14-21a_1 5-6a_2 6-10b_1 12-16b_2, \text{ in } C_{2v} \text{ symmetry for isomer 1, } 18-25a_1 3-4a_2 8-12b_1 8-12b_2, \text{ in } C_{2v} \text{ symmetry for isomer 3, } 25-37a' 10-16a'', \text{ in } C_s \text{ symmetry or simply } 34-53a \text{ in } C_1 \text{ symmetry})$ and $G_2 = (22-24a_1 7a_2 11b_1 17-19b_2, \text{ in } C_{2v} \text{ symmetry for isomer 1, } 26-29a_1 13-14b_1 13-14b_2, \text{ in } C_{2v} \text{ symmetry for isomer 3, } 38-43a' 17-18a'', \text{ in } C_s \text{ symmetry or simply } 54-61a \text{ in } C_1 \text{ symmetry})$. For isomer 6 of As_2O_5 , the MCSCF calculation used 17 active orbitals (i.e., the 2p of O, and the 4s and 4p of As) which contained 30 electrons (30e, 23o) that were distributed as $G_1 = (29-38a' 11-15a'')$ and $G_2 = (39-43a' 16-18a'')$, while in the GVVPT2 treatment, the oxygen 2s dominated molecular orbitals were correlated which introduced 5 additional orbitals into the GVVPT2 occupied space (25-28a' 10a'', in C_s symmetry).

The work that I personally conducted included the methods: RHF, RMP2, MCSCF, and GVVPT2 (GUGA-based) calculations, performed through the use of a local software package referred to as UNDMOL.¹⁷⁹ I also performed several calculations using the rigorously size extensive variant of completely renormalized couple cluster with single and

double excitations along with non-iterative triples, namely, CR-CC(2,3), through the use of the GAMESS US program.^{216,217} However, several other calculations relevant to this thesis are included in the results that were performed by other group members. Both nonrelativistic and 2nd order Douglas-Kroll-Hess (DKH) scalar relativistic CR-CC(2,3) calculations were performed using the GAMESS US program. B3LYP calculations were performed using UNDMOL, GAMESS US, and the Gaussian 03 program.¹⁸⁸ Concerning the basis sets used, 6-311G* was used for B3LYP calculations while cc-pVDZ and cc-pVTZ were used for all of the RMP2, MCSCF, GVVPT2 and CR-CC(2,3) calculations.

3.3.2 Validation of the Computational Protocol

As mentioned above, the computational protocol, which was used to identify and characterize the multiple stationary points of the Se_2O_3 and Se_2O_5 PES's, was tested on the monomeric selenium oxides, SeO , SeO_2 and SeO_3 . The results were then compared to experimental data as well as the more computationally expensive protocol used in the study of the monomers.²¹⁸ A new protocol had to be developed for the dimeric oxides, since they are considerably more expensive to study (e.g., the geometry optimization of Se_2O_5 needed 14 *quadrillion* CSFs to be described in C_s symmetry, which is not computationally feasible for all isomers). The CASSCF that was used on the monomers were reduced to an incomplete model space which consisted in single- and double-excitations from a HF-like reference macroconfiguration, as described above. This change did not have any significant change on the GVVPT2-predicted geometrical parameters, which agreed well experimental values. Also, the calculation of the heats of oxidation reactions were reproduced to within about 2 kcal/mol accuracy. However, when comparing results obtained from the use of a

double split one-electron basis set to the triple split valence basis set there was significant deviation from the experimental values for the geometrical parameters and especially for the reaction energies.²¹⁸

To efficiently identify the isomers and transition states of As_2O_3 , As_2O_5 , Se_2O_3 and Se_2O_5 , the accuracy of B3LYP/6-311G* was tested on the monomers. It was found that the geometrical parameters were in close agreement with the values found using GVVPT2/cc-pVTZ. This was found especially true for the SeO_2 and SeO_3 monomers (deviations of only 0.001 and 0.007 Å, respectively), which is important since the bonding motifs of the dimers are similar to that of SeO_2 and SeO_3 . However, the reaction energies for B3LYP/6-311G* significantly deviated from experiment (ca. 17 kcal/mol error in one case) while GVVPT2/cc-pVTZ agreed quite well (ca. 2 kcal/mol in error for the same reaction).

Therefore, the geometry optimizations were calculated using B3LYP/6-311G* and the relative energies were calculated using the GVVPT2/cc-pVTZ level along with CR-CC(2,3)/cc-pVTZ for the purposes of corroboration. In an earlier published study, an approach similar to this, where GVVPT2 was used to calculate the energies of several optimized geometries (which included transition states) obtained through the use of B3LYP, showed good agreement with a well-calibrated and widely used composite method, i.e., CBS-QB3.²¹⁹ To assess the suitability of B3LYP/6-311G* for the optimization of the dimers presented in this thesis, one isomer each of Se_2O_3 and Se_2O_5 was optimized at the GVVPT2/cc-pVTZ level and the parameters compared to the parameters obtained from B3LYP/6-311G*, the results of which are presented below in Sections 3.3.3 and 3.3.4, along with all the relevant data obtained for Se_2O_3 and Se_2O_5 , respectively. The results of the calculations concerning As_2O_3 and As_2O_5 are given below in Sections 3.3.5 and 3.3.6, respectively.

3.3.3 Se₂O₃

Concerning the diselenium trioxide (Se₂O₃) molecule, there were a total of four minima (i.e., isomer 1, 2, 3 and 4) and three transition states (i.e., TS13, TS23 and TS24) found. An example of an isomer (i.e., isomer 1), along with the numbering system used for the presentation of the geometrical parameters is given in Figure 3.4. The optimized geometrical parameters, which were obtained through the B3LYP/6-311G* calculations performed by Dr. Zhenhua Chen are given in Table 3.1.

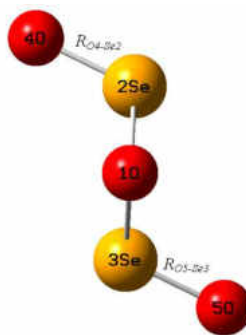


Figure 3.4. Structure of isomer 1 of diselenium trioxide (Se₂O₃).²¹⁸

Isomer 1 was predicted to be a structure possessing C₂ symmetry and consists of a three-membered ring backbone and terminal oxygens trans to each other. Isomer 2 was found to be a planar structure with C_s symmetry. Isomer 3 was predicted to be a non-planar structure with C_s symmetry. Isomer 4 was found to be a planar structure which possessed C_{2v} symmetry. Each of the transition states were predicted to be of the C₁ point group.

Every isomer found showed significant asymmetry in $r_e(\text{Se-O})$. When comparing the geometrical parameters for Se₂O₃ to that of the monomers, it was found that the long Se-O bonds in the equilibrium structures of Se₂O₃ (i.e., 1.806 – 1.884 Å) were significantly longer than the $r_e(\text{Se-O})$ bond lengths in SeO, SeO₂ and SeO₃.²¹⁸ However, the short Se-O

Table 3.1. Optimized B3LYP/6-311G* geometrical parameters (Å and degrees) of the diselenium trioxide (Se₂O₃) isomers and transition states.²¹⁸

	Isomer 1	Isomer 2	Isomer 3	Isomer 4	TS13	TS23	TS24
Parameters	(C ₂)	(C _s)	(C _s)	(C _{2v})	(C ₁)	(C ₁)	(C ₁)
R _{(O1)-(Se2)}	1.879	1.806	1.884	1.820	2.720	1.875	1.869
R _{(O4)-(Se2)}	1.627	1.658	1.626	1.633	1.638	1.641	1.640
R _{(O1)-(Se3)}	1.879	1.850	1.884	1.820	1.656	1.839	1.871
R _{(O5)-(Se3)}	1.627	1.631	1.626	1.633	1.649	1.632	1.634
∠ (O5)(Se3)(O1)	109.0	103.6	110.0	112.4	109.8	106.8	110.8
∠ (Se3)(O1)(Se2)	86.2	116.5	85.8	139.7	71.9	113.3	112.6
∠ (O1)(Se2)(O4)	109.0	99.6	110.0	112.4	151.9	111.9	110.9

bonds (i.e., 1.626 – 1.633 Å) are longer than the $r_e(\text{Se-O})$ bond length in SeO₂ (i.e., 1.622 Å) and SeO₃ (i.e., 1.614 Å) while being shorter than the $r_e(\text{Se-O})$ bond length in SeO (i.e., 1.656 Å).²¹⁸ The bond angles of Se₂O₃ were found to be smaller than the bond angles of both SeO₂ and SeO₃ by ca. 5–10°. It is worth noting that since the bond length and angles of the found isomers of Se₂O₃ are quite similar, isomerization can be expected.

As mentioned above, the results of a full geometry optimization at the GVVPT2/cc-pVTZ level were compared to that of the results obtained through B3LYP/6-311G* for isomer 1. The GVVPT2 calculation confirmed both isomer 1's C₂ symmetry and the general structural characteristics. However, there were deviations from the specific values of the geometry. For example, the short Se–O bonds (i.e., between a selenium and its terminal oxygen) decreased by 0.022 Å and the long Se–O bonds (i.e., between a selenium and the apex oxygen) decreased by 0.021 Å; the angle about the apex oxygen expanded from 86.2° to 87.6°. Though there were the differences noted in these geometrical parameters, i.e., using the B3LYP/6-311G* optimized geometry for isomer 1 for the GVVPT2 energy calculation rather than the GVVPT2/cc-pVTZ optimized geometry, an error of only 0.3

kcal/mol occurred. Thus, the B3LYP/6-311G* optimized geometries of the dimeric trioxides were validated for the purposes of this study.²¹⁸

The relative energies found for each level of theory and with each basis set used is given in Table 3.2. Also, for a qualitative visual aid, the relative energies are plotted for both the cc-pVTZ and cc-pVDZ basis sets and are given in Figures 3.5 and 3.6, respectively. It can be seen that regardless of the level of theory or which basis set was used, isomer 1 was predicted to be the most stable, with the only exception being GVVPT2/cc-pVDZ. Similar anomalies were observed with the monomers when a basis set was used that was too small.²¹⁸ This again confirmed the need for an adequately large basis set in the study of these dimeric oxides.

Table 3.2. Relative energies (kcal/mol) of the diselenium trioxide (Se₂O₃) isomers and transition states.²¹⁸

		B3LYP (6-311G*)	CR-CC(2,3) (cc-pVDZ)	CR-CC(2,3) (cc-pVTZ)	GVVPT2 (cc-pVDZ)	GVVPT2 (cc-pVTZ)
Isomer 4	C _{2v}	9.7	5.4	12.3	-0.3	6.3
TS24	C ₁	21.2	-	-	6.7	13.2
Isomer 2	C _s	9.1	4.1	9.3	0.4	5.8
TS23	C ₁	18.0	7.2	12.3	5.2	11.2
Isomer 3	C _s	2.7	2.6	2.2	2.0	1.4
TS13	C ₁	30.0	28.3	30.9	33.6	36.8
Isomer 1	C ₂	0.0	0.0	0.0	0.0	0.0

Concerning the comparison between the single point energy calculations using GVVPT2/cc-pVTZ and CR-CC(2,3)/cc-pVTZ, both methods found the same general ordering. They predicted that isomer 1 was followed by isomer 3 with energies at 1.4 kcal/mol above isomer 1 for GVVPT2 and 2.2 kcal/mol for CR-CC(2,3). Isomer 2 was found to be the next most stable with relative energies of 5.8 and 9.3 kcal/mol for GVVPT2 and CR-CC(2,3),

respectively, and isomer 4 was predicted to be the least stable at 6.3 and 12.3 kcal/mol, respectively. This good agreement between GVVPT2 and CR-CC(2,3) was also observed for the monomers. This is due to characteristics of the wavefunctions. For example, isomer 1 has a single largest amplitude of 0.933 while the next contribution is -0.123, so that its wavefunction is similar to the wavefunction predicted for SeO_2 (i.e., 0.931 and -0.176).

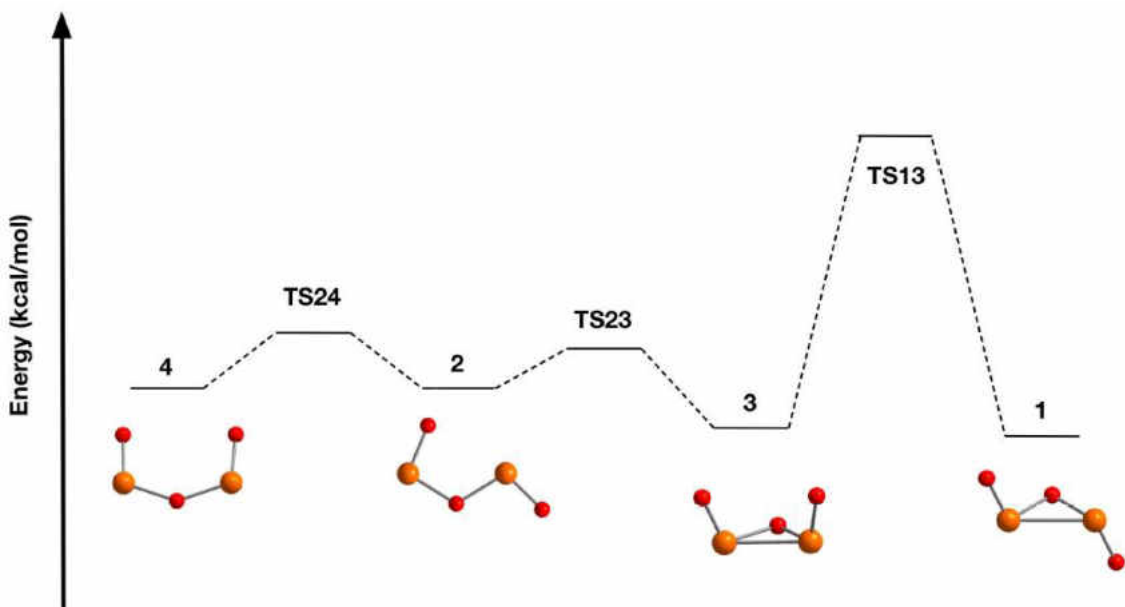


Figure 3.5. Relative GVVPT2/cc-pVTZ energies of diselenium trioxide (Se_2O_3) isomers and transition states (in kcal/mol).²¹⁸

Figure 3.6 shows the relative energies predicted using the GVVPT2 level of theory with the cc-pVDZ basis set. As mentioned above, isomer 4 was mistakenly predicted to be the most stable isomer at -0.3 kcal/mol lower than isomer 1. Isomer 2 was found to be nearly isoenergetic with isomer 4 and isomer 1, with an energy only 0.4 kcal/mol greater than isomer 1. Isomer 3 was predicted to be the least stable and even so had an energy only 2.0 kcal/mol more than isomer 1.

The barrier heights between isomers 1 and 3, isomers 3 and 2, and isomers 2 and 4 were

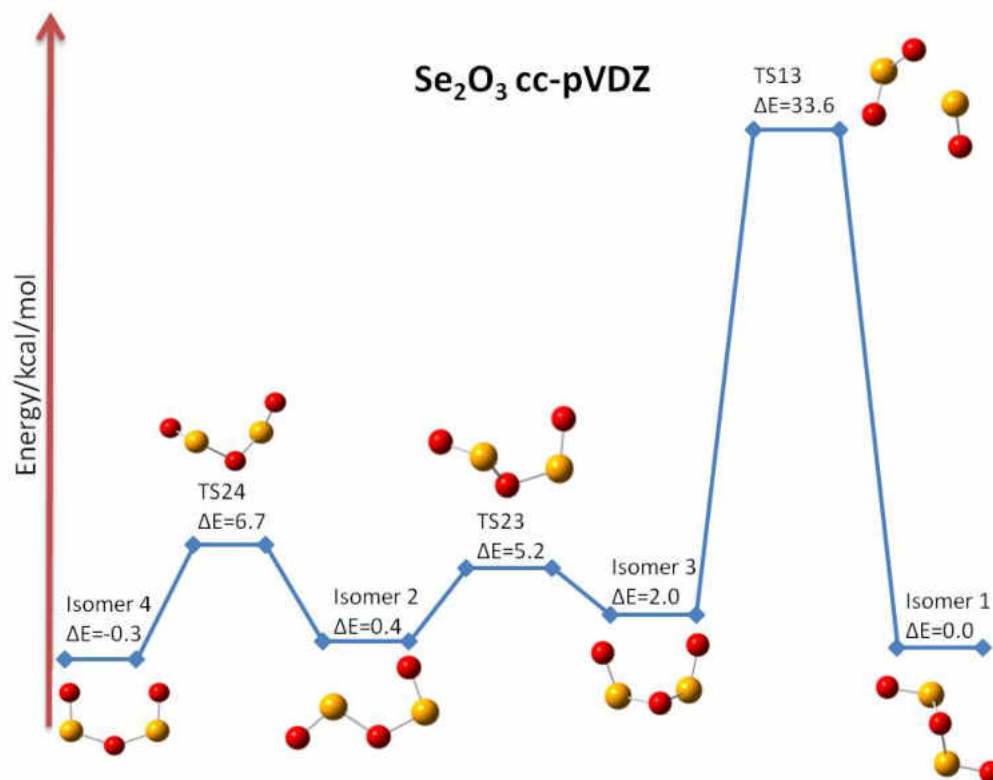


Figure 3.6. Relative GVVPT2/cc-pVDZ energies of diselenium trioxide (Se₂O₃) isomers and transition states (in kcal/mol).²¹⁸

predicted by GVVPT2/cc-pVTZ to be at 36.8, 11.2 and 13.2 kcal/mol, respectively. Using CR-CC(2,3)/cc-pVTZ, the barrier heights were found to be 30.9 kcal/mol for TS13 and 12.3 kcal/mol for TS23. However, the barrier height of TS24 proved difficult to predict, and the CR-CC(2,3) calculations failed to converge for both basis sets (i.e., cc-pVDZ and cc-pVTZ). Interestingly, in sharp contrast to TS23, the predictions for TS13 made at all levels of theory and with all basis sets are in essential agreement.

In Table 3.3, the total energies (in atomic units) of SeO, SeO₂ and isomer 1 of Se₂O₃ are given along with the reaction energies (in kcal/mol) predicted by B3LYP/6-311G*, GVVPT2/cc-pVTZ and CR-CC(2,3)/cc-pVTZ concerning the reaction of the monomeric

oxides to form Se_2O_3 ,



The reaction energies calculated by GVVPT2 and CR-CC(2,3) are in near perfect agreement (ca. 0.1 kcal/mol). Because of the excellent agreement of GVVPT2 and CR-CC(2,3) with experiment for the prediction of the oxidation energies of Se to the monomers and their general agreement for the relative energy calculations, it can be concluded that the reaction given in eq 3.48 is slightly exothermic. When the change in the zero point energy is included in the reaction, the product is destabilized by 1.0 kcal/mol, yet the reaction remains slightly exothermic.

Table 3.3. Total energies (a.u.) of SeO, SeO₂ and Se₂O₃ (isomer 1), and predicted reaction energy (kcal/mol) where both GVVPT2 and CR-CC(2,3) used the optimized B3LYP/6-311G* geometries.²¹⁸

	SeO	SeO ₂	Se ₂ O ₃ (1)	ΔE
B3LYP/6-311G*	-2476.730 645	-2551.954 559	-5028.689 640	-2.8
GVVPT2/cc pVTZ	-2475.108 097	-2550.227 732	-5025.347 576	-7.4
CR-CC(2,3)/cc pVTZ	-2475.124 653	-2550.249 035	-5025.385 695	-7.5

3.3.4 Se₂O₅

There were a total of six minima (i.e., isomer 1, 2, 3, 4, 5 and 6) and three transition states (i.e., TS12, TS23, TS34, TS35 and TS56) found for the diselenium pentoxide (Se₂O₅) molecule. An example of a structure (i.e., TS12), along with the numbering system used for the presentation of the geometrical parameters is given in Figure 3.7. The optimized geometrical parameters, which were obtained through the B3LYP/6-311G* calculations

performed by Dr. Zhenhua Chen, are given in Tables 3.4 and 3.5 for the isomers and transition states, respectively.

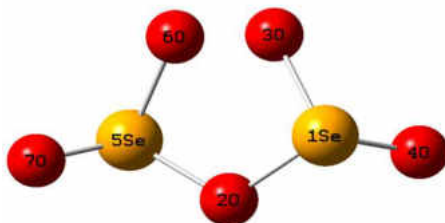


Figure 3.7. Structure of TS12 of diselenium pentoxide (Se_2O_5).²¹⁸

Isomer 1 and isomer 2 were predicted to possess C_2 symmetry. Isomer 3, isomer 4 and isomer 5 were found to have C_s symmetry. Isomer 6 was predicted to be a non-planar structure with C_s symmetry. Isomer 6, along with TS23, TS34, TS35 and TS56 were predicted to be of the C_1 point group. TS12 was predicted to possess C_2 symmetry. Isomers 1, 2 and 4 were found to be ring structures.

Table 3.4. Optimized B3LYP/6-311G* geometrical parameters (\AA and degrees) of the diselenium pentoxide (Se_2O_5) isomers.²¹⁸

Parameters	Isomer 1 (C_2)	2 (C_2)	3 (C_s)	4 (C_s)	5 (C_s)	6 (C_1)
$R_{(O4)-(Se1)}$	1.606	1.607	1.612	1.828	1.614	1.605
$R_{(O3)-(Se1)}$	1.924	1.911	1.649	1.602	1.614	1.924
$R_{(O2)-(Se1)}$	1.858	1.845	-	1.604	1.612	1.867
$R_{(O2)-(Se5)}$	1.858	1.845	1.624	-	-	1.847
$R_{(O6)-(Se5)}$	1.924	1.911	1.610	1.897	1.637	1.918
$R_{(O7)-(Se5)}$	1.606	1.607	1.610	1.560	1.612	1.606
$\angle (O4)(Se1)(O3)$	101.9	109.4	111.4	111.1	119.8	101.9
$\angle (Se1)(O2)(Se5)$	118.0	118.4	-	110.0	-	117.4
$\angle (O6)(Se5)(O7)$	101.9	109.4	120.9	107.7	114.7	108.9

As observed for Se_2O_3 , the optimized bond lengths fell into two general categories, those with short bond lengths and those with long bond lengths. When comparing the

Table 3.5. Optimized B3LYP/6-311G* geometrical parameters (Å and degrees) of the diselenium pentoxide (Se₂O₅) transition states.²¹⁸

	TS12	TS23	TS34	TS35	TS56
Parameters	(C ₂)	(C ₁)	(C ₁)	(C ₁)	(C ₁)
R _{(O4)-(Se1)}	1.606	1.654	1.647	1.634	1.660
R _{(O3)-(Se1)}	1.899	1.721	1.607	1.614	1.622
R _{(O2)-(Se1)}	1.842	1.622	1.609	-	1.724
R _{(O2)-(Se5)}	1.842	-	-	1.617	-
R _{(O6)-(Se5)}	1.899	1.671	1.676	1.611	1.674
R _{(O7)-(Se5)}	1.606	1.612	1.610	1.611	1.614
∠ (O4)(Se1)(O3)	104.8	103.2	118.0	113.9	120.4
∠ (Se1)(O2)(Se5)	122.2	-	-	-	-
∠ (O6)(Se5)(O7)	104.8	115.1	109.6	120.3	114.2

geometrical parameters for Se₂O₅ to that of the monomers, it was found that the long Se–O bonds in the equilibrium structures of Se₂O₅ were significantly longer than the $r_e(\text{Se–O})$ bond lengths in SeO (i.e., 0.172 – 0.268 Å longer), SeO₂ (i.e., 0.206 – 0.302 Å longer), and SeO₃ (i.e., 0.214 – 0.310 Å longer).²¹⁸ The short Se–O bonds were all about 0.044 – 0.054 Å shorter than the bond length of SeO, 0.010 – 0.020 Å shorter than in SeO₂, and 0.002 – 0.012 Å shorter than in SeO₃, except one particularly short Se–O bond. This was predicted in the isomer 4 (i.e., the most stable isomer), which has the shortest bond length (1.560 Å) observed for any dimeric molecule presented in this thesis. The bond angles of Se₂O₅ are smaller than the bond angles of both SeO₂ and SeO₃ by up to 20° less. The trends observed in the bond lengths and bond angles present in the isomers are observed in the transition states as well. It is worth noting that since the bond lengths and angles of the found isomers of Se₂O₅ are quite similar, as with the Se₂O₃ molecule, isomerization can be expected.

As done for Se₂O₃, the results of a full geometry optimization at the GVVPT2/cc-pVTZ level was compared to the results obtained through B3LYP/6-311G* for isomer 4. The

GVVPT2 calculation confirmed both isomer 4's C_s symmetry and the general structural characteristics. However, there were deviations from the specific values of the geometry. One of the bridging oxygens, which is connected by long Se–O bonds (1.897 and 1.828 Å) to the two seleniums, had a bond length decrease by 0.031 Å (to 1.866 Å) whereas the other Se–O bond changed by less than 0.001 Å. This resulted in the distance between the two seleniums across the ring to change from 2.808 Å to 2.768 Å. Also, one of the short SeO bonds (i.e., between a selenium and its terminal oxygen) decreased from 1.604 Å to 1.598 Å and the angle between the two oxygens outside of the ring contracted by 0.2° to 107.5°. Although there were again the noted differences in these geometrical parameters, using the B3LYP/6-311G* optimized geometry for isomer 1 for the GVVPT2 energy calculation rather than the GVVPT2/cc-pVTZ optimized geometry brought about an error less than 0.7 kcal/mol. Thus, the B3LYP/6-311G* optimized geometries for the dimeric pentoxides were validated for the purposes of this study.²¹⁸

The relative energies found for each level of theory and with each basis set used is given in Table 3.6. Also, for a visual aid, the relative energies are plotted for both the cc-pVDZ and cc-pVTZ basis sets and are given in Figures 3.9 and 3.8. It can be seen that regardless of the level of theory or which basis set was used, isomer 4 was predicted to be the most stable.²¹⁸

Concerning the comparison between the single point energy calculations using GVVPT2/cc-pVTZ and CR-CC(2,3)/cc-pVTZ, as was the case for the isomers of Se_2O_3 , both methods found the same general ordering. They predicted that isomer 4 was followed by isomer 3 with energies at 10.8 kcal/mol above isomer 4 for GVVPT2 and 14.9 kcal/mol for CR-CC(2,3). Next was isomer 5, followed by isomer 2 and isomer 6. Fi-

Table 3.6. Relative energies (kcal/mol) of the diselenium pentoxide (Se_2O_5) isomers and transition states.²¹⁸

		B3LYP	CR-CC(2,3)	CR-CC(2,3)	GVVPT2	GVVPT2
	Symmetry	(6-311G*)	(cc-pVDZ)	(cc-pVTZ)	(cc-pVDZ)	(cc-pVTZ)
Isomer 1	C_2	3.2	9.4	20.7	19.2	31.1
TS12	C_2	8.1	14.2	25.1	23.7	38.5
Isomer 2	C_2	1.7	6.7	18.1	14.7	27.9
TS23	C_1	33.4	37.3	45.5	32.3	39.2
Isomer 3	C_s	11.6	9.0	14.9	5.5	10.8
TS34	C_1	13.3	13.0	17.6	11.6	16.0
Isomer 4	C_s	0.0	0.0	0.0	0.0	0.0
TS35	C_1	13.9	10.8	17.2	7.5	13.3
Isomer 5	C_s	12.7	9.1	16.0	6.2	12.0
TS56	C_1	36.6	40.4	48.7	35.9	42.8
Isomer 6	C_1	3.2	8.5	20.7	16.3	30.0

nally, isomer 1 was predicted to be the least stable minima with the GVVPT2/cc-pVTZ and CR-CC(2,3)/cc-pVTZ relative energies of 31.1 and 20.7 kcal/mol, respectively. As stated earlier, this good agreement between GVVPT2 and CR-CC(2,3) was also observed for the monomers. This is due to the similarities of certain characteristics of the wavefunctions. For example, isomer 1 has a single largest amplitude of 0.933 while the next contribution is -0.123 so that this wavefunction has similar spectral characteristics to the wavefunction predicted for SeO_2 (i.e., 0.931 and -0.176). For isomer 4, the largest wave function amplitude of Se_2O_5 was 0.936, and lies well in the range of leading configurations (e.g., 0.950, SeO ; 0.931, SeO_2 ; 0.919, SeO_3)²¹⁸ in which GVVPT2 results have been observed to agree well with CR-CC(2,3).

Figure 3.8 shows the relative energies predicted using the GVVPT2 level of theory with the cc-pVDZ basis set. Unlike the case for Se_2O_3 , the general ordering of the isomers was preserved. However, CR-CC(2,3)/cc-pVDZ mistakenly predicted isomer 2 to be more sta-

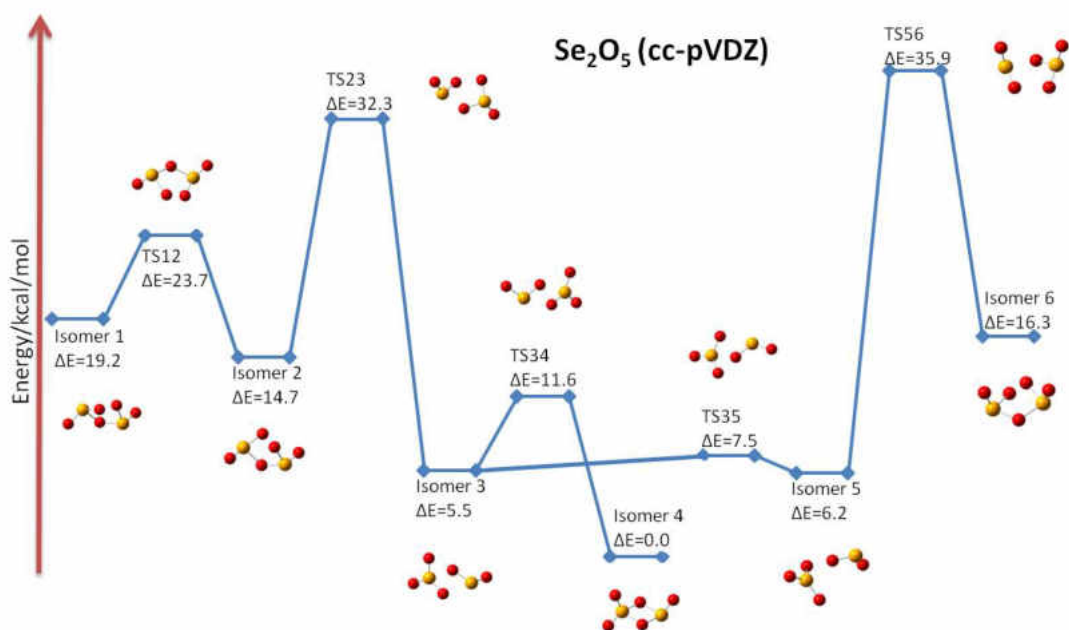


Figure 3.8. Relative GVVPT2/cc-pVDZ energies of diselenium pentoxide (Se_2O_5) isomers and transition states (in kcal/mol).²¹⁸

ble than isomer 3. The B3LYP energy ordering was significantly worse, with the ordering: isomer 4 < isomer 2 < isomer 1 = isomer 6 < isomer 3 < isomer 5.

The barrier heights between isomers 1 and 2, isomers 2 and 3, isomers 3 and 4, isomers 3 and 5, and isomers 5 and 6 were predicted by GVVPT2/cc-pVTZ to be 38.5, 39.2, 16.0, 13.3 and 42.8 kcal/mol, respectively. Using CR-CC(2,3)/cc-pVTZ, the barrier heights were found to be 25.1 kcal/mol for TS13, 45.5 kcal/mol for TS23 and 17.6 kcal/mol for TS34. Using B3LYP/6-311G*, the barrier heights were found to be 8.1 kcal/mol for TS13, 33.4 kcal/mol for TS23, 13.3 kcal/mol for TS34, 13.9 kcal/mol for TS35 and 36.6 kcal/mol for TS56.

As can be seen in Table 3.7, the total energies (in atomic units) of O_2 , SeO_3 and isomer 4 of Se_2O_5 are given along with the reaction energies (in kcal/mol) predicted by B3LYP/6-

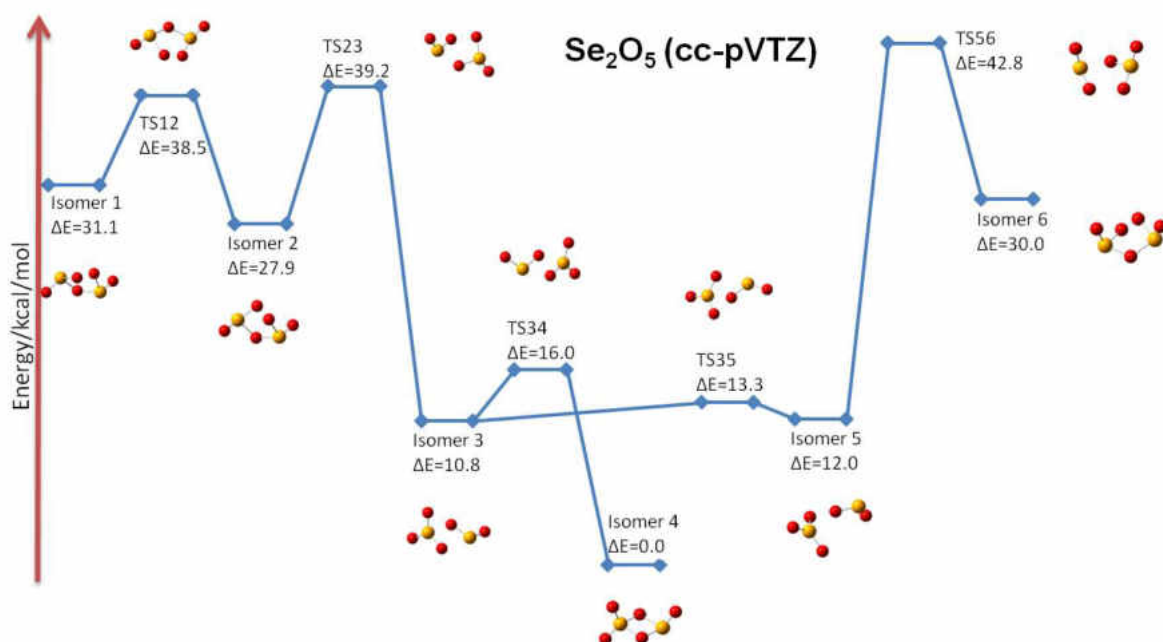


Figure 3.9. Relative GVVPT2/cc-pVTZ energies of diselenium pentoxide (Se₂O₅) isomers and transition states (in kcal/mol).²¹⁸

311G*, GVVPT2/cc-pVTZ and CR-CC(2,3)/cc-pVTZ concerning the stability of the reactants to the formation of Se₂O₅, from the monomers



and from further oxidation of a diselenium oxide,



The reaction energies calculated by B3LYP, CR-CC(2,3) and GVVPT2 all predict that both reactions are exothermic. GVVPT2 and CR-CC(2,3) predict the reaction energies of reaction 1 (given in eq 3.49) to be ca. -20 kcal/mol with an agreement between methods

of 2.5 kcal/mol. They predict the reaction energies of reaction 2 (given in eq 3.50) to be significantly more exothermic with energies of -44.2 and -49.5 kcal/mol, respectively.

B3LYP/6-311G* is in good agreement with the other results for reaction 1, but it is considerably off for reaction 2 in which there is much more of a change in bonding environment. When the change in the zero point energy is included in the reactions, only relatively small changes take place, i.e., the product is destabilized by 1.6 kcal/mol in reaction 1 and by 2.3 kcal/mol in reaction 2.

Table 3.7. Total energies (a.u.) of O₂, SeO₃ and Se₂O₅ (isomer 4), and predicted reaction energy (kcal/mol) where ΔE_{rxn1} refers to (SeO₂ + SeO₃ → Se₂O₅ (4)) and ΔE_{rxn2} refers to (Se₂O₃ (1) + O₂ → Se₂O₅ (4)). Both GVVPT2 and CR-CC(2,3) used the optimized B3LYP/6-311G* geometries.²¹⁸

	O ₂	SeO ₃	Se ₂ O ₅ (4)	ΔE_{rxn1}	ΔE_{rxn2}
B3LYP/6-311G*	-150.360 823	-2627.110 341	-5179.098 678	-21.2	-30.3
GVVPT2/cc pVTZ	-150.118 225	-2625.286 023	-5175.544 687	-19.4	-49.5
CR-CC(2,3)/cc pVTZ	-150.130 032	-2625.302 180	-5175.586 132	-21.9	-44.2

3.3.5 As₂O₃

A total of four minima (i.e., isomer 1, 2, 3 and 4) and three transition states (i.e., TS12, TS23 and TS34) were found for the diarsenic trioxide (As₂O₃) molecule. An example of an isomer (i.e., isomer 4), along with the numbering system used for the presentation of the geometrical parameters is given in Figure 3.10. The optimized geometrical parameters, which were obtained through the B3LYP/6-311G* calculations performed by Dr. Zhenhua Chen, are given in Table 3.8. The applicability of the B3LYP/6-311G* optimized geometries was confirmed for the purposes of this study and is explained above in the preceding section.

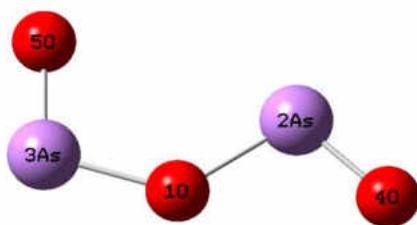


Figure 3.10. Structure of isomer 4 of diarsenic trioxide (As_2O_3).²¹⁸

Isomer 1 was predicted to possess C_{2v} symmetry. Isomer 4 was found to be a planar structure with C_s symmetry. Isomer 2 was predicted to be a non-planar structure with C_s symmetry. Isomer 3 was found to possess C_2 symmetry. Each of the transition states were predicted to be of the C_1 point group. Isomer 1 was found to be a cage structure (i.e., with three bridging oxygens).

Table 3.8. Optimized B3LYP/6-311G* geometrical parameters (\AA and degrees) of the diarsenic trioxide (As_2O_3) isomers and transition states.²²⁰

Parameters	Isomer 1 (C_{2v})	Isomer 2 (C_s)	Isomer 3 (C_2)	Isomer 4 (C_s)	TS12 (C_1)	TS23 (C_1)	TS34 (C_1)
$R_{(O1)-(As2)}$	1.866	1.700	1.819	1.845	1.738	1.770	1.841
$R_{(O4)-(As2)}$	1.866	1.700	1.619	1.617	1.738	1.642	1.616
$R_{(O5)-(As2)}$	1.866	-	-	-	-	-	-
$R_{(O1)-(As3)}$	1.866	2.146	1.819	1.802	2.032	1.894	1.797
$R_{(O4)-(As3)}$	1.866	2.146	-	-	2.032	-	-
$R_{(O5)-(As3)}$	1.866	1.612	1.619	1.671	1.649	1.613	1.625
$\angle (O5)(As3)(O1)$	82.1	103.2	106.8	106.7	89.4	104.3	105.9
$\angle (As3)(O1)(As2)$	81.4	96.3	134.8	129.7	86.1	113.8	130.8
$\angle (O1)(As2)(O4)$	82.1	95.5	106.8	103.4	91.8	101.1	104.7

As observed for the dimeric selenium oxides, the optimized bond lengths fall into two general categories: short bond length and long bond length. When comparing the geometrical parameters for As_2O_3 to that of the monomers, it was found that the long As–O bonds

in the equilibrium structures of As_2O_3 (i.e., 1.802 – 2.146 Å) were significantly longer than the $r_e(\text{As-O})$ bond lengths in AsO (i.e., 1.632 Å), AsO_2 (i.e., 1.647 Å) and AsO_3 (i.e., 1.613 Å). Similarly, a few of the short As-O bonds (i.e., 1.612 – 1.700 Å) are longer than the $r_e(\text{As-O})$ bond length in AsO , AsO_2 and AsO_3 ; however, some are shorter than all of the $r_e(\text{As-O})$ bond lengths of the monomers. The bond angles of As_2O_3 (82.1 – 106.8°) are all smaller than the bond angles of AsO_2 (126.2°) while only a few are smaller than the bond angles of AsO_3 (102.3°). As in the case of the dimeric selenium oxides, since most of the bond lengths and angles of the found isomers of As_2O_3 are quite similar, isomerization should be investigated.

The relative energies found for each level of theory and with each basis set used is given in Table 3.9. Also, for a visual aid, the relative energies are plotted for the cc-pVTZ basis set and are given in Figure 3.11.

Table 3.9. Relative energies (kcal/mol) at the B3LYP, CR-CC(2,3) and GVVPT2 levels of theory of the diarsenic trioxide (As_2O_3) isomers and transition states.(Hicks and co-workers. Not yet submitted for publication).

		B3LYP (6-311G*)	CR-CC(2,3) (cc-pVTZ)	GVVPT2 (cc-pVTZ)
Isomer 1	C_{2v}	0.0	0.0	0.0
TS 12	C_1	12.4	17.4	16.2
Isomer 2	C_s	-0.5	8.1	4.4
TS 23	C_1	1.2	8.6	20.6
Isomer 3	C_2	0.2	8.5	20.4
TS 34	C_1	0.9	8.9	21.0
Isomer 4	C_s	0.9	9.1	-

Concerning the comparison between the single point energy calculations using GVVPT2/cc-pVTZ and CR-CC(2,3)/cc-pVTZ, both methods found the same relative ordering. They predicted that isomer 1 was followed by isomer 2 with energies at 4.4 kcal/mol above

isomer 1 for GVVPT2 and 8.1 kcal/mol for CR-CC(2,3). Isomer 3 was found to be the next most stable with relative energies of 20.4 and 8.5 kcal/mol for GVVPT2 and CR-CC(2,3), respectively, and isomer 4 was predicted to be the least stable at 9.1 kcal/mol by CR-CC(2,3). The energy of isomer 4 has yet to be calculated using GVVPT2, being that the MCSCF has yet to converged.

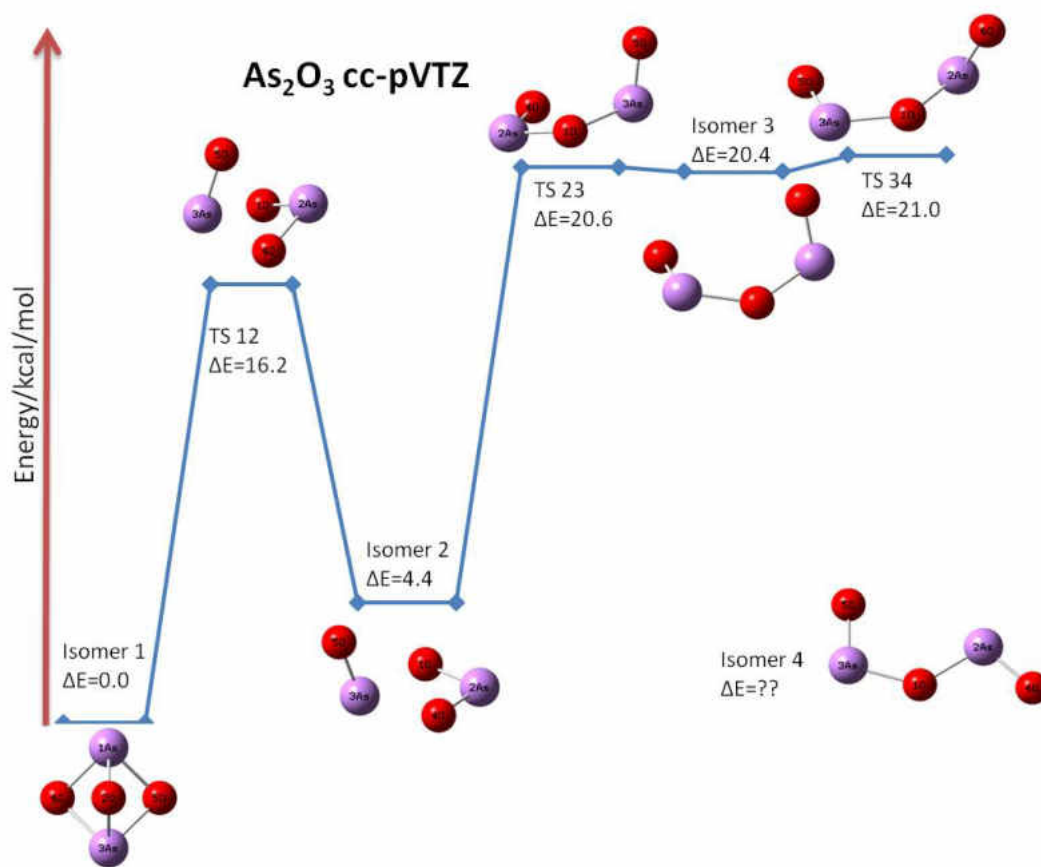


Figure 3.11. Relative GVVPT2/cc-pVTZ energies of diarsenic trioxide (As₂O₃) isomers and transition states (in kcal/mol). (Hicks and co-workers. Not yet submitted for publication)

B3LYP/6-311G* mistakenly predicted the energy of isomer 2 to be the most stable isomer with an energy of -0.5 kcal/mol relative to isomer 1. For all practical purposes, isomer 2 is predicted to be almost isoenergetic with isomer 1. B3LYP/6-311G* then predicts

isomer 3 (0.2 kcal/mol) to be the next most stable followed by isomer 4 (0.9 kcal/mol) as the least stable, which are both nearly isoenergetic with isomer 2 and isomer 1.

The barrier heights between isomers 1 and 2, isomers 2 and 3 and isomers 3 and 4 were predicted by GVVPT2/cc-pVTZ to be 16.2, 20.6 and 21.0 kcal/mol, respectively. Barrier height calculations using CR-CC(2,3)/cc-pVTZ should be completed prior to publication. Using B3LYP/6-311G*, the barrier heights were found to be 12.4 kcal/mol for TS13, 1.2 kcal/mol for TS23 and 0.9 kcal/mol for TS34. TS12 has the closest agreement between B3LYP/6-311G* and GVVPT2/cc-pVTZ, with relatively small differences in energy. However, the other transition states show significant variation between B3LYP/6-311G* and GVVPT2/cc-pVTZ.

3.3.6 As₂O₅

Calculations on the diarsenic pentoxide (As₂O₅) molecules produced a total of seven minima (i.e., isomers 1, 2, 3, 4, 5, 6 and 7) and five transition states (i.e., TS13, TS24, TS36, TS67 and TS53) found. An example of an isomer (i.e., isomer 5), along with the numbering system used for the presentation of the geometrical parameters is given in Figure 3.12. As with the As₂O₃ calculations, the optimized geometrical parameters, which were obtained through the B3LYP/6-311G* calculations performed by Dr. Zhenhua Chen are given in Tables 3.10 and 3.11 for the isomers and transition states, respectively. Also see Figure 3.13 for a graphical representation.

Isomer 1 was predicted to possess D_{3h} symmetry. Isomer 3 was found to possess C_{2v} symmetry. Isomers 2, 4 and 6 all were predicted to have C_s symmetry. Isomers 5 and isomer 7 both were found to be of the C₁ point group. Each of the transition states were

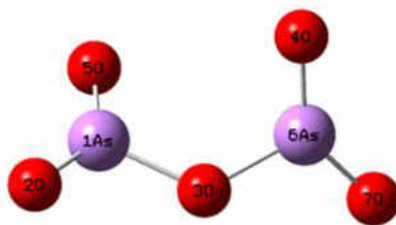


Figure 3.12. Structure of isomer 5 of diarsenic pentoxide (As_2O_5).²²⁰

predicted to have C_s symmetry except for TS 67, which was found to belong to the C_1 point group. Isomer 1 and isomer 2 were found to be cage structures while isomer 6 and TS36 were found to be ring structures.

Table 3.10. Optimized B3LYP/6-311G* geometrical parameters (\AA and degrees) of the diarsenic pentoxide (As_2O_5) isomers.²²⁰

Parameters	Isomer 1 (D_{3h})	2 (C_s)	3 (C_{2v})	4 (C_s)	5 (C_1)	6 (C_s)	7 (C_1)
$R_{(O2)-(As1)}$	1.603	1.757	1.611	1.765	1.611	1.868	1.630
$R_{(O3)-(As1)}$	1.852	1.899	1.611	-	1.822	1.849	1.795
$R_{(O5)-(As1)}$	1.852	1.812	2.071	1.677	1.611	1.849	1.612
$R_{(O3)-(As6)}$	1.852	1.818	-	1.604	1.771	1.816	-
$R_{(O4)-(As6)}$	1.852	1.901	1.693	2.212	1.623	1.836	1.912
$R_{(O7)-(As6)}$	1.603	-	1.604	-	1.609	1.606	1.611
$R_{(O7)-(As1)}$	-	1.777	-	1.765	-	-	-
$\angle (O5)(As6)(O3)$	-	82.0	-	103.3	-	83.6	-
$\angle (O5)(As1)(O3)$	83.6	82.2	105.8	-	110.6	91.3	114.0
$\angle (As1)(O4)(As6)$	79.4	80.8	93.9	92.8	-	-	-
$\angle (O4)(As6)(O7)$	129.7	-	93.9	-	139.5	119.8	99.6
$\angle (O4)(As1)(O7)$	-	112.2	-	123.6	-	-	-
$\angle (O2)(As1)(O4)(As6)$	-	145.2	102.7	144.7	-	-	-
$\angle (O2)(As1)(O3)(As6)$	-	-	-	-	95.4	61.0	-10.2

As observed for the dimeric selenium oxides and for As_2O_3 , the optimized bond lengths fall into two general categories: short bond length and long bond length. Though with As_2O_5 , the line between the two was somewhat blurred. When comparing the geometrical

Table 3.11. Optimized B3LYP/6-311G* geometrical parameters (Å and degrees) of the diarsenic pentoxide (As₂O₅) transition states.²²⁰

Parameters	TS13 (C _s)	TS35 (C _s)	TS24 (C _s)	TS67 (C ₁)	TS36 (C _s)
R _{(O2)-(As1)}	1.605	1.756	1.610	1.657	1.688
R _{(O3)-(As1)}	1.664	-	1.610	1.764	-
R _{(O3)-(As6)}	-	1.670	-	-	1.670
R _{(O4)-(As1)}	-	1.723	1.836	1.611	1.913
R _{(O5)-(As1)}	-	1.723	-	-	1.913
R _{(O5)-(As6)}	1.732	-	1.628	2.027	1.774
R _{(O4)-(As6)}	1.732	-	1.765	-	1.774
R _{(O7)-(As6)}	1.601	-	1.608	1.610	-
R _{(O7)-(As1)}	-	1.767	-	-	1.613
∠ (As1)(As6)(O3)	-	65.9	-	-	93.2
∠ (O2)(As1)(O3)	141.0	-	138.8	107.1	-
∠ (As1)(O4)(As6)	-	-	111.8	-	-
∠ (O5)(As6)(O7)	132.2	-	139.6	101.1	44.3
∠ (O4)(As1)(O7)	-	119.3	-	-	117.8
∠ (O2)(As1)(As6)(O4)	66.1	114.4	-	-	-

parameters for As₂O₅ to that of the monomers, it was found that the long As–O bonds in the equilibrium structures of As₂O₅ (i.e., 1.756 – 2.212 Å) were significantly longer than the r_e (As–O) bond lengths in AsO (i.e., 1.632 Å), AsO₂ (i.e., 1.647 Å) and AsO₃ (i.e., 1.613 Å). While a few of the short As–O bonds (i.e., 1.601 – 1.732 Å) are longer than the r_e (As–O) bond length in AsO, AsO₂ and AsO₃, many are shorter than all of the r_e (As–O) bond lengths for the monomers by 0.001-0.012 Å. Concerning the bond angles of As₂O₅ (82.0 – 139.6°), most of them are smaller than the bond angles of AsO₂ (126.2°) while only a few are smaller than the bond angles of AsO₃ (102.3°). As for the dimeric selenium oxides and As₂O₃, the similarity of bond lengths and angles in the found isomers of As₂O₃ raises the likelihood of isomerization.

The relative energies found for each level of theory and with each basis set used is given in Table 3.12. Also, for a visual aid, the relative energies are plotted for the cc-pVTZ basis set and are given in Figure 3.13. It can be seen that isomer 1 is the minimum for GVVPT2 and for CR-CC(2,3), but isomer 6 is the minimum for B3LYP/6-311G*. In the same way that the energy for isomer 4 of As₂O₃ is missing, the GVVPT2/cc-pVTZ calculation of isomer 6 is missing from Table 3.12 because the MCSCF has not yet converged.

Table 3.12. Relative energies (kcal/mol) at the B3LYP, CR-CC(2,3) and GVVPT2 levels of theory of the diarsenic pentoxide (As₂O₅) isomers and transition states.(Hicks and co-workers. Not yet submitted for publication)

		B3LYP (6-311G*)	CR-CC(2,3) (cc-pVTZ)	GVVPT2 (cc-pVTZ)
Isomer 1	D _{3h}	7.1	0.0	0.0
TS13	C _s	15.4	14.7	16.1
Isomer 3	C _{2v}	4.2	6.5	1.9
TS36	C _s	46.8	50.5	50.0
Isomer 6	C _s	0.0	4.7	-
TS67	C ₁	33.0	51.9	71.8
Isomer 7	C ₁	31.1	-	60.4
TS53	C _s	5.9	9.0	5.6
Isomer 5	C ₁	5.9	9.3	6.6
Isomer 4	C _s	32.2	37.6	44.1
TS24	C _s	43.3	44.3	52.3
Isomer 2	C _s	38.6	34.4	42.8

GVVPT2 predicted that isomer 1 was the most stable followed by isomer 3 with an energy of 1.9 kcal/mol above isomer 1, followed by isomer 5 at 6.6 kcal/mol, isomer 2 at 42.8 kcal/mol, isomer 4 at 44.1 kcal/mol and isomer 7 at 60.4 kcal/mol. For CR-CC(2,3), isomer 1 was again predicted to be the most stable followed by isomer 6 with an energy of 4.7 kcal/mol above isomer 1, followed by isomer 3 at 6.5 kcal/mol, isomer 5 at 9.3 kcal/mol, isomer 2 at 34.4 kcal/mol, and isomer 4 at 37.6 kcal/mol.

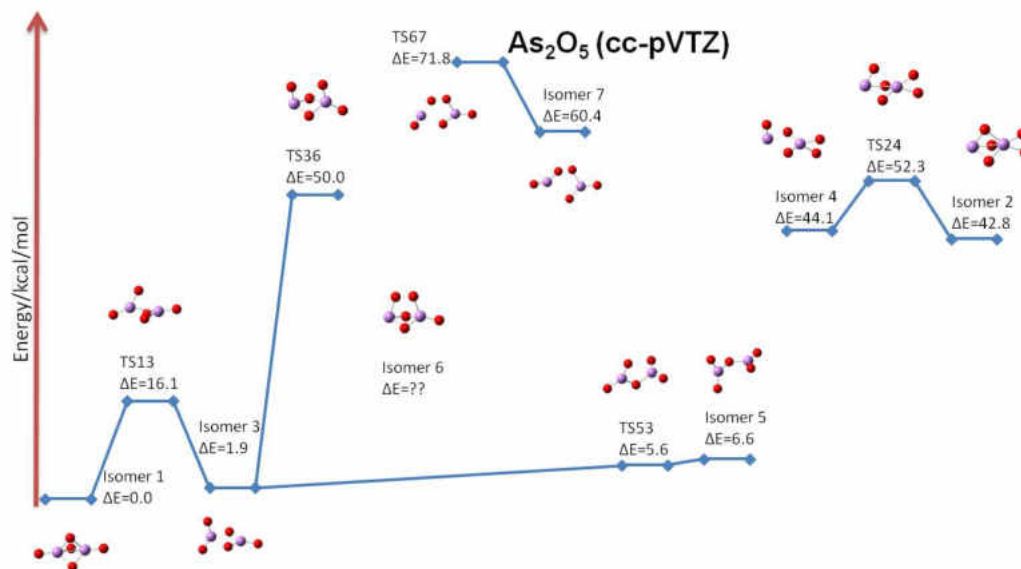


Figure 3.13. Relative GVVPT2/cc-pVTZ energies of diarsenic pentoxide (As_2O_5) isomers and transition states (in kcal/mol). (Hicks and co-workers. Not yet submitted for publication)

In the B3LYP/6-311G* relative energy calculations, isomer 6 was predicted as the most stable isomer, followed by isomer 3 (4.2 kcal/mol), isomer 5 (5.9 kcal/mol), isomer 1 (7.1 kcal/mol), isomer 7 (31.1 kcal/mol), isomer 4 (32.2 kcal/mol), and isomer 2 (38.6 kcal/mol) was predicted as the least stable.

The transition states between isomers 1 and 3, isomers 3 and 5, isomers 2 and 4, and isomers 3 and 6 were predicted by GVVPT2/cc-pVTZ to be at 16.1, 5.6, 52.3, and 50.0 kcal/mol, respectively. Using CR-CC(2,3)/cc-pVTZ, the transition states between isomers 1 and 3, isomers 3 and 5, isomers 2 and 4, and isomers 6 and 7 were predicted to be at 14.7, 9.0, 44.3, and 51.9 kcal/mol, respectively. Using B3LYP/6-311G*, the transition state energies were found to be 15.4 kcal/mol for TS13, 5.9 kcal/mol for TS53, 43.3 kcal/mol for TS24, 33.0 kcal/mol for TS67 and 46.8 kcal/mol for TS36.

3.4 CHAPTER CONCLUSIONS AND FUTURE PROSPECTS

On the basis of good agreement between B3LYP/6-311G* and GVVPT2/cc-pVTZ optimized geometries for the monomers, B3LYP/6-311G* geometry optimizations were performed for Se_2O_3 , Se_2O_5 , As_2O_3 and As_2O_5 . Four isomers were obtained for Se_2O_3 and As_2O_3 , six isomers were found for Se_2O_5 and seven isomers were obtained for As_2O_5 , as were a number of relevant transition states for each species. To our knowledge, these are the first calculations on the diselenium oxide and diarsenic oxide potential energy surfaces. The veracity of B3LYP geometries was corroborated by full optimizations of one isomer of Se_2O_3 and Se_2O_5 at the GVVPT2/cc-pVTZ level. Accurate energies of obtained geometries were obtained at the GVVPT2/cc-pVTZ and CR-CC(2,3)/cc-pVTZ levels at the B3LYP geometries. Without exception, GVVPT2 and CR-CC(2,3) predicted identical energy orderings, with comparable relative energies where the data was available, especially so for the low-lying isomers. In contrast, B3LYP produced semi-quantitatively useful energy results for Se_2O_3 , but not for Se_2O_5 , As_2O_5 or As_2O_3 .

The most stable Se_2O_3 isomer was a structure with C_2 symmetry that has a three-membered ring backbone and terminal oxygens trans to each other (i.e., isomer 1). B3LYP/6-311G* also predicts this isomer to be the minimum. A sizable barrier [30.9 kcal/mol, GVVPT2; 36.8 kcal/mol, CR-CC(2,3)] separates the equilibrium structure from a nearby nonplanar C_s structure (i.e., isomer 3). Relatively small barriers (ca. 10 kcal/mol or less) separate isomer 3 from the other minima that we located: a planar C_s structure (i.e., isomer 2) and a C_{2v} structure (i.e., isomer 4). Based on the energy results and the structural data, we would expect fairly facile isomerizations between the three high-lying stationary points,

but much more stability for the equilibrium structure. For diselenium pentoxide (Se_2O_5) isomers, the most stable structure predicted by GVVPT2/cc-pVTZ and CR-CC(2,3)/cc-pVTZ was one of the two C_s stationary points located (i.e., denoted isomer 4). This isomer has a four-membered ring, which is separated from the next two lowest-lying isomers (i.e., two C_s structures, isomer 3 and isomer 5) by a barriers of 16.0 kcal/mol [17.6 kcal/mol, CR-CC(2,3)] and 13.3 kcal/mol. Two other isomers, both C_2 structures, are high lying, but separated from each other by a small barrier while isomer 5, a C_1 structure, is separated from isomer 6 by a sizable barrier of 42.8 kcal/mol.

The most stable As_2O_3 isomer was a structure with C_{2v} symmetry that has a cage-like structure (i.e., isomer 1). B3LYP/6-311G*, however, predicted isomer 2 to be the minimum, albeit by only 0.5 kcal/mol below the corresponding B3LYP/6-311G* energy of isomer 1. A moderate barrier [16.2 kcal/mol, GVVPT2; 17.4 kcal/mol, CR-CC(2,3)] separates the equilibrium structure from isomer 2, which has nonplanar C_s structure. A barrier of 20.4 kcal/mol separates isomer 2 from isomer 3, which exists in a high-lying shallow minimum. Though GVVPT2 calculations have yet to be conducted on isomer 4, CR-CC(2,3) predicted it to be nearly isoenergetic with the nearby TS 34.

For the As_2O_5 isomers, the most stable structure predicted by GVVPT2/cc-pVTZ and CR-CC(2,3)/cc-pVTZ was a D_{3h} stationary point (i.e., isomer 1). This isomer has a cage-like structure, similar to the As_2O_3 isomer 1 cage with two additional oxygens jutting out from the two arsenics away from the cage. The next lowest-lying isomer (i.e., a C_s structure, isomer 3) is separated from isomer 1 by a barrier of 16.1 kcal/mol [14.7 kcal/mol, CR-CC(2,3)], which is then separated from the next lowest-lying isomer (i.e., a C_s structure, isomer 5) by a small barrier of 5.6 kcal/mol [9.0 kcal/mol, CR-CC(2,3)]. Two high-lying

isomers, for which the calculations have converged, (i.e., two C_s structures, isomer 2 and isomer 4) are connected to each other through a barrier of 52.3 kcal/mol [44.3 kcal/mol, CR-CC(2,3)]. Isomer 2 was predicted to be a cage-like structure similar to isomer 1 of As_2O_3 , yet with the two additional oxygens jutting out from one of the two arsenics away from the cage. Though similar to isomer 1, isomer 2 was predicted to be significantly less stable than isomer 1 by 42.8 kcal/mol [34.4 kcal/mol, CR-CC(2,3)].

Reaction energies were calculated for the addition of the monoselenium oxides to form the diselenium oxides. Both GVVPT2/cc-pVTZ and CR-CC(2,3)/cc-pVTZ predict that SeO will react slightly exothermically with SeO_2 to produce the most stable isomer of Se_2O_3 (eq 3.48) by ca. 6.5 kcal/mol, after inclusion of zero point energy change. Our calculations predict that the direct reaction of SeO_2 with SeO_3 to form Se_2O_5 (eq 3.49) is also energetically favorable, by ca. -18 to -19 kcal/mol [-17.8, GVVPT2; -19.3, CR-CC(2,3)], after inclusion of zero point energy change. Key transition states were located and found to be of modest height (ca. 5-10 kcal/mol) in the direction leading to most stable isomer. The onward reaction of Se_2O_3 with O_2 to form Se_2O_5 (eq 3.50) was shown to be more favorable energetically, with a heat of reaction of ca. -45 kcal/mol [47.2 kcal/mol, GVVPT2; -41.9 kcal/mol, CR-CC(2,3)], after inclusion of change in zero point energy. Taking into account that oxidations of Se to SeO and SeO_2 are thermodynamically favorable (NB: our calculations are in good agreement with experimental data), that oxidation of SeO to SeO_3 is energetically favorable, and that formation reactions of Se_2O_3 and especially Se_2O_5 from selenium oxides are exothermic, it seems that speciation studies of selenium in coal flue gases should take into account the diselenium oxides.

Future work on this project will include finishing the needed calculations, thus filling

in the gaps in Table 3.9, Figure 3.11, 3.12 and Figure 3.13. While some gaps in the data correspond to calculations that merely have yet to be completed, there are several gaps corresponding to issues intrinsic to the methods used. The gap in Table 3.12 for isomer 7 of As_2O_5 corresponds to a questionable value from the CR-CC(2,3) calculation which needs to be confirmed. The gap in Table 3.9 for isomer 4 of As_2O_3 and the gap in Table 3.12 for isomer 6 of As_2O_5 corresponds to the MCSCF calculations failing to converge, which may be due to root flipping. Finally, reaction energies should be calculated to determine the thermodynamics of the formation of the As_2O_3 and As_2O_5 species.

This study corroborates and extends the domain of conclusions of earlier studies with GVVPT2 using incomplete model spaces.²¹⁹ Furthermore, it supports earlier studies that GVVPT2 can be used for accurate energy differences similarly to CCSD(T), in this case extended to greater range through complete renormalization (i.e., CR-CC(2,3)). The favorable scaling of GVVPT2 (i.e., N^5) and rigorous spin-adaptation recommends that GVVPT2 be given serious consideration for studies of complex potential energy surfaces.

REFERENCES

1. ESRL. ESRLs Global Monitoring Division, Trends in Atmospheric Carbon Dioxide. <http://www.esrl.noaa.gov/gmd/ccgg/trends/> (accessed Dec 9, 2013).
2. EIA. US Energy Information Administration. <http://www.eia.gov/countries/country-data.cfm?fips=CHtrk=mcde> (accessed Dec 9, 2013).
3. S.A. Rackley, Carbon Capture and Storage, Elsevier, 2010.
4. R.E. Hester, R.M. Harrison, Carbon Capture: Sequestration and Storage, RSC Pub, 2010.
5. Henley, J. The Guardian (London). The last days of paradise. <http://www.theguardian.com/environment/2008/nov/11/climatechange-endangered-habitats-maldives> (accessed Dec 12, 2013).
6. Albo, A.; Luis, P.; Irabin, A.; *Ind. Eng. Chem. Res.* **2010**, *49*, 11045.
7. Wikipedia. List of countries by carbon dioxide emissions. http://en.wikipedia.org/wiki/List_of_countries_by_carbon_dioxide_emissions (accessed Dec 9, 2013).
8. CDIAC. Fossil-Fuel CO2 Emissions. http://cdiac.ornl.gov/trends/emis/meth_reg.html (accessed Dec 9, 2013).
9. Yu, C.-H. *Aerosol Air Qual. Res.* **2012**, *12*, 745.
10. Petron, G.; Tans, P.; Frost, G.; Chao, D.; Trainer, M. *J. Geophys. Res.* **2008**, *113*, 1.
11. Inventory of U.S. Greenhouse Gas Emissions and Sinks: 1990-2006, Environmental Protection Agency, Washington, DC, 2008.
12. Karl, T. R.; Trenberth, K. E. *Science* **2003**, *302*, 1719.
13. Keeling, C. D.; Whorf, T. P.; Wahlen, M.; Vanderpligt, J. *Nature* **1995**, *375*, 666.
14. Li, H.; Eddaoudi, M.; O'Keefe, M.; Yaghi, O. M. *Nature* **1999**, *402*, 276.
15. Choi, S.; Drese, J.H.; Jones, C.W. *ChemSusChem* **2009**, *2*, 796.
16. Plaza, M.G.; Garca, S.; Rubiera, F.; Pis, J.J.; Pevida, C. *Chem. Eng. J.* **2010**, *163*, 41.

17. Hsu, S. C.; Lu, C., Su, F.; Zeng W.; Chen, W. *Chem. Eng. Sci.* **2010**, *65*, 1354.
18. Arenillas, A.; Drage, T. C.; Smith, K.; Snape, C. E. *J. Anal. Appl. Pyrolysis* **2005**, *74*, 298.
19. Przepiorski, J.; Skrodzewicz M.; Morawski, A. W. *Appl. Surf. Sci.* **2004**, *225*, 235.
20. Gray, M. L.; Soong, Y.; Champagne, K. J.; Baltrus, J.; Stevens, Jr., R. W.; Toochinda, P.; Chuang, S. S. C. *Sep. Purif. Technol.* **2004**, *35*, 31.
21. Strelko, V. V.; Kuts, V. S.; Thrower, P. A. *Carbon* **2000**, *38*, 1499.
22. Wang, Q.; Luo, J.; Zhong, Z.; Borgna, A. *Energy Environ. Sci.* **2011**, *4*, 42.
23. Wikipedia. Zeolite. <http://en.wikipedia.org/wiki/Zeolite> (accessed Dec 9, 2013).
24. Ferey, G. *Chem. Soc. Rev.* **2008**, *37*, 191.
25. MacGillivray, L. *Metal-Organic Frameworks: Design and Application*, 1st ed.; John Wiley Sons, 2010.
26. Batten, S.R.; Neville, S.M.; Turner, D.R.; *Coordination Polymers: Design. Analysis and Application*, 1st ed.; RSC Publishing, 2009.
27. Yaghi, O.M.; O'Keeffe, M.; Ockwig, N.W.; Chae, H.K.; Eddaoudi, M.; Kim, J.; *Nature* **2003**, *423*, 705.
28. Kitagawa, S.; Kitaura, R.; Noro, S. *Angew. Chem., Int. Ed.* **2004**, *43*, 2334.
29. Li, J.-R.; Ma, Y.; McCarthy, M. C.; Sculley, J.; Yu, J.; Jeong, H.-K.; Balbuena, P. B.; Zhou, H.-C. *Coordination Chemistry Reviews* **2011**, *255*, 1791-1823.
30. Zhao, D.; Yuan, D. Q.; Sun, D. F.; Zhou, H. C. *J. Am. Chem. Soc.* **2009**, *131*, 9186.
31. Yuan, D.; Zhao, D.; Sun, D.; Zhou, H.C. *Angew. Chem., Int. Ed.* **2010**, *49*, 5357.
32. Eddaoudi, M.; Kim, J.; Rosi, N.; Vodak, D.; Wachter, J.; O'Keefe, M.; Yaghi, O. M. *Science* **2002**, *295*, 469-472.
33. NETL. NETL: the Energy lab. <http://www.netl.doe.gov/publications/proceedings/05/carbon-seq/Poster%20234.pdf> (accessed Dec 9, 2013).
34. Ramsahye, N.A.; Maurin, G.; Bourrelly, S.; Llewellyn, P.L.; Serre, C.; Loiseau, T.; Devic, T.; Ferey, G. *J. Phys. Chem. C* **2008**, *112*, 514.
35. Xu, Q.; Liu, D. H.; Yang, Q. Y.; Zhong, C. L.; Mi, J. G. *J. Mater. Chem.* **2010**, *20*, 706.
36. Torrisi, A.; Mellot-Draznieks, C.; Bell, R. G. *J. Chem. Phys.* **2009**, *130*, 194703.
37. Torrisi, A.; Mellot-Draznieks, C.; Bell, R. G. *J. Chem. Phys.* **2010**, *132*, 044705.

38. Dubbeldam, D.; Frost, H.; Walton, K. S.; Snurr, R. Q. *Fluid Phase Equilib.* **2007**, *261*, 152.
39. Becke, A.D. *J.Chem.Phys.* **1993**, *98*, 5648-5652.
40. Stephens, P.J.; Devlin, F.J.; Chabalowski, C.F.; Frisch, M.J. *J.Phys.Chem.* **1994**, *98*, 11623-11627.
41. Møller, C.; Plesset, M. S. *Phys. Rev.* **1934**, *46*, 618-622.
42. Pianwanit, A.; Kritayakornupong, C.; Vongachariya, A.; Selphusit, N.; Ploymeerusmee, T.; Remsungnen, T.; Nuntasri, D.; Fritzsche, S.; Hannongbua, S. *Chem. Phys.* **2008**, *349*, 77.
43. Düren, T.; Sarkisov, L.; Yaghi, O. M.; Snurr, R. Q. *Langmuir* **2004**, *20*, 2683.
44. Düren, T.; Snurr, R. Q. *J. Phys. Chem. B* **2004**, *108*, 15703.
45. Sarkisov, L.; Düren, T.; Snurr, R. Q. *Mol. Phys.* **2004**, *102*, 211.
46. Garberoglio, G.; Skoulidas, A. I.; Johnson, J. K. *J. Phys. Chem. B.* **2005**, *109*, 13094.
47. Frost, H.; Duren, T.; Snurr, R. Q. *J. Phys. Chem. B* **2006**, *110*, 9565.
48. Jiang, J.-W.; Sandler, S. *Langmuir* **2006**, *22*, 5702.
49. Babarao, R.; Hu, Z.; Jiang, J.; Chempath, S.; Sandler, S. I. *Langmuir* **2007**, *23*, 659.
50. Walton, K. S.; Millward, A. R.; Dubbeldam, D.; Frost, H.; Low, J. L.; Yaghi, O. M.; Snurr, R. Q. *J. Am. Chem. Soc.* **2008**, *130*, 406.
51. Dubbeldam, D.; Galvin, C. J.; Walton, K. S.; Ellis, D. E.; Snurr, R. Q. *J. Am. Chem. Soc.* **2008**, *130*, 10884.
52. Yang, Q.; Zhong, C. J. *Phys. Chem. C* **2008**, *112*, 1562.
53. Martn-Calvo, A.; Garcia-Perez, E.; Castillo, J.; Calero, S. *Phys. Chem. Chem. Phys.* **2008**, *10*, 7085.
54. Düren, T.; Bae, Y.-S.; Snurr, R. Q. *Chem. Soc. Rev.* **2009**, *38*, 1237.
55. Greathouse, J. A.; Kinnibrugh, T. L.; Allendorf, M. D. *Ind. Eng. Chem. Res.* **2009**, *48*, 3425.
56. Keskin, S.; Liu, J.; Rankin, R. B.; Johnson, J. K.; Sholl, D. S. *Ind. Eng. Chem. Res.* **2009**, *48*, 2355.
57. Zheng, C.; Liu, D.; Yang, Q.; Zhong, C.; Mi, J. *Ind. Eng. Chem. Res.* **2009**, *48*, 10479.
58. Xiong, R.; Keffer, D.; Fuentes-Cabrera, M.; Nicholson, D.; Michalkova, A.; Petrova, T.; Leszczynski, J.; Odbadrakh, K.; Doss, B.; Lewis, J. *Langmuir* **2010**, *26*, 5942.

59. DeToni, M.; Pullumbi, P.; Coudert, F.-X.; Fuchs, H. *J. Phys. Chem. C* **2010**, *114*, 21631.
60. Liu, J.; Thallapally, P.; McGrail, B.; Brown, D.; Liu, J.; *Chem. Soc. Rev.* **2012**, *41*, 2308.
61. Aleksandrov, T. D. Vapor-Liquid Phase Equilibria Using Monte Carlo Wang-Landau Simulations. Ph.D. Dissertation, University of North Dakota, Grand Forks, ND, 2012.
62. Frenkel D.; Smit, B. *Understanding Molecular Simulation*, 2nd ed.; Academic Press: San Diego, CA, 2002.
63. Siderius D. W.; Shen, V. K. *J. Phys. Chem. C* **2013**, *117*, 5861.
64. Smith, G. R.; Bruce, A. D.; *J. Phys. A* **1995**, *28*, 6623.
65. Wang, J. S.; Tay, T. K.; Swendsen, R. H.; *Phys. Rev. Lett.* **1999**, *82*, 476.
66. Wang, J. S. *Comput. Phys. Commun.* **1999**, *122*, 22.
67. Wang J. S.; Swendsen, R. H. *J. Stat. Phys.* **2002**, *106*, 245.
68. Fitzgerald, M.; Picard, R. R.; Silver, R. N. *Europhys. Lett.* **1999**, *46*, 282.
69. Fitzgerald, M.; Picard, R. R.; Silver, R. N. *J. Stat. Phys.* **2000**, *98*, 321.
70. Errington, J. J. *Chem. Phys.* **2003**, *118*, 9915.
71. Gospodinov I. D.; Escobedo, F. A. *J. Chem. Phys.* **2005**, *122*, 164103.
72. Okamoto, Y. *J. Mol. Graphics Modell.* **2004**, *22*, 425.
73. Paluch, A. S.; Shen, V. K.; Errington, J. R. *Ind. Eng. Chem. Res.* **2008**, *47*, 4533.
74. Errington, J. R.; Shen, V. K. *J. Chem. Phys.* **2005**, *123*, 164103.
75. Wang, F. G.; Landau, D. P. *Phys. Rev. Lett.* **2001**, *86*, 2050.
76. Wang, F. G.; Landau, D. P. *Phys. Rev. E* **2001**, *64*, 056101.
77. Ganzenmller, G.; Camp, P. J. *J. Chem. Phys.* **2007**, *127*, 154504.
78. Shell, M. S.; Debenedetti, P. G.; Panagiotopoulos, A. Z. *Phys. Rev. E* **2002**, *66*, 056703.
79. Shell, M. S.; Debenedetti, P. G.; Panagiotopoulos, A. Z. *J. Phys. Chem. B* **2004**, *108*, 19748.
80. de Pablo, J. J.; Yan, Q.; Faller, R. *J. Chem. Phys.* **2002**, *116*, 8649.
81. Shell, M. S.; Debenedetti, P. G.; Panagiotopoulos, A. Z. *J. Chem. Phys.* **2003**, *119*, 9406.

82. Desgranges, C.; Delhommelle, J. *J. Chem. Phys.* **2009**, *130*, 244109.
83. Aleksandrov, T.; Desgranges, C.; Delhommelle, J. *Fluid Phase Eq.* **2010**, *287*, 79.
84. Desgranges, C.; Kastl, E. A.; Aleksandrov, T.; Delhommelle, J. *Mol. Simul.* **2010**, *36*, 544.
85. Desgranges, C.; Hicks, J.M.; Magness, A.; Delhommelle, J. *Molecular Physics*, **2010**, *108*, 151.
86. Malakis, A.; Berker, A. N.; Hijagapiou, I. A.; Fytas, N. G.; Papakonstantinou, T. *Phys. Rev. E* **2010**, *81*, 041113.
87. Ganzenmiller, G.; Camp, P. J. *Condens. Matter Phys.* **2011**, *14*, 33602.
88. Zhou, C.; Bhatt, R.N. *Phys. Rev. E* **2005**, *72*, 025701.
89. Duane, S.; Kennedy, A. D.; Pendleton, B. J.; Roweth, D. *Phys. Lett. B* **1987**, *195*, 216.
90. Mehlig, B.; Heerman, D. W.; Forrest, B. M. *Phys. Rev. B* **1992**, *45*, 679.
91. Vargaftik, N. B.; Vinogradov, Y. K.; Yargin, V. S. *Handbook of Physical Properties of Liquids and Gases*, Begell House: New York, 1996.
92. Desgranges, C.; Delhommelle, J. *J. Chem. Phys.* **2012**, *136*, 184107.
93. Desgranges, C.; Delhommelle, J. *J. Chem. Phys.* **2012**, *136*, 184108.
94. Hicks, J. M.; Desgranges C.; Delhommelle, J. *J. Phys. Chem. C* **2012**, *116*, 22938.
95. Myers, A. L.; Monson, P. A. *Langmuir* **2002**, *18*, 10261.
96. Myers, A. *AIChE J.* **2002**, *48*, 145.
97. Myers, A. L. *Adsorption* **2002**, *9*, 9.
98. Landau, D. P. *Phys. Rev. B* **1976**, *13*, 2997.
99. Ferrenberg A. M.; Swendsen, R. H. *Phys. Rev. Lett.* **1988**, *61*, 2635.
100. Ferrenberg A. M.; Swendsen, R. H. *Phys. Rev. Lett.* **1989**, *63*, 1195.
101. Wang, J.-S.; Tay, T. K.; Swendsen, R. H. *Phys. Rev. Lett.* **1999**, *82*, 476.
102. Wu, F.Y. *Rev. Mod. Phys.* **1982**, *54*, 235.
103. Beale, P. D. *Phys. Rev. Lett.* **1996**, *76*, 78.
104. Lyubartsev, A. P.; Martsinovski, A. A.; Shevkunov, S. V.; Vorontsov-Velyaminov, P. N. *J. Chem. Phys.* **1992**, *96*, 1776.
105. Muller, M.; Paul, W. *J. Chem. Phys.* **1994**, *100*, 719.

106. Escobedo, F.; de Pablo, J. J. *J. Chem. Phys.* **1996**, *105*, 4391.
107. Escobedo, F. A.; Abreu, C. R. A. *J. Chem. Phys.* **2006**, *124*, 104110.
108. Abreu, C. R. A.; Escobedo, F. A. *J. Chem. Phys.* **2006**, *124*, 054116.
109. Singh, J. K.; Errington, J. R.; *J. Phys. Chem. B* **2006**, *110*, 1369.
110. Escobedo, F. A.; Martinez-Veracoechea, F. J. *J. Chem. Phys.* **2007**, *127*, 174103.
111. Escobedo, F. A. *J. Chem. Phys.* **2007**, *127*, 174104.
112. Escobedo, F. A.; Martinez-Veracoechea, F. J. *J. Chem. Phys.* **2008**, *129*, 154107.
113. Trebst, S.; Huse, D. A.; Troyer, M. *Phys. Rev. E* **2004**, *70*, 046701.
114. Shi, W.; Maginn, E. J. *J. Comput. Chem.* **2008**, *29*, 2520.
115. Panagiotopoulos, A. Z. *Mol. Phys.* **1987**, *61*, 813.
116. Potoff, J. J.; Siepmann, J. I. *AIChE J.* **2001**, *47*, 1676.
117. Maitland, G. C.; Rigby, M.; Smith, E. B.; Wakeham, W. A. *Intermolecular Forces*, Clarendon: Oxford, 1981.
118. Mayo, S. L.; Olafson, B. D.; Goddard, W. A. *J. Phys. Chem.* **1990**, *94*, 8897.
119. Nicholson, D.; Parsonage, N. G. *Computer simulation and the statistical mechanics of adsorption*, 1st ed.; Academic Press: London, 1982.
120. Adamson, A. W.; Gast, A. P. *Physical chemistry of surfaces*, 6th ed.; Wiley: New York, 1997.
121. Steele, W. A. *The interaction of gases with solid surfaces*, 1st ed.; Pergamon: Oxford, 1974.
122. Yang, R. T. *Gas separation by adsorption processes*, 1st ed.; Butterworths: Boston, 1987.
123. Rowsell, J. L. C.; Yaghi, O. M. *Microporous Mesoporous Mater.* **2004**, *73*, 3.
124. Davis, M. E. *Nature* **2002**, *417*, 813.
125. James, S. L. *Chem. Soc. Rev.* **2003**, *32*, 276.
126. Rosseinsky, M. J. *Microporous Mesoporous Mater.* **2004**, *73*, 15.
127. Mueller, U.; Schubert, M.; Teich, F.; Puetter, H.; Schierle-Arndt, K.; Pastre, J. *J. Mater. Chem.* **2006**, *16*, 626.
128. Rowsell, J. L. C.; Yaghi, O. M. *Angew. Chem., Int. Ed.* **2005**, *44*, 4670.

129. Eddaoudi, M.; Li, H.; Yaghi, O. M. *J. Am. Chem. Soc.* **2000**, *122*, 1391.
130. Wong-Foy, A. G.; Matzger, A. J.; Yaghi, O. M. *J. Am. Chem. Soc.* **2006**, *128*, 3494.
131. Rowsell, J. L. C.; Spencer, E. C.; Eckert, J.; Howard, J. A. K.; Yaghi, O. M. *Science* **2005**, *309*, 1350.
132. Millward, A. R.; Yaghi, O. M. *J. Am. Chem. Soc.* **2005**, *127*, 17998.
133. Skoulidas, A. I.; Sholl, D. S. *J. Phys. Chem. B* **2005**, *109*, 15760.
134. Chen, H.; Sholl, D. S. *Langmuir* **2006**, *22*, 709.
135. Hill, T. L. *Adv. Catal.* **1952**, *4*, 211.
136. Ruthven, D. M. *Principles of adsorption and adsorption processes*, 1st ed.; Wiley-Interscience: New York, 1982.
137. McQuarrie, D. A. *Statistical Mechanics*, 1st ed.; Harper-Row: New York, 1973.
138. DeToni, M.; Pullumbi, P.; Coudert, F.-X.; Fuchs, H. *J. Phys. Chem. C* **2010**, *114*, 21631.
139. World Coal Association. Coal Electricity. <http://www.worldcoal.org/coal/uses-of-coal/coal-electricity/> (accessed May 23, 2013).
140. Nelson, P. F. *Energy Fuels FIELD Full Journal Title:Energy Fuels* **2007**, *21*, 477.
141. Ebdon, L.; Pitts, L.; Cornelis, R.; Crews, H.; Donard, O. F. X.; Quevauviller, P.; Editors, Trace Element Speciation for Environment, Food and Health; 2001.
142. Fitzpatrick, S.; Ebdon, L.; Foulkes, M. E. *Int. J. Environ. Anal. Chem.* **2002**, *82*, 835.
143. Swaine, D. J. *Fuel Process. Technol.* **2000**, 6566, 21.
144. Jadhav, R. A.; Fan, L.-S. *Environ. Sci. Technol. FIELD Full Journal Title:Environmental Science and Technology* **2001**, *35*, 794.
145. van der Hoek, E. E.; Comans, R. N. J. *Environ. Sci. Technol. FIELD Full Journal Title:Environmental Science and Technology* **1996**, *30*, 517.
146. Huggins, F. E.; Senior, C. L.; Chu, P.; Ladwig, K.; Huffman, G. P. *Environ. Sci. Technol. FIELD Full Journal Title:Environmental Science Technology* **2007**, *41*, 3284.
147. Shah, P.; Strezov, V.; Stevanov, C.; Nelson, P. F. *Energy Fuels* **2007**, *21*, 506.
148. Shah, P.; Strezov, V.; Stevanov, C.; Nelson, P. F. *Energy Fuels FIELD Full Journal Title:Energy Fuels* **2007**, *21*, 506.
149. Chen, C. J.; Wu, M. M.; Lee, S. S.; Wang, J. D.; Cheng, S. H.; Wu, H. Y. *Arteriosclerosis (Dallas, Tex.)* **1988**, *8*, 452.

150. Lai, M. S.; Hsueh, Y. M.; Chen, C. J.; Shyu, M. P.; Chen, S. Y.; Kuo, T. L.; Wu, M. M.; Tai, T. Y. *Am J Epidemiol* **1994**, *139*, 484.
151. Chen, C.-J.; Hsueh, Y.-M.; Lai, M.-S.; Shyu, M.-P.; Chen, S.-Y.; Wu, M.-M.; Kuo, T.-L.; Tai, T.-Y. *Hypertension (Dallas)* **1995**, *25*, 53.
152. Chen, C. J.; Chen, C. W.; Wu, M. M.; Kuo, T. L. *Br J Cancer* **1992**, *66*, 888.
153. Chen, C. J.; Wang, C. J. *Cancer Res.* **1990**, *50*, 5470.
154. Sonich-Mullin, C.; Fielder, R.; Wiltse, J.; Baetcke, K.; Dempsey, J.; Fenner-Crisp, P.; Grant, D.; Hartley, M.; Knaap, A.; Kroese, D.; Mangelsdorf, I.; Meek, E.; Rice, J. M.; Younes, M. *Regul. Toxicol. Pharmacol.* **2001**, *34*, 146.
155. Swaine, D. J. *Fuel Process. Technol. FIELD Full Journal Title:Fuel Processing Technology* **2000**, *65-66*, 21.
156. J. E. Staudt, T. Engelmeyer, W. H. Weston, R. Sigling, Deactivation of SCR Catalyst with Arsenic-Experience at OUC Stanton and Implications for Other Coal-Fired Boilers, presented at the Conference on Selective Catalytic Reduction (SCR) and Selective NonCatalytic Reduction (SNCR) for NO_x Control, Pittsburgh, PA, May 15-16, 2002, US Department of Energy, National Energy Technology Laboratory, Pittsburgh, PA, (2002).
157. Zhao, Y.; Zhang, J.; Huang, W.; Wang, Z.; Li, Y.; Song, D.; Zhao, F.; Zheng, C. *Energy Convers. Manage.* **2008**, *49*, 615.
158. Monahan-Pendergast, M.; Przybylek, M.; Lindblad, M.; Wilcox, J. *Atmos. Environ. FIELD Full Journal Title:Atmospheric Environment* **2008**, *42*, 2349.
159. Urban, D. R.; Wilcox, J. *J Phys Chem A FIELD Full Journal Title:The journal of physical chemistry. A* **2006**, *110*, 5847.
160. Cheong, S. K.; Bunker, B. A.; Shibata, T.; Hall, D. C.; DeMelo, C. B.; Luo, Y.; Snider, G. L.; Kramer, G.; El-Zein, N. *Appl. Phys. Lett. FIELD Full Journal Title:Applied Physics Letters* **2001**, *78*, 2458.
161. Yan, R.; Gauthier, D.; Flamant, G.; Peraudeau, G.; Lu, J.; Zheng, C. *Environ. Sci. Technol.* **2001**, *35*, 1406.
162. Senior, C. L.; Bool, L. E.; Srinivasachar, S.; Pease, B. R.; Porle, K. *Fuel Process. Technol.* **2000**, *63*, 149.
163. Zhang, J.; Zhao, Y.; Ding, F.; Zeng, H.; Zheng, C. *Front. Energy Power Eng. China* **2007**, *1*, 273.
164. Fitzpatrick, S.; Ebdon, L.; Foulkes, M. E. *Int. J. Environ. Anal. Chem.* **2002**, *82*, 835.
165. Swaine, D. J. *Fuel Process. Technol.* **2000**, *65-66*, 21.

166. Lemly, D. A. *Ecotoxicol. Environ. Safety A* **2004**, *59*, 44.
167. Clark, L. C.; Combs, G. F., Jr.; Turnbull, B. W.; Slate, E. H.; Chalker, D. K.; Chow, J.; Davis, L. S.; Glover, R. A.; Graham, G. F.; Gross, E. G.; Krongrad, A.; Leshner, J. L., Jr.; Park, H. K.; Sanders, B. B., Jr.; Smith, C. L.; Taylor, J. R. *JAMA, J. Am. Med. Assoc.* **1996**, *276*, 1957.
168. Zheng, B.; Hong, Y.; Zhao, W.; Zhou, H.; Xia, W.; Su, H.; Mao, D.; Yang, L.; Thornton, I. *Chin. Sci. Bull.* **1992**, *37*, 1725.
169. Trumble, J. T.; Kund, G. S.; White, K. K. *Environ. Pollut.* **1998**, *101*, 175.
170. Schefel oxides. In *Gmelins Handbuch der Anorganischen Chemie, Erzsbd. 3 Springer Verlag, Berlin* **1980**.
171. Brisdon, A. K.; Ogden, J. S. *J. Mol. Struct.* **1987**, *157*, 141.
172. Urban, D. R.; Wilcox, J. J. *J. Phys. Chem. A* **2006**, *110*, 8797.
173. Steudel, R.; Sandow, T.; Steidel, J. Z. *Naturforsch., B: Anorg. Chem., Org. Chem. Zeitschrift fuer Naturforschung, Teil B: Anorganische Chemie, Organische Chemie* **1985**, *40B*, 594.
174. Meyer, B. *Sulfur, Energy, and Environment.* **1977**.
175. Brabson, G. D.; Andrews, L.; Marsden, C. J. *J. Phys. Chem.* **1996**, *100*, 16487.
176. Brassington, N. J.; Edwards, H. G. M.; Long, D. A.; Skinner, M. J. *Raman Spectrosc.* **1978**, *7*, 158.
177. Khait, Y. G.; Song, J.; Hoffmann, M. R. *J. Chem. Phys.* **2002**, *117*, 4133.
178. Song, J.; Khait, Y. G.; Hoffmann, M. R. *Abstracts of Papers, 222nd ACS National Meeting, Chicago, IL, United States, August 26-30, 2001*, PHYS-292.
179. Jiang, W.; Khait, Y. G.; Hoffmann, M. R. *J. Phys. Chem. A* **2009**, *113*, 4374.
180. Dudley, T. J.; Hoffmann, M. R. *Mol. Phys.* **2003**, *101*, 1303.
181. Azenkeng, A.; Laumb, J.; Jensen, R.; Olson, E.; Benson, S.; Hoffmann, M. R. *Abstracts of Papers, 231st ACS National Meeting, Atlanta, GA, United States, March 26-30, 2006*, PHYS-448.
182. Devarajan, A.; Gaenko, A. V.; Khait, Y. G.; Hoffmann, M. R. *J. Phys. Chem. A* **2008**, *112*, 2677.
183. Song, J.; Khait, Y. G.; Hoffmann, M. R. *J. Chem. Phys.* **2003**, *118*, 10065.
184. Purvis, G. D., III; Bartlett, R. J. *J. Chem. Phys.* **1982**, *76*, 1910.

185. Pople, J. A.; Head-Gordon, M.; Raghavachari, K. *J. Chem. Phys.* **1987**, *87*, 5968.
186. Woon, D. E.; Dunning, T. H., Jr. *J. Chem. Phys.* **1993**, *98*, 1358.
187. Wilson, A. K.; Peterson, K. A.; Woon, D. E.; Dunning, T. H., Jr. *J. Chem. Phys.* **1999**, *110*, 7667.
188. Frisch, M. J.; Trucks, G. W.; Schlegel, H. B.; Scuseria, G. E.; Robb, M. A.; Cheeseman, J. R.; Zakrzewski, V. G.; Montgomery, J. A., Jr.; Stratmann, R. E.; Burant, J. C.; Dapprich, S.; Millam, J. M.; Daniels, A. D.; Kudin, K. N.; Strain, M. C.; Farkas, O.; Tomasi, J.; Barone, V.; Cossi, M.; Cammi, R.; Mennucci, B.; Pomelli, C.; Adamo, C.; Clifford, S.; Ochterski, J.; Peterson, G. A.; Ayala, P. Y.; Cui, Q.; Morokuma, K.; Rega, N.; Salvador, P.; Dannenberg, J. J.; Malick, D. K.; Rabuck, A. D.; Raghavachari, K.; Foresman, J. B.; Cioslowski, J.; Ortiz, J. V. B., A. G.; Stefanov, B. B.; Liu, G.; Liashenko, A.; Piskorz, P.; Komaromi, I.; Gomperts, R.; Martin, R. L.; Fox, D. J.; Keith, T.; Al-Laham, M. A.; Peng, C. Y.; Nanayakkara, A.; Challacombe, M.; Gill, P. M. W.; Johnson, C., B. W.; Wong, M. W.; Andres, J. L.; Gonzalez, C.; Head-Gordon, M.; Replogle, E. S.; Pople, J. A. *Gaussian 03, Gaussian, Inc.: Pittsburgh, PA*, **2002**.
189. A. Szabo and N. S. Ostlund, *Modern Quantum Chemistry*, Revised 1st Ed.; McGraw-Hill Publishing Co.: Singapore, 1986.
190. Born, M.; Oppenheimer, R. *Ann. Phys. (Leipzig)* **1927**, *84*, 457.
191. Moller, C.; Plesset, M. S. *Phys. Rev.* **1934**, *46*, 618.
192. Grimme, S. *J. Chem. Phys.* **2003**, *118*, 9095.
193. Grimme, S. *J. Phys. Chem. A* **2005**, *109*, 3067.
194. Roos, B. O. In *Ab Initio Methods in Quantum Chemistry*; Lawley, K. P., Ed.; Wiley: New York, 1987; Vol. 2, p 399-445.
195. Roos, B. O.; Szulkin, M.; Jaszunski, M. *Theor. Chim. Acta* **1987**, *71*, 375.
196. Olsen, J.; Roos, B. O.; Joergensen, P.; Jensen, H. J. A. *J. Chem. Phys.* **1988**, *89*, 5082.
197. Khait, Y. G.; Song, J.; Hoffmann, M. R. Macroconfigurations in Molecular Electronic Structure Theory. *Int. J. Quantum Chem.* **2004**, *99*, 210.
198. Kirtman, B. *J. Chem. Phys.* **1981**, *75*, 798.
199. Malrieu, J. P.; Durand, Ph.; Daudey, J. P. *J. Phys. A* **1985**, *18*, 809.
200. Lindgren, I.; Morrison, J. *Atomic Many-Body Theory*, 2nd ed.; Springer: Berlin, 1986.
201. Mukhopadhyay, D.; Datta, B.; Mukherjee, D. *Chem. Phys. Lett.* **1992**, *197*, 236.
202. Malrieu, P. P.; Heully, J. L.; Zaitsevskii, A. *Theor. Chim. Acta* **1995**, *90*, 167.

203. Khait, Y. G.; Hoffmann, M. R. *J. Chem. Phys.* **1998**, *108*, 8317.
204. Meissner, L. *J. Chem. Phys.* **1998**, *108*, 9227.
205. Landau, A.; Eliav, E.; Kaldor, U. *Chem. Phys. Lett.* **1999**, *313*, 399.
206. Eliav, E.; Borschevsky, A.; Shamasundar, K. R.; Pal, S.; Kaldor, U. *Int. J. Quantum Chem.* **2009**, *109*, 2909.
207. Kirtman, B. *J. Chem. Phys.* **1981**, *75*, 798.
208. Kuhler, K.; Hoffmann, M. R. *J. Math. Chem.* **1996**, *20*, 351.
209. Khait, Y. G.; Hoffmann, M. R. *J. Chem. Phys.* **1998**, *108*, 8317.
210. Murphy, R. B.; Messmer, R. P. *Chem. Phys. Lett.* **1991**, *183*, 443.
211. Finley, J.; Malmqvist, P.-A.; Roos, B. O.; Serrano-Andres, L. *Chem. Phys. Lett.* **1998**, *288*, 299.
212. Nakano, H.; Nakatani, J.; Hirao, K. *J. Chem. Phys.* **2001**, *114*, 1133.
213. Hoffmann, M. R. *Chem. Phys. Lett.* **1993**, *210*, 193.
214. Hoffmann, M. R. *J. Phys. Chem.* **1996**, *100*, 6125.
215. Mbote, Y. E. B.; Khait, Y. G.; Hardel, C.; Hoffmann, M. R. *J. Phys. Chem. A* **2010**, *114*, 8831.
216. Schmidt, M. W.; Baldrige, K. K.; Boatz, J. A.; Elbert, S. T.; Gordon, M. S.; Jensen, J. H.; Koseki, S.; Matsunaga, N.; Nguyen, K. A.; et al. *J. Comput. Chem.* **1993**, *14*, 1347.
217. Gordon, M. S.; Schmidt, M. W. In *Theory and Applications of Computational Chemistry: First Forty Years*; Dykstra, C. E., Frenking, G., Kim, K. S., Scuseria, G. E., Eds.; Elsevier: Amsterdam, 2005; Chapter 41.
218. Mokambe, R. M.; Hicks, J. M.; Kerker, D.; Jiang, W.; Theis, D.; Chen, Z.; Khait, Y. G.; Hoffmann, M. R. *Mol. Phys.* **2013**, *111*, 1078.
219. Mbote, Y. E. B.; Khait, Y. G.; Hardel, C.; Hoffmann, M. R. *J. Phys. Chem. A* **2010**, *114*, 8831.
220. Mokambe, R. M. Theoretical Studies of the Ground and Low-Lying Excited States of [3,3]Bidiazirinylidene(C₂N₄), Tetramethyleneethane Diradical, and Arsenic and Selenium Oxides. Ph.D. Dissertation, University of North Dakota, Grand Forks, ND, 2012.